DOT/FAA/TC-24/27

Federal Aviation Administration
William J. Hughes Technical Center
Aviation Research Division
Atlantic City International Airport
New Jersey 08405

Structurally Distributed Aircraft Battery

February 2025

Technical Report

U.S. Department of Transportation
Federal Aviation Administration

NOTICE

Form DOT F 1700.7 (8-72) Reproduction of completed page authorized

1. Report No. DOT/FAA/TC-24/27	2. Government Accession No.	3. Recipient's Catalog No.
4. Title and Subtitle Structurally Distributed Aircraft Battery		5. Report Date February 2025
		6. Performing Organization Code
7. Author(s) Dr. Jitendra Kumar Dr. Alexander Morgan		8. Performing Organization Report No.
9. Performing Organization Name and Address University of Dayton Research Institute (UDRI) Power and Energy Division Solid-State Battery & Integrated Systems Laboratory 300 College Park, Dayton, OH 45469-7535		10. Work Unit No. (TRAIS)
		11. Contract or Grant No. 692M15-20-C-00014
12. Sponsoring Agency Name and Address Federal Aviation Administration William J. Hughes Technical Center Aviation Research Division Atlantic City International Airport, NJ 08405		13. Type of Report and Period Covered Final Report
		14. Sponsoring Agency Code ANG-E2

15. Supplementary Notes
Dr. Thomas Maloney is the Federal Aviation Administration William J. Hughes Technical Center Aviation Research Division COR.

16. Abstract

Lithium-ion batteries (LIBs) are critical to the early adoption of electrified small aircraft because LIBs can provide the required energy, power, and cycle life. However, safety is still a concern, especially in dangerous situations like aircraft crashes or operations in harsh conditions. If damaged, the battery can release stored energy fast, leading to a battery fire known as thermal runaway (TR). Safety problems are particularly challenging for aircraft batteries due to their large size, many times larger than battery packs used in electric vehicles. One way to mitigate safety problems is to design LIBs in small sizes to minimize safety risks. Another engineering solution is to design mechanically and thermally stable battery enclosures to protect LIB packs from various adverse environmental effects, especially mechanical damage (e.g. puncture), which leads to electrical shorting and accelerates exothermic reactions, enabling TR propagation from one cell (or module) to another. Ideally, TR from a damaged cell or module to a nearby cell or module can be controlled using a thick battery enclosure. However, a battery enclosure that is very thick and heavy would reduce the battery energy density significantly, which practically is unacceptable. This project answers questions, such as how big one battery module should be, how much protection do the batteries need, and how they should be protected without adding too much extra weight, negating the advantage of high energy in today's and future aerospace battery systems. Based on data generated in this project, design guidelines are provided for a LIB module comprising the right battery cell chemistry and its format. It also provides guidelines for a secondary battery enclosure to facilitate natural heating-cooling, desired mechanical protection, thermal isolation, and containment of battery fire gases in the fire event.

17. Key Words electric aircraft, distributed electric power systems, battery enclosure and mechanical strength, battery enclosure and heat dissipation, indentation, compression, and fatigue resiliency of battery enclosure, mechanical load and battery thermal runaway, mechanical load and battery voltage loss, modular battery pack design for electric aircraft, finite element analysis	18. Distribution Statement This document is available to the U.S. public through the National Technical Information Service (NTIS), Springfield, Virginia 22161. This document is also available from the Federal Aviation Administration William J. Hughes Technical Center at www.faa.gov/data_research/library

19. Security Classif. (of this report)	20. Security Classif. (of this page)	21. No. of Pages 87	19. Security Classif. (of this report)

Contents

Figures

Tables

Acronyms

Acronym	**Definition**
Al	aluminum
BMS	battery management system
COT	commercial-off-the-shelf
CAGR	compound-annual-growth-rate
EAV	electric air vehicles: (EAVs)
EC	carbon epoxy composites
EPA	Environmental Protection Agency
eVTOL	electric take-off and landing aircraft
EVs	electric vehicles
FAA	Federal Aviation Administration
FEA	finite element analysis
GAMA	General Aviation Manufacturers Association
ICE	internal combustion engine
LIB	lithium-ion battery
LFP	lithium iron phosphate
NASA	National Aeronautics and Space Administration
Ni	Nickel
NMC	nickel manganese cobalt
NCA	nickel-cobalt-aluminum oxide
OCV	open-circuit voltage
P	parallel: (P)
PES	polyethersulfone
PLA	polylactic acid
S	series
SOC	state of charge
SOH	state of health
Ti	Titanium
TMS	thermal management system
TR	thermal runaway
TGA	thermogravimetric analysis
UDRI	University of Dayton Research Institute
UDOS	urban dynamometer driving schedule

Executive summary

The Federal Aviation Administration (FAA) funded project 692M15-20-C-00014 involves selecting Li-ion batteries (LIBs) with high-performance (hundreds of cycles (05C to 2C rates), >250 Wh/kg energy) and high-safety (should not catch fire). It also provides guidance to modularize LIB packs in small sizes that can be distributed structurally in an aircraft and operated at ambient conditions (temperature and pressure). Distributed small-form-factor batteries can improve battery endurance, safety, and energy efficiency. LIBs in small form factors that are spatially distributed in an aircraft will experience significantly less thermal stress and require less thermal management than large battery packs.

The small form factor LIB modules need an enclosure that helps in easy thermal diffusion to maintain battery temperature, enabling easy serviceability, and protection from mechanical abuse or collision. At the same time, the new battery enclosure must be lightweight and have minimal wall thickness so that battery-specific and volumetric energy densities are not compromised and enable natural battery temperature control. The increase in the overall weight of the battery system due to the secondary enclosure must be nullified by removing the customarily-used thermal management system (TMS). The TMS for a large battery pack can be more than 30% of the total weight of the battery system. Moreover, small LIB modules will enhance the reliability of the power system; if one module fails, plenty of others will support the power demand. It will significantly improve fire safety, as fire from small and single modules would be minimal and can be managed with portable fire extinguishers if the batteries are accessible.

Plastic, carbon-fiber-epoxy composites, and metals are the three most common materials for building battery enclosures. They all have merits and demerits. Plastics are lightweight but weak in mechanical strength and can melt at low temperatures. Composites can be mechanically robust but require significant thickness to provide the necessary mechanical strengths and are not easy to machine. Metals possess all the properties needed for a battery enclosure if the weight of the enclosure can be controlled. In this project, we have focused on metals ideal for a battery enclosure that provides high mechanical strength and high thermal conduction while still offering a competitive weight advantage when used in an optimal wall thickness.

To provide a quantitative basis for why metal enclosures should be considered for future electric aircraft, we studied in-situ mechanical abuse, such as indentation, compression, and fatigue, and its effect on the LIB cell's thermal and electrochemical behavior. Based on mechanical-thermal-electrochemical data, we optimized the thickness of the most valuable metals for the battery enclosure to protect the LIB from thermal runaway (TR). The experiment results were further verified using finite element analysis and then further analyzed to understand the modes of failure.

Based on experimental findings, we provide a new design for building modular LIB packs that can be naturally thermally managed, improve serviceability, reduce the chances of total failure of the power system in case of failures of a few LIB cells or modules, and provide protection from mechanical damages, hence provide overall better functionality and safety.

1 Introduction

Electric air vehicles (EAVs) will be at the heart of the development of green aviation for decades to come. Research on the life cycle assessment of all-electric aircraft compared to fossil fuel-based aircraft shows that the former will have advantage of lowering air pollution than later in long run (Rickard Arvidsson, 2024). Besides noiseless, EAVs also presents advantage over fossil fuel-based aircraft in terms of energy saving (Stefan Baumeister, 2024). The combined factors of energy saving and reducing air pollution is the main reason for the development of electric aircraft which is very active globally. For example in the United States i) the National Aeronautics and Space Administration (NASA) completed the high-voltage functional ground test of Maxwell" X-57 electric aircraft in 2023, ii) Ampaire's nine-seater e-caravan normal-class aircraft in undergoing airworthiness certification process, iii) In 2022, Volocopter's VoloConnect fixed-wing passenger aircraft in the United States completed its first flight, and iv) In 2022, the electric vertical take-off and landing (eVTOL) aircraft of Joby Company of the United States formally applied to the United Kingdom to submit an airworthiness application. Development of EAVs is also active in Europe and Asia. Example, i) The European VELIS Electro, an electric training aircraft, earned the full type certificate of light sports aircraft from the European Union Aviation Safety Agency (EASA) in 2020, ii) In 2022, the "e-Sling" electric plane developed by the Federal Institute of Technology in Zurich, Switzerland, completed its first flight, iii) In 2024 China's EHang Holdings Limited completed first passenger flights in Thailand using EH216-S pilotless electric vertical takeoff and landing ("eVTOL") aircraft. According to the General Aviation Manufacturers Association (GAMA) estimate, over 30 electric aircraft will be awarded type certificates worldwide before 2025 (Cardone, Gargiulo, & Fornaro, 2021).

The commercial LIB is the most promising in developing green aviation due to its advantages of high specific energy, high power density, high cycle life, low self-discharge, and lower (than jet fuel) environmental impact (Schöberl, Ank, Schreiber, Wassiliadis, & Lienkamp, 2024). However, whether the LIB is used as backup power in traditional aircraft or propulsion energy in EAVs, the safety of a LIB is still a concern. The inherent safety problem of LIBs is primarily due to the use of flammable liquid electrolytes and low-melting plastic separators. When there is a need to maximize the size of LIBs to meet energy and power demands, this problem is magnified. A large battery pack presents a risk of thermal runaway (TR)(i.e., battery fire) when operated in unsafe conditions or with mechanical damage. TR is extremely difficult to manage once started, even with an advanced battery management system (BMS) and battery thermal management system (TMS).

To maximize LIB use on aircraft while minimizing battery fire risk, one must consider new design rules for making smaller battery modules that must be protected with mechanically strong and thermally/corrosively stable secondary (battery) cases before distributing them across the aircraft structure. Smaller battery modules pose a lesser fire threat by allowing for a higher chance of extinguishing the fire or minimizing flame spread to the rest of the aircraft. When modules are spatially separated, the chances of TR can be eliminated. There are numerous potential advantages to this approach:

- Smaller battery modules can fit in smaller locations that are impractical for seat passengers or cargo storage, so potentially more total amp-hours of battery charge can be stored on the plane taking advantage of these empty locations.
- Smaller batteries can take advantage of natural, on-board convective and conductive cooling, thus saving weight and cost by eliminating battery TMS.
- When smaller batteries fail/wear out, they can easily be replaced rather than removing an entire large battery pack with 1-2 bad cells.
- The fire risk is minimized when a single small battery fails compared to a large battery pack; failure (heating) in one battery of a large battery pack can propagate to all battery cells in a battery pack, resulting in a large-scale battery fire.
- Smaller batteries dispersed around the aircraft structure bring localized redundancy to other aircraft subsystems.
- Smaller batteries dispersed around the aircraft potentially open up other future power capture systems for direct local charging, such as thermoelectrics near hot components and solar panels on wing and outer skin areas.

Our proposed effort was mainly focused on in-situ mechanical-electrical-thermal testing of ranged structural materials in contact with LIB cells that can be applied as enclosures for safe, small, naturally thermal-controlled LIB modules during regular operation and in the event of a plane crash. The effort included

1. An EAV survey that identifies:
    a. which EAVs would most benefit from distributed small form factor electrical power design rules.
    b. the types of batteries used in the selected EAVs for overall better energy, power, and safety.

   c. the needs of new battery configurations (individually dedicated to power take-off, cruise, dash, and landing/runway drive) to minimize the current practice of over-designed battery redundancy, which should improve fuel efficiency and help with safety (in flight and post-crash).

2. Materials identification for mechanically robust, thermally conducting, and low-weight battery enclosures. The final selection of battery enclosure is based on detailed mechanical-thermal-electrical studies on different types of LIB cells.

The mechanical-thermal-electrical data obtained and verified through theoretical analysis has been used to design a novel modular LIB small pack which, if proven will play a key role in developing power system for a safe electric aircraft. A pack level study similar to cell level study in this project is needed.

2 Survey and challenges of battery-operated aircraft

Batteries power today's most widely used EAVs, (i.e., unmanned electric vehicles or drones). Skyquest (2024) reported that the drone market size was valued at $28B in 2023, $35B in 2024, and projected to reach $208.38B by 2032, growing at a compound annual growth rate (CAGR of 25% during the forecasted period (2025-2032). Most drones use single or double small-size battery modules with a few LIB cells to achieve the desired voltage of less than<30V and energy (watt x time; Wh) in the Wh range, depending on the size and flight range of drones (Shaefer, 2016). Usually, no external thermal control is needed to operate small drones as the battery can be cooled naturally during operation. There has been little effort given so far to ensure battery safety in today's drones, mainly due to the small size and cost of drones in addition to their unmanned nature.

But, tomorrow's EAVs demand much larger battery packs of several hundred volts and energy in the high kWh range to power one to twelve-seat manned aircraft. Battery safety will be essential and most challenging. Table 1 shows some notable companies involved in designing and testing such electric aircraft powered by LIBs, a hybrid of the internal combustion engine (ICE) and LIBs, or a hybrid of ICE and fuel cell. For example, the X-57 Maxwell (Aerotech News, 2020), a fully electric, 2-seater aircraft developed by NASA, was tested to fly with two 460-volt, 400-pound LIB packs that were located in the back of the main cabin. The two LIB packs supplied 46 kWh of power, sufficient for a one-hour, 100 mile flight. EAVs present very different safety issues vs. jet-fueled aircraft. Hence, surveying aircraft helps the FAA know what aircraft could benefit from improved design rules that maximize aircraft range while simultaneously reducing hazards brought by large battery packs. Further, EAVs are very new technology, and the designs are constantly changing, which makes for a more complicated design space to consider.

Table 1. Worldwide efforts to develop and advance electric/hybrid aircraft.

Company / Government institutions – Country of Origin	**Aircraft type**
NASA's X-57 Maxwell – USA	Fully electric (2 seater) – tested – Li-ion
Pipistrel's Velis Electra – Slovenia	Fully electric (2 seater) – certified (EASA.A.573 TCDS) – Li-ion
Eviation's Alice – Israel	Fully electric (9 seater) – tested – Li-ion
Ampaire's Electric EEL – USA	Hybrid (electric + combustion) – test in progress
Mokulele Airline	9-seater electric engine
Bye Aerospace – Denver, USA	Two seater – electric
Zunum (backed by Boeing & JetBlue)	12 seater hybrid
Airbus's – Netherland	Hybrid & Electric
Wisk's backed by Boeing – USA	Hybrid & Electric (urban mobility, cargo, defense, space)
Rolls Royce (fastest electric aircraft tested)	All electric (1 seater), Li-ion (6,000 cylindrical cells)
Chinese-made RX4E aircraft	All electric (4 seater)
Volt-Aero, France	Hybrid (9 seater)

Despite successful test flights of several EAVs, the commercial operation of manned EAVs will require much longer flight operation (>500 miles) that will require either 4-5 times larger battery packs or a smaller battery packs with 4-5 times improved energy density. Larger battery packs are not commercially viable because they leave less space for passengers and cargo. Achieving a 4-5 time energy-dense battery, from the current ~150 – 200 Wh/kg at the system level, will require invention of new battery chemistry beyond LIB. Larger battery packs, like the ones on board the X-57, require strict thermal management for safety and specialized mounting brackets, which add weight, to hold the battery in place during flight. Another problem with large battery packs located in one central location of the aircraft is that wiring may have to be laid out from the central location to feed power from the battery to various operations located at distinct places of the airplane. If the main battery pack fails, all systems fail, thus creating too much reliance on a central battery "powerplant" for the entire aircraft. Using larger batteries also restricts the number of sites in an airplane where the battery can be placed to maintain the EAVs's center of mass. Usually, larger battery packs are placed in the center/interior of the fuselage to balance out the aircraft, but this restricts easy battery swapping and maintenance operations. Moreover, the current approach has a single battery design trying to meet all the different power requirements (take-off - high power, cruise – medium power, dash – medium power, landing – low power, etc.) that brings a high level of battery redundancy and reduced fuel efficiency. Finally, large battery packs, should they go into thermal runaway or be damaged upon crashing, present severe fire and explosion hazards not seen with more miniature battery packs.

For the above reasons, a comprehensive solution that considers improved energy, power, cycle life, and safety, along with engineering rules on distributed battery systems, will help meet the needs of future EAVs. The new designs should consider more miniature battery packs that can be specifically designed for a particular power demand while distributed throughout the fuselage to maintain aerodynamics and be located near systems requiring power such as motor, avionic, electronic speed controller, avionics, communication module, etc. This reduces the need for a central power plant and could take advantage of wing space for power storage via thin-film battery packs, as is accomplished today with fuel inside the wings of traditional aircraft. The solution should also consider taking advantage of the structure of the aircraft for potential secondary containment of distributed batteries and access to the battery packs for maintenance and safety (post-crash fire events or other fire events, including in-flight venting). The comprehensive solution covers many different variables, and the design rules solution may likely have to be tailored to a specific aircraft frame/shape rather than be generic to all aircraft.

Overall, designing and implementing the distributed LIB system concept in future EAVs to solve the problems above will require a holistic approach, some of which are presented in the following sections.

3 Selection of battery and associated components

Criteria for battery selection was related to the design and testing of efficient battery integration architectures, including i) understanding the power and energy needs of EAVs (e.g. Altavian F7200 drone); ii) selection and procurement of LIB cells with different cathode chemistry, size of cells, and packaging; iii) selection and procurement of battery fault diagnostics, including temperature and pressure sensors; iv) selection and procurement of potential battery casing materials and v) design of test layouts/test plans.

3.1 Power and energy need for battery-operated EAVs

When considering power systems for EAVs, there are multiple factors, including size/weight of the EAV, weight of the payload, flight altitude, flight speeds, mission duration, weather conditions expected for flight, and power draw from flight control and communication systems. (Kim, Perry, & Ansell, 2018). For example, a conventional fixed-wing EAV with landing gear capability will have different power/energy demands than an eVTOL EAV. An EAV's energy/power demand can be met using a single battery pack for energy and power needs or two or more smaller battery packs, one for power and the other for energy needs. For example, Figure 1 shows the power profile of the fixed wing, hand-launched Altavian F7200 drone with an empty weight of 4.4 kg, a payload weight of 1.6 kg, and a battery weight of 1.3 kg. A single LIB pack (22.2V and 11 Ah) was used for the entire flight operation (Shaefer, 2016). Since this is a hand-launched drone, there are only a few high voltage drops (i.e high current draw from the battery) during the initial launch period, possibly when the engine starts with the surge in current output from the battery. Most of the flight duration results in slow voltage drop as the current drain during this period is lowest. There are few sharp voltage drops during the landing period due to higher power needs.

However, the power profile can significantly change for self-operated drones that involve auto take-off and landing, such as vertical take-off and landing EAVs, or larger EAVs like NASA’s X-57, which has take-off and landing gear operations. Therefore, understanding and measuring a particular EAV's power profile is critical for designing the batteries that will power and propel that EAV. If the profile is unknown, creating the right battery system for that aircraft becomes increasingly challenging.

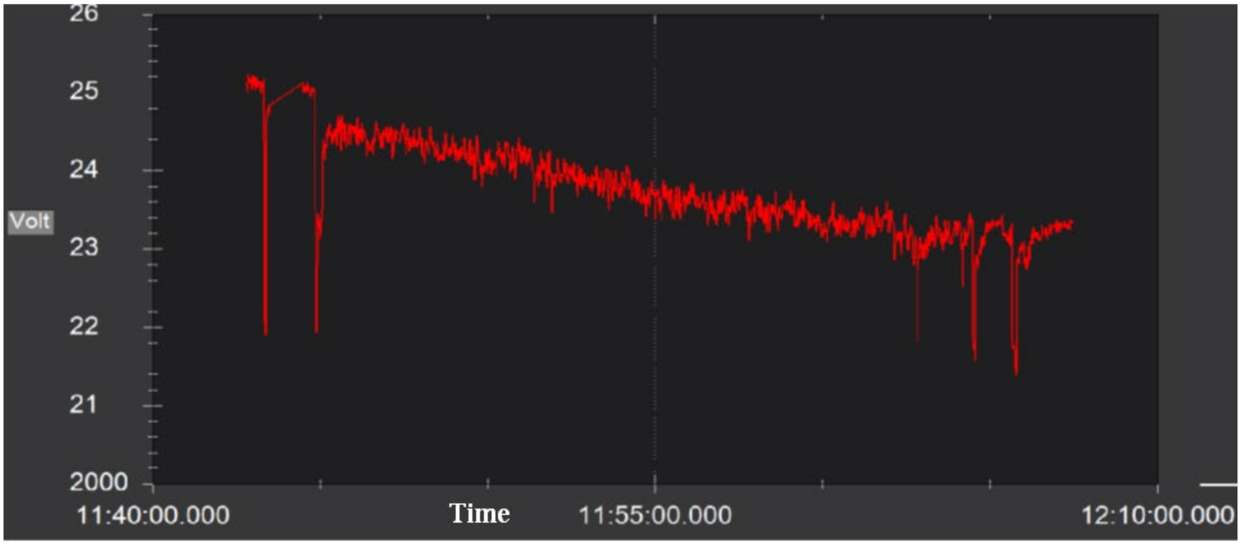

Figure 1. The power profile (volt vs. time) of Altavian F7200 operated using a single LIB pack

Figure 2 shows the power profile of an eVTOL EAV, the E400, Event38 Unmanned System (Shaefer, 2016), where battery 0 (B0) was used for high-power operations such as take-off and landing, and battery 1 (B1) was used for energy operations such as cruise and dash .

The B0 module consists of 8 LIB cells connected in series (8S). Each LIB cell has a capacity of 3.25 Ah and a maximum voltage of 4.3V. B0 is a power module that delivers energy at high rates during eVTOL takeoff and landing.

The B1 module consists of 40 LIB cells. Each LIB cell is an 18650 cylindrical cell with a capacity of 3.3 Ah and a maximum voltage of 4.3 V. All 40 cells make four series (S); each series string contains 10 cells (10S). Finally, all four strings are connected in parallel (P), constituting an energy pack (10S, 4P) with a total capacity of 13.2 Ah and a maximum voltage of 43V. B1 is an energy pack that delivers the desired power during the cruise and dash operation of eVTOL.

Power pack B0 delivered energy at an extremely high rate of ~14 C for a short period, whereas energy pack B1 delivered energy at a low rate (1.2 - 0.5 C) but for most of the flight period. 1C rate means battery charge or discharge in 1 hour.

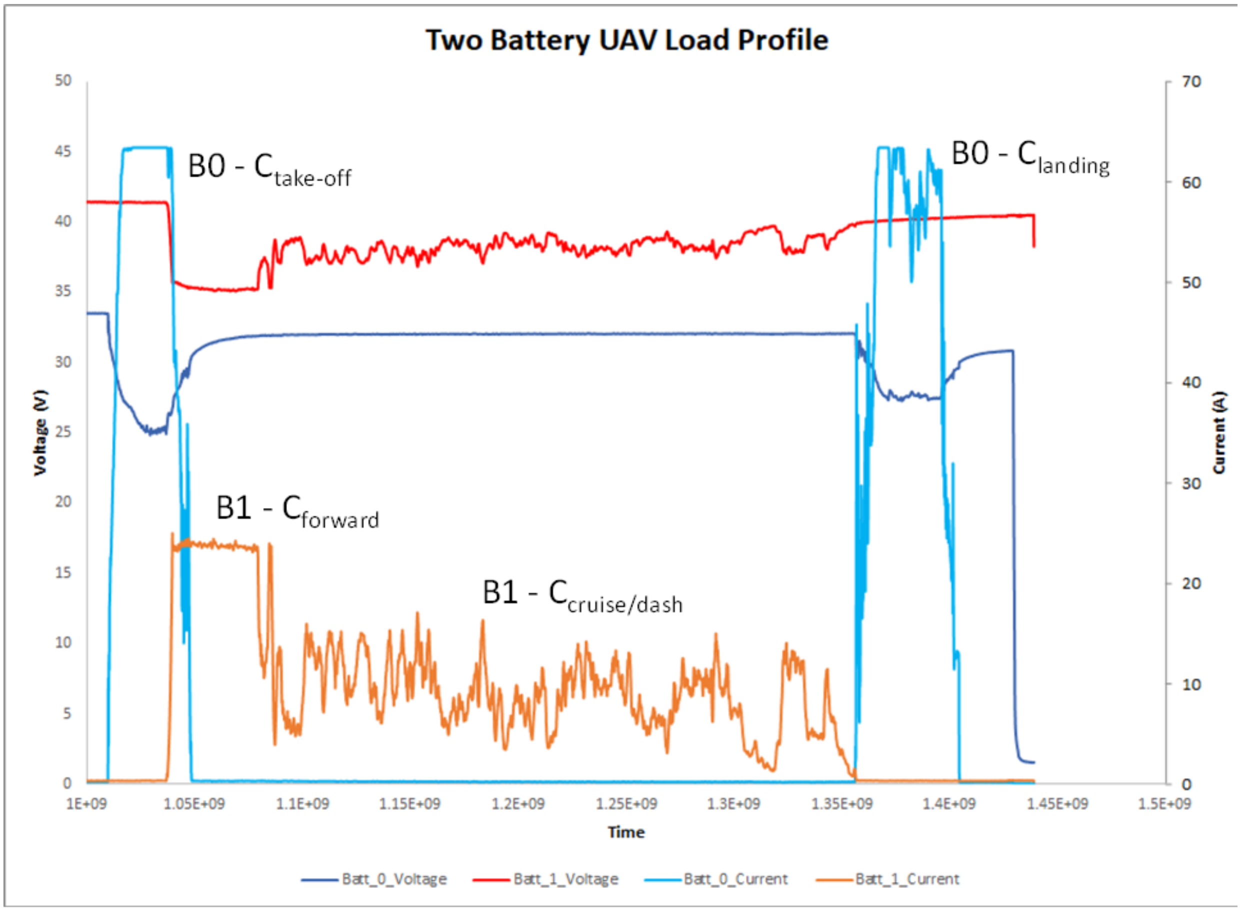

Figure 2. The power profile of E400-eVTOL using Li-Po (battery 0, B0) for take-off and landing and LIB (battery 1, B1) for forward thrust, cruise, and dash

Designing dedicated power and energy packs (Figure 2) for EAVs over a single battery pack (Figure 1) can have multiple advantages:

1. protection from excess heating of the entire pack during high power drain,
2. longer battery life as energy and power sub-modules work within their designed operating range,
3. reduce battery redundancy as a single battery pack is generally over-designed to take care of both power and energy needs, and thus, cells may not be used to their maximum potential, etc.

Power packs will play a crucial role as EAVs grow (larger) and need more mileage on a single charge. The advantages of using dedicated battery sub-packs for energy and power include enhanced energy efficiency and safety, essential for any EAV's success. The trade-off of designing battery packs like Figure 2 may lie in the complexity of BMS design, where robust communication and fail-proof switching between energy and power packs will be an absolute necessity.

3.2 Battery selection for energy-efficient and safe EAV operation

As discussed in Section 3.1, one can choose a single battery for energy and power or two batteries, one designed for power and another for energy. Furthermore, the common practice is to select one chemistry for building a battery pack; for example, eVTOL data presented in Figure 2 used LIB cells as energy and power sub-module design, though in different formats. One is a pouch cell (power pack) and the other is a cylindrical format (energy pack). There is the advantage of using single chemistry in battery pack design, as this provides options for choosing simple and less complex BMS control circuitry because of the same charge/discharge voltages of individual LIB cells.

However, no LIB chemistry can provide all the desired characteristics, such as high energy and power with high safety. For example, an LIB based on transition metal oxides such as nickel manganese cobalt (NMC is considered a high-energy LIB (200-300 Wh/kg cell level) with moderate power and medium safety. On the other hand, an LIB based on lithium iron phosphate (LFP) is considered a high-power, moderate-energy battery (~150 Wh/kg cell level) with higher safety than an NMC-based LIB.

Figure 3 shows specific energy densities (in Wh/kg) of three different commercial off-the-shelf (COT LIBs, nickel-cobalt-aluminum oxide (NCA) 18650 from Panasonic, and LFP 18650 and LFP 26650 from K2 energy. Each were tested at different C-rates at room temperature. At lower C-rates, NCA 18650 provides the best energy density, but as the C-rate for high power increases, Wh/kg decreases rapidly. Both LFP 18650 and 26650 overtake NCA 18650 in terms of Wh/kg when the C-rate increases beyond the 1C rate. Noticeably, within LFP chemistry, a thicker cell like LFP 26650 yields higher energy density than LFP 18650, but LFP 18650 provides better C-rate capability.

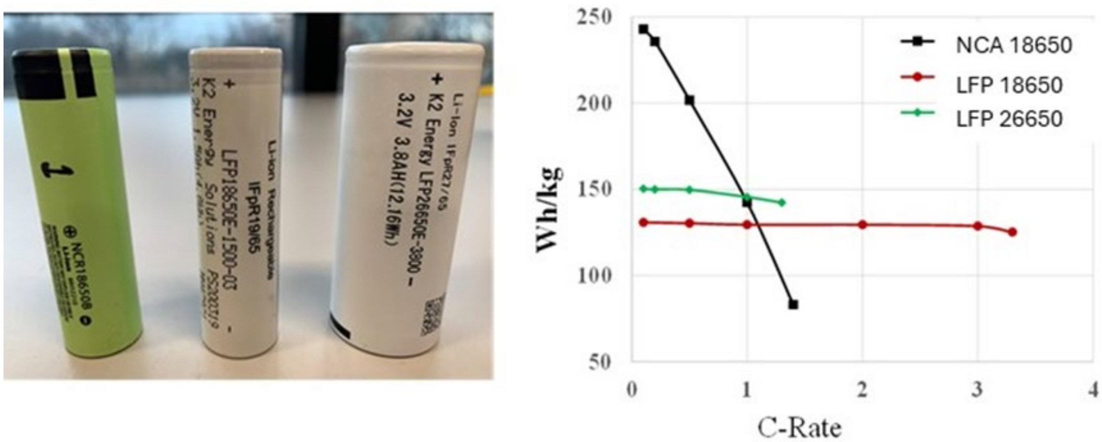

Figure 3. Energy vs rate performance of COTs LIB cells.

Data in Figure 3 was obtained with constant current (CC) charge and discharge. However, as shown in Figure 2, EAVs, may experience variable current battery discharge, with high current drain during take-off and landing and moderate current drain during dash/cruise. Thus, we decided to test the different chemistry cells of Figure 3 in electric vehicle (EV) test conditions using the United States Environmental Protection Agency (EPA) Urban Dynamometer Driving Schedule (UDDS (Dynamometer Schedules, 2023). Data of cells tested with UDDS is shown in Figure 4. UDDS involves battery charge in CC mode and discharge in series of high current pulses and few charge pulses in between discharge pulses. The idea of including charge pulses between discharge pulses is to account for occasional battery charge due to vehicle deceleration (break). When NCA and LFP battery cells were tested using UDDS the later (Figure 4 - dotted green curve) performed better than former (Figure 4 – dotted red curve).

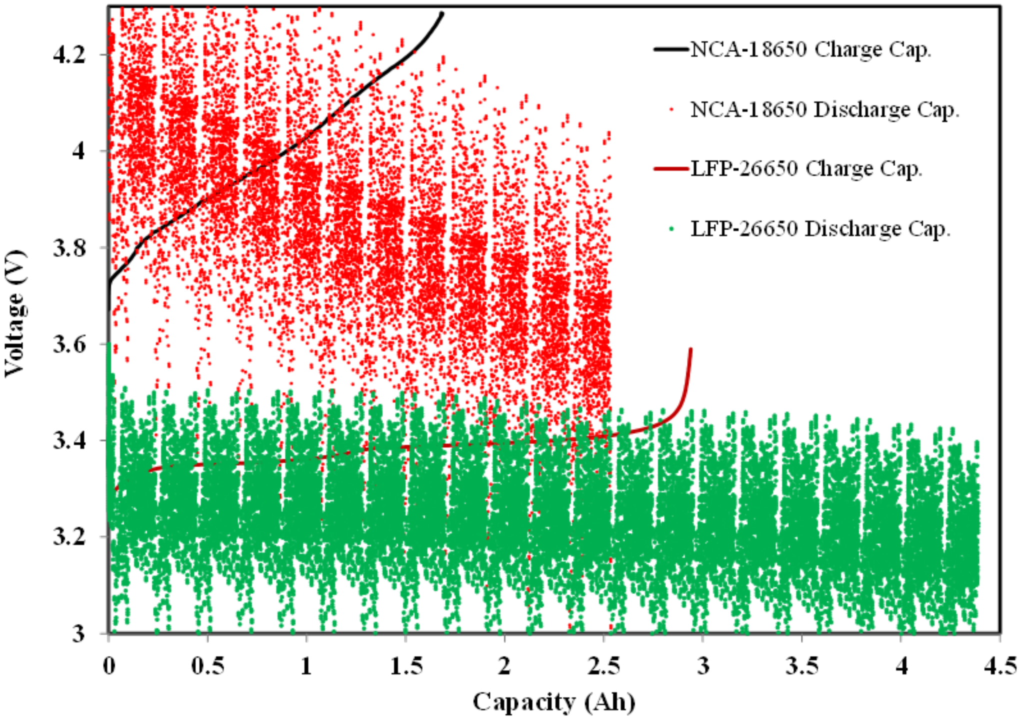

Figure 4. Constant current (CC) charge and UDDS discharge performances of NCA and LFP-based COTS LIBs.

Performance data in Figures 3 and 4 and varying requirements from Figures 1 and 2 suggest that battery power systems must be designed according to energy and power needs. A single LIB chemistry battery can be created in different formats, such as energy and power sub-modules. An energy sub-module can be designed by selecting an LIB based on an NCA cathode that is best suitable for high energy. A power sub-module can be created using an LIB based on an LFP cathode, which is ideal for high power. With this new design, the best of two or more different LIB chemistries can be integrated to maximize the power and energy of EAVs.

This customized design may prove the best combination for a safe energy storage system, as none of the individual sub-packs has to work beyond their limit where they can experience fast cell degradation accompanied by unnecessary heat generation and, hence, reduced safety.

3.3 Battery distribution and battery control circuit requirements

If properly designed, a BMS ensures the proper functioning of the battery, thus enabling safe operation throughout its regular use and battery lifetime. The BMS is comprised of various sensors that inform users of the status of voltage, current, temperature, resistance, state of charge (SOC), state of health (SOH), and other relevant battery features. This system enablessafe battery operation and informs users when the battery recharging is needed before device/system/EAV shutdown. Pressure and gas sensors can be added to BMS circuitry to indicate unsafe pressure build-up inside the battery (or individual cell) and identify any gas formation due to battery material degradation . This could allow a battery can be decommissioned before it goes into TR or fails in use. As in most cases, battery repair may not be feasible to allow the battery to return to service after sensors detect gas buildup.

In addition to battery function control, the BMS can be integrated into power control circuitry, especially for large battery operation or for batteries that involve switching between various power sources (Figure 2). In the design depicted in Figure 2, the power module must switch to the energy module without time lag and vice versa, as eVTOL changes the function from take-off to cruise or cruise to landing. Similarly, for distributed battery systems, which are the subject of study for this project, a robust BMS and power circuit design will be required to ensure all the distributed small battery sub-modules work optimally and safely in tandem.

3.4 Battery containments for energy-efficient and safe EAVs operation

Li-ion cell components are enclosed in a cell case made of either plastic/aluminum foil/plastic laminate (pouch format) or thin stainless steel (SS) (cylindrical or prismatic formats). Primary cell casings are now standard, and little research is being conducted to develop new ones. In contrast, secondary casing, known as a battery case, is an evolving research and development field, especially for larger battery applications in EVs and EAVs. The secondary battery casing relates to the casing used to house the entire group of cells, battery control hardware, and TMS in one enclosure. It is a critical component of the power system that plays a vital role in ensuring safety, including the containment of TR. The requirements for the secondary battery casing include:

1. providing mechanical support to all components of the battery pack (battery cell, BMS, TMS, wiring, cell insulation, etc.);
2. protecting battery components from mechanical abuse and harsh environmental conditions;

3. enveloping battery fire and smoke during a TR event,
4. stopping ejecta from burning a cell to minimize mechanical damage of a neighboring cell, and
5. protecting the battery pack from becoming involved in a post-crash fire event (i.e., protect against relevant FAR 25.853 fire tests for EAVs).

Secondary battery enclosures can be made either of plastic, carbon composites, metals, metal/plastic composite laminate, or carbon fiber composite laminates. These materials have strengths and weaknesses and can be selected based on application and safety requirements. Plastics are lightweight and cost-effective but have low melting points and inferior mechanical strength and, may not fully ensure safety during a TR event or crash, especially for EAV applications. Carbon fiber-epoxy composites have better thermal and mechanical protection than plastics but may not protect from a TR event. Metals embody the best overall characteristics to ensure battery safety during TR events but are considered to be costly and heavy. This project has proven superior protection by metals over plastics and carbon composites through testing. Metals, can be weight effective if selected wisely and optimized for thickness. The majority of efforts in this project involved understanding the mechanical behavior of secondary enclosures and their effectiveness in ensuring battery safety, which will be presented in the subsequent sections. Before that, we discuss below some of the advantages of metals as battery enclosures.

3.4.1 Metals as secondary enclosures

Stainless steel (SS) has been used by Boeing as a secondary casing for LIB packs to minimize damage from TR events in aircraft batteries (Skillings, 2013). To a certain extent, SS containers can protect or at least reduce the aircraft damage from an internal battery fire during a TR event by starving the battery fire from external oxygen, assuming the SS container is not punctured or damaged. SS containers can also store some battery fire gases, provided critical pressure limits are not exceeded. However, due to the heaviness of the container, a range of alternative metals including aluminum (Al), titanium (Ti), and nickel (Ni) were also tested. It was concluded that Ti (melting point 1668°C, 56% lighter than SS, extreme corrosion resistance) can be a far better battery enclosure than the other tested metals because of its superior thermal and mechanical properties. However, Ti is slightly costlier than SS, Ni, and Al. The thermal and mechanical properties of Ti are discussed in Section 4 and Section 5, respectively.

3.4.2 Carbon-epoxy composites

Carbon-epoxy composites (EC), widely used to build aircraft structures, can be used as a secondary battery container. The EC can be lighter than Ti, but Ti (6.6 W/m-K) has higher thermal conductivity than the airframe (0.23 – 0.24 W/m-K). Thus, a combination of carbon-fiber and Ti sheet multilayer structure in which the best airframe and Ti can be realized would be another option for secondary cell casing. Mechanical property differences of Ti and EC would need to be compared to determine when the composite is the best material for battery containers vs. Ti, or if a mix of the two makes sense for specific locations on the aircraft. The FAA may explore this option in the future.

4 Thermal properties of plastic, composite, and metal enclosures

In this section, we summarize the thermal behavior of different enclosure materials and underline the role of enclosure in natural thermal management.

4.1 Thermal properties of different enclosure materials

An enclosure with higher thermal conductivity will reduce heat build-up around the battery cell by faster heat dissipation and enable natural heating-cooling. Heat build-up around a battery cell can harm its performance and safety. Tables 2 and 3 give the thermal conductivity of polylactic acid (PLA) and composite (20 wt% carbon fiber in polyethersulfone (PES)), respectively. Figure 5 compares the thermal conductivities of PLA plastic, carbon nanofiber-PES composite, and Al (and Al-alloy (Zhang & Li, 2023)).

Table 2. Temperature-dependent thermal conductivity of PLA.

Temperature (°C)	Thermal Diffusivity (mm^2/s)	Specific Heat (J/g K)	Thermal Conductivity (W/m K)
22	0.099	1.086	0.128
50	0.096	1.366	0.156
75	0.067	1.653	0.132
100	0.070	1.396	0.116

Density: 1.19 g/cc

Table 3. Temperature-dependent thermal conductivity of 20% CF-PES.

Temperature (°C)	Thermal Diffusivity (mm^2/s)	Specific Heat (J/g K)	Thermal Conductivity (W/m K)
22	0.485	1.002	0.573
50	0.478	1.096	0.618
75	0.469	1.122	0.621
100	0.461	1.169	0.636
125	0.452	1.222	0.652
150	0.443	1.288	0.673

Density: 1.18 g/cc

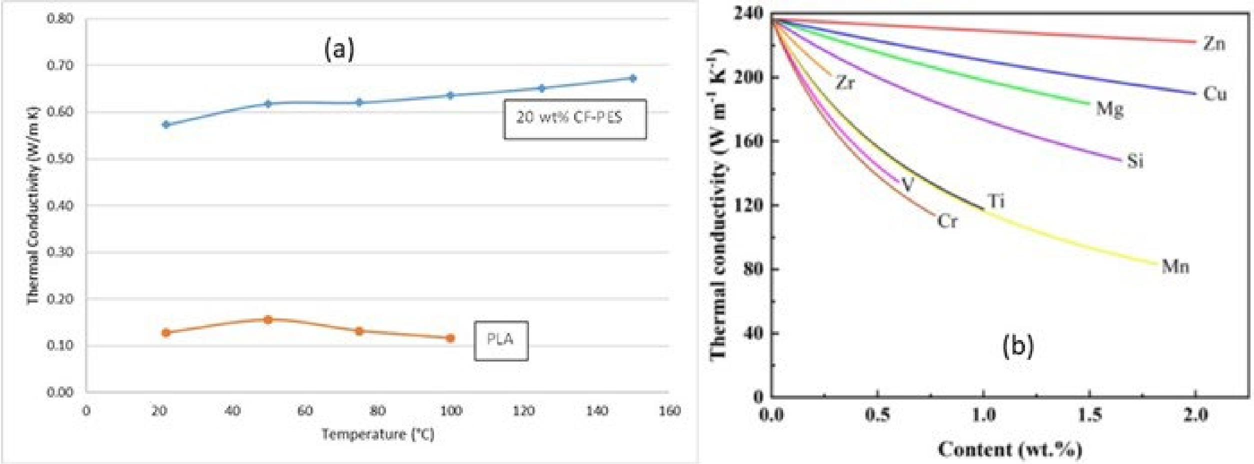

Figure 5. (a) Thermal conductivity comparison of 20 wt% CF-PES composite and PLA plastic. (b) Room-temperature thermal conductivity of Al (and Al alloys (Zhang & Li, 2023)).

Results from Figure 5 and Tables 2 and 3 show that the thermal conductivity of 20 wt% CF-PES is >5 times higher than PLA, and hence, the former is expected to diffuse heat from the battery under charge and discharge faster than the latter. Moreover, the thermal conductivity of Al (236 W/mK, room temperature, RT) is 412 times higher than 20 wt% CF-PES. Thus, Al can be selected among Al, CF-PES, and PLA for better thermal conductivity. But, PLA and CF-PES have a weight advantage. The density of CF-PES is lowest among 20 wt%CF in PES (1.18 g/cc), PLA (1.19 g/cc), and Al (2.7 g/cc).

Another choice is laminate of Al and CF or Al and PLA or other plastics. Figure 6 shows thermogravimetric analysis (TGA) of PLA (red curve) and 20 wt% CF in PES (black curve) in air. PLA loses most of its mass below 350°C, whereas 20 wt% CF-PES loses 4-5 % mass up to 500°C. Thus, the latter is thermally more stable between PLA and CF-PES than the former. However, Al melts at 650°C but does not decompose up to 1250°C (Ding, Wang, Luo, & Li, 2020) and is thus considerably thermally more durable than both PLA and CF-PES. Regardless, none of the above will be ideal as those materials have lower melting points and may not survive the temperature of battery fire, which can be >1000°C. Therefore, this project has conducted a detailed study of various metallic enclosure material options (Table 4), providing the highest protection from mechanical damage, the best thermal conductivity, and the highest temperature stability.

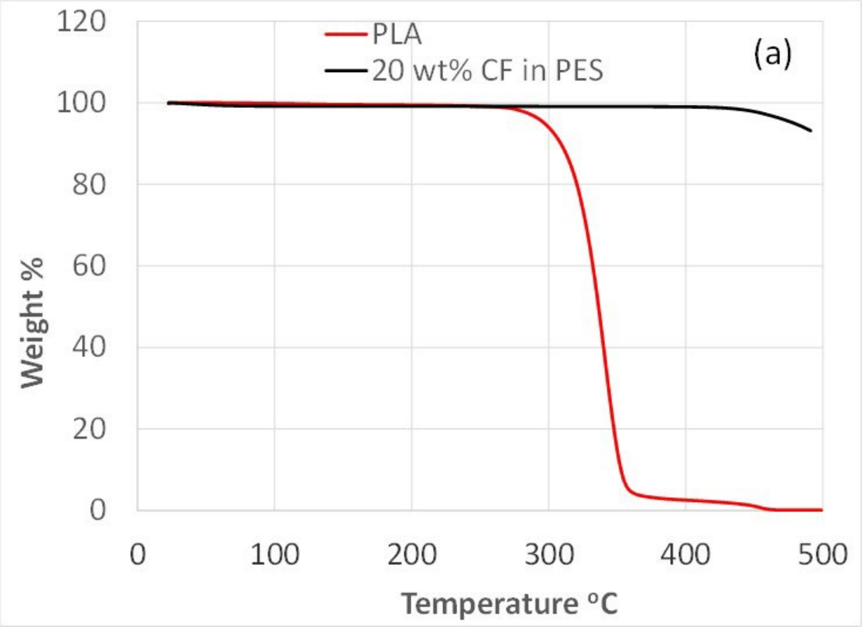

Figure 6. Thermogravimetric analysis of PLA (red curve) and carbon fiber composite (20 wt% CF in PES (black curve) in air.

Table 4. Density, thermal conductivity, and melting point of potential metals for battery enclosure application.

Metals	Density (g/cc)	Thermal conductivity (W/mK) at RT	Melting point (°C)
Plastic	~1.2	0.13	<<1000
Composites	~1.1	0.6	<<1000
Aluminum	2.7	236	660
Nickel	8.9	97	1455
Stainless steel	7.75-8.03	15	1375 - 1510
Titanium	4.5	17	1668

4.2 Role of enclosure in dissipating heat generated during battery operation

Besides determining the best enclosures for high thermal and mechanical stabilities and low weight to enable structurally distributed batteries, it is essential to know how battery enclosure contributes to heat transfer between the battery and surroundings. Depending on the intended battery application, the enclosure can either be heat-insulating or heat conductive. For example, suppose a battery is designed to work in a cold environment. In that case, a heat-insulating enclosure is preferred to reduce the heat energy required to keep the battery temperature around 23°C. On the other hand, an enclosure with high thermal conductivity can allow better natural cooling for a battery intended to be used in the aircraft's interior. For enclosures designed to be used exterior to the aircraft structure, the thermal conductivity of enclosure and insulation used to minimize extreme temperature exposure (cold during flight, potentially hot when on the ground in high temperature locations) will be critical. Below, we provide a few data showing how the enclosure will impact heat build-up.

It is known that the temperature of a battery cell increases with an increase in charge/discharge current. Figure 7 shows heat generation during the cycling of a single LIB cell (2Ah) at increasing current (0.5C (1A/2h) to 2C (4A/0.5h). The cell was cycled outside an enclosure. The maximum temperature of 33°C was recorded when the cell was cycled at 2C rate. This temperature rise can be managed with natural cooling without adversely affecting long-term cell performance for a single cell. However, more cells placed near each other (module) will experience higher temperature rise for the same given C-rate.

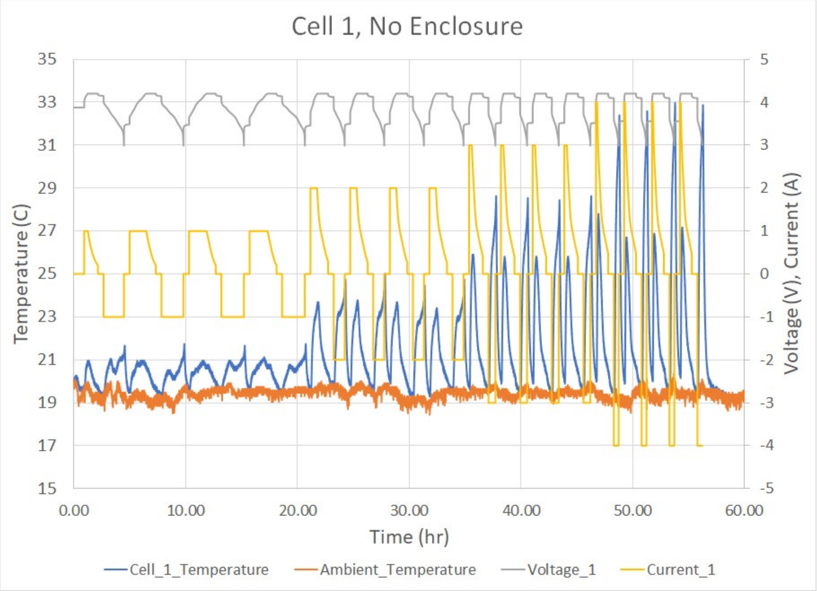

Figure 7. Heat evolution during LIB cell cycling at increasing C-rates (0.5C – 1A/2h, 1C – 2A/1h, 1.5C – 3A/0.66 h), 2C – 4A/.5h).

Figure 8 shows heat generation during the cycling of the same cell as in Figure 7 but inside 20 wt% CF-PES enclosure at an increasing current (0.5C (1A/2h) to 2C (4A/0.5h). The maximum temperature of 42°C was recorded when the cell cycled at a 2C rate, almost 10 °C higher than without an enclosure. Thus, enclosure can significantly affect heat buildup during battery cycling.

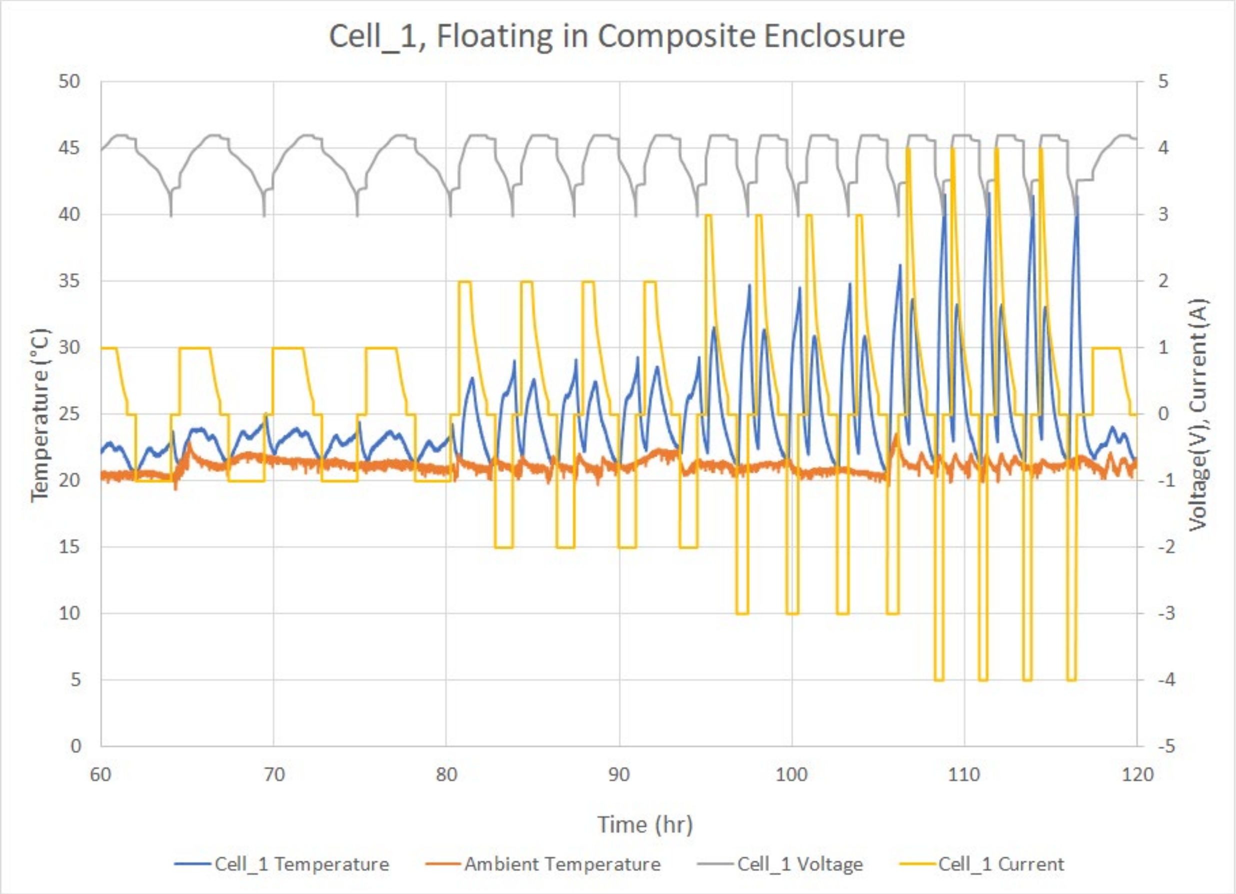

Figure 8. Heat evolution during battery cell, inside a 20wt% CF-PES, cycling at increasing C-rates (0.5C – 1A/2h, 1C – 2A/1h, 1.5C – 3A/0.66 h), 2C – 4A/.5h).

After establishing (in this section) that metal enclosures can play a vital role in fast heat dissipation, hence enabling more natural thermal management, which is one of the central objectives of this project, in the next section, we present the mechanical superiority of metal enclosures over plastics and carbon composites.

5 Mechanical superiority of metal enclosures over plastic and carbon fiber-epoxy enclosures

5.1 Resiliency of pouch Li-ion cells against semi-indentation load

To determine the mechanical strengths of different enclosures, we adopted a standard mechanical indentation method where different enclosures were subjected to load by a semispherical indentor. Here, we show which enclosure offers the most protection to the LIB pouch cells when indented. Figure 9 confirms that the battery with an Al metal enclosure not only withstands the highest load (>55klbf) but also protects the battery from TR when subjected to a load with 0.1 in/min rate. Temperature rise in the cell enclosed in an Al box is only 150°C, whereas cell temperature in both the composite and plastic enclosures quickly rose beyond 500°C and lead battery TR. The plastic box is particularly damaging because the high temperature melts the box, and the melt flows like liquid to transport heat to neighboring cells, facilitating cell-to-cell thermal runaway propagation.

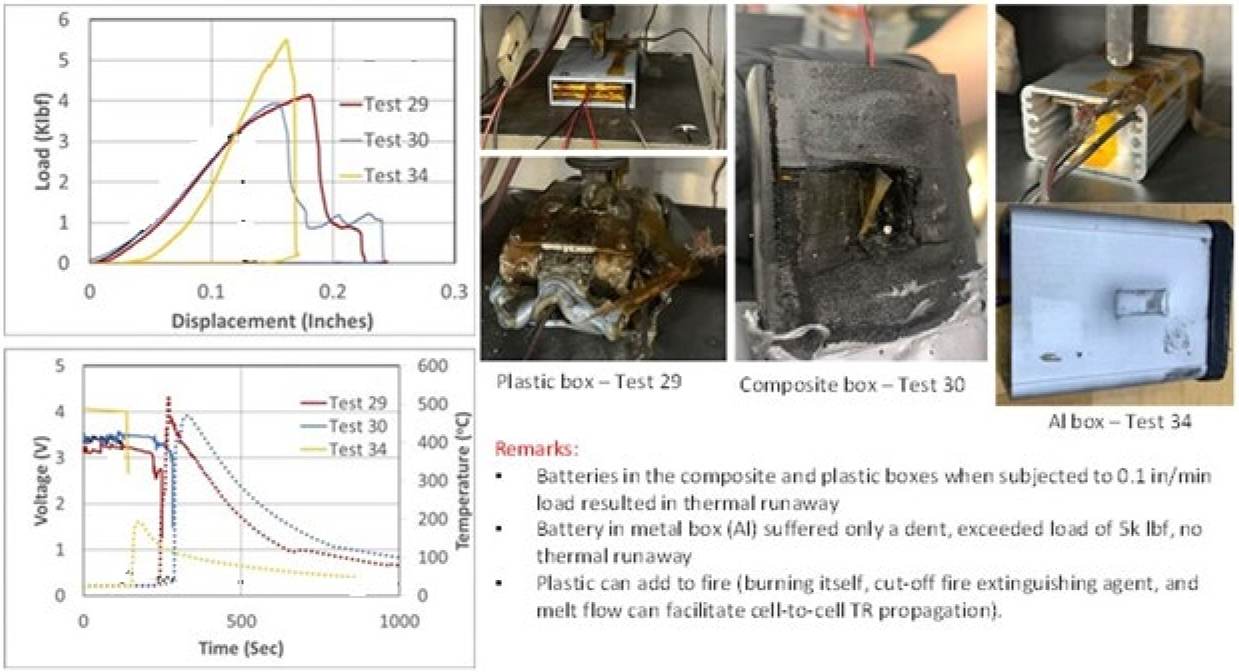

Remarks:

- Batteries in the composite and plastic boxes when subjected to 0.1 in/min load resulted in thermal runaway
- Battery in metal box (Al) suffered only a dent, exceeded load of 5k lbf, no thermal runaway
- Plastic can add to fire (burning itself, cut-off fire extinguishing agent, and melt flow can facilitate cell-to-cell TR propagation).

Figure 9. Mechanical load test results (load vs. displacement, battery voltage during discharge, and temperature rise due to battery damage) on cells enclosed in boxes of different materials (Al - yellow curve; PLA – red curve; and carbon composite – blue curve).

After confirming that metal enclosures can be the best battery enclosures for many reasons, we decided to evaluate the performance of different metals to find out which metal will be the best in *protecting from mechanical damage and also presents an advantage in terms of weight. The weight of an object intended to be used in an aircraft can be the critical selection criteria.*

Figure 10a shows the load-displacement characteristics of two 2 Ah pouch cells stacked together under in-situ open-circuit voltage (OCV) measurement. The maximum load (from 5 mm radius indenter) the sample could take is more than 3k lbf, which is impressive, but the load speed was shallow (0.01 in/min, almost static). The intent of this test was to know how a slow but high load can physically damage pouch cells and the resultant change in the cell's temperature and voltage. Also, the idea of stacking two pouch cells together is to know how the load (damage) will transfer from the directly affected cell to the adjacent cell. Figure 10b shows a slight voltage loss and sharp temperature rise (but no TR) when the indenter load increases on the cell (red circled region). Around the maximum load (>3k lbf), the indenter load starts decreasing as the indenter starts damaging the pouch cell (Figure 10 c (before load application) vs. d (after load application)), and we stopped the experiment. Postmortem reveals a slight depression on the 2nd cell (Figure 10 e and f), but the 2nd cell remains unaffected in its discharge behavior (Figure 10g).

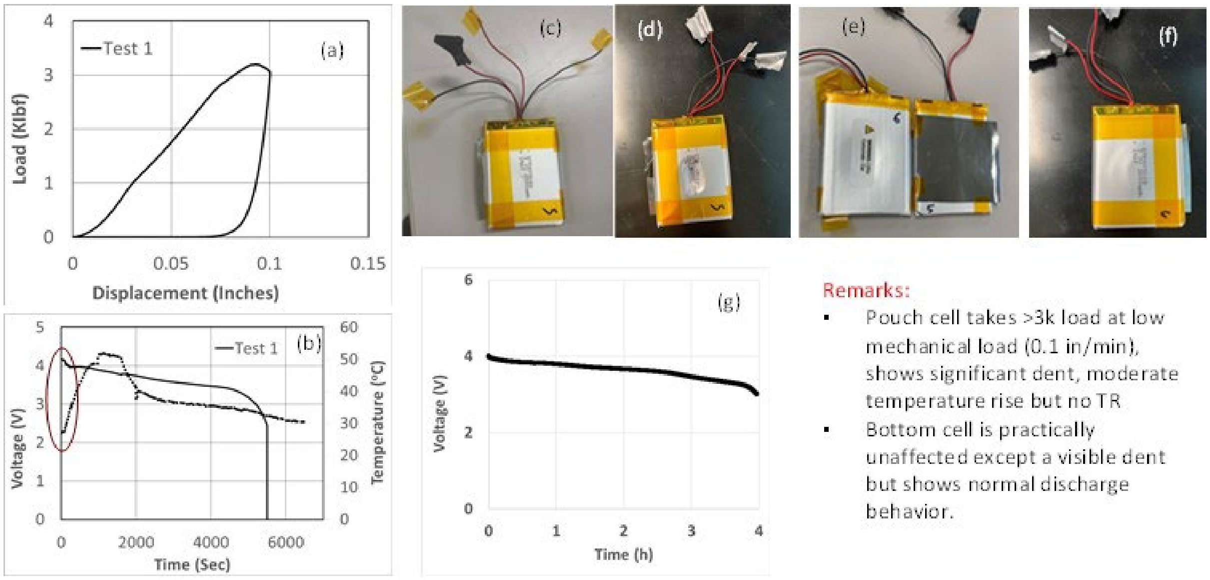

Remarks:

- Pouch cell takes >3k load at low mechanical load (0.1 in/min), shows significant dent, moderate temperature rise but no TR
- Bottom cell is practically unaffected except a visible dent but shows normal discharge behavior.

Figure 10. Effect of mechanical load on voltage, temperature, and physical deformation of pouch cell without secondary protection.

In Figure 10, we determined the effect of slow mechanical load application on the cell's temperature rise when OCV was measured. However, in real world applications, the cell may be charged or discharged when a battery experiences external mechanical load (a collision situation). Figure 11a shows load-displacement characteristics of 2 stacked (2Ah) pouch cells (same as Figure 10), and the result is the same as what we observed in Figure 10a. The critical difference can be seen in Figure 11b; charge and discharge voltage changes are more dramatic than in Figure 13b (OCV measurement). Moreover, *the temperature rise during the discharge (test 2) of a fully charged cell was more than when a discharged cell was under charge* (test 3) at the same C-rate. The remaining tests were conducted on fully charged cells under discharge and mechanical load application. Also, before we performed more detailed mechanical tests, we explored methods to measure temperature accurately (Figure 12).

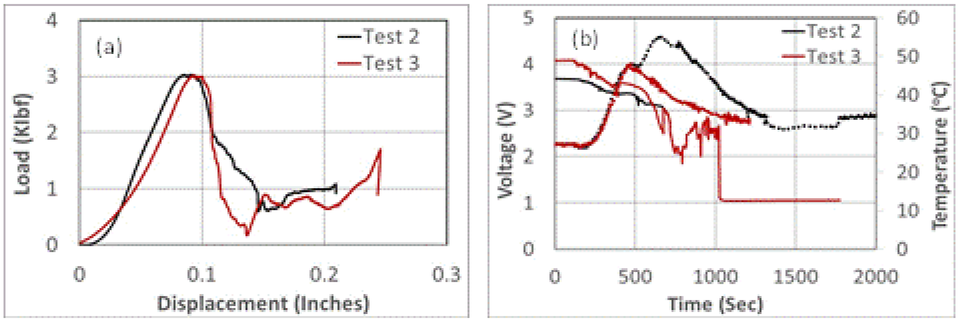

Figure 11. Effect of mechanical load on charge and discharge voltages and temperature of pouch Li-ion cell.

Figure 12 shows the advantage of using a thin metal foil (~20 µm) between stacked cells. Temperature measurement using only a metal tab at the edge of the cell (Figure 12c) not only delays sensing the temperature but also slows down. The battery remains elevated for a longer time as the dissipation of battery core temperature is slow since the pouch materials are not good heat conductors. On the other hand, a metal foil covering the entire cell area (Figure 12b) senses the temperature rise (induced by the application of load and damage of the cell) sooner, sharper, and dissipates the heat faster. This result implies that using *a metal foil will facilitate quicker and even cooling stacked cells under regular operation when heat is generated due to battery charge and discharge. Hence, it is a tool to effectively sense and manage battery temperature, especially when natural cooling heating is required*. In the remaining tests, all samples used a metal (SS or Ti) foil (25 microns) between the two pouch cells stacked together.

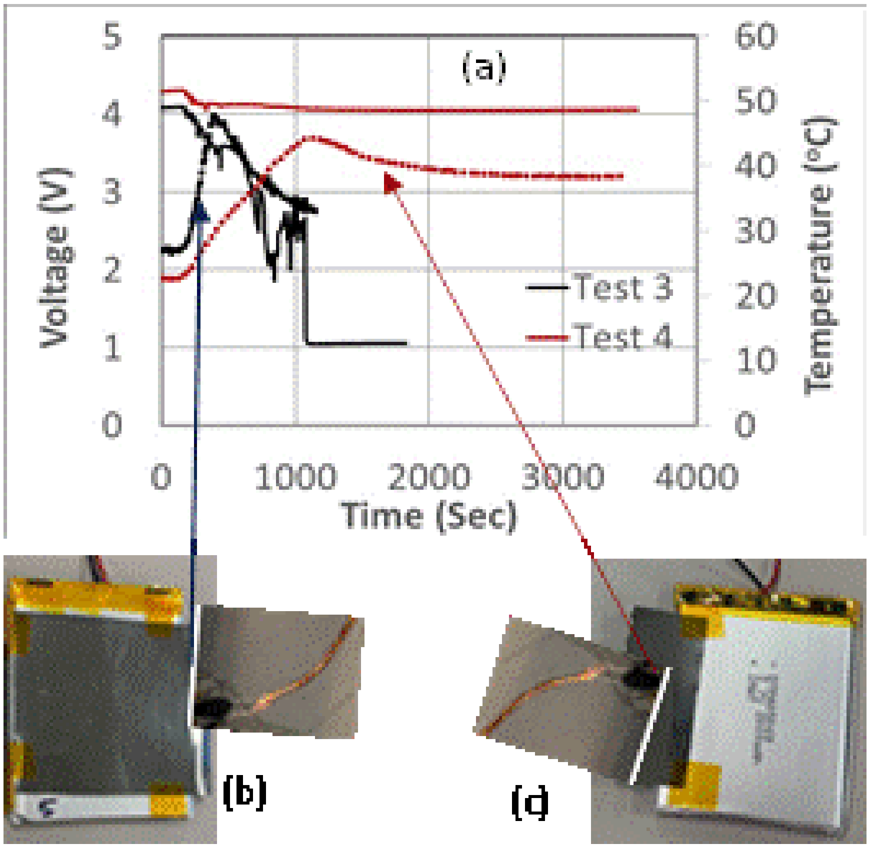

Figure 12. Measuring the battery core temperature with and without metal foil.

Figure 13 shows that a pouch cell can withstand a high load of >3k lbs without battery fire but only when the load application rate is shallow (0.01 in/min). A 5 mm radius indenter made of stainless steel was used to apply load on the cell (Appendix 1). Indenters with spherical tips with various radii are used for different applications. Still, we selected one (5 mm radius, it's neither a very sharp tip like a needle or bullet nor very big like a flat surface) for the present work and kept it constant for all the experiments involved. In the test, the indenter is static, and the cell mounted of a flat stainless steel disc moves toward the indenter until a failure (voltage drop, temperature rise) or maximum load is reached. In the test, the load is applied to the cell only once. As the rate of load application increases, the battery cell suffers more damage, leading to battery fire at a load application rate of 0.1 in/min (Figure 13). With a load application rate of 0.1 in/min, the battery caught fire within 200 sec. A sharp temperature rise was observed. The fire was quenched by nitrogen gas. In a real crash or collision, the load application rate can easily exceed 0.1 in/min; hence, secondary (mechanical) battery protection is required.

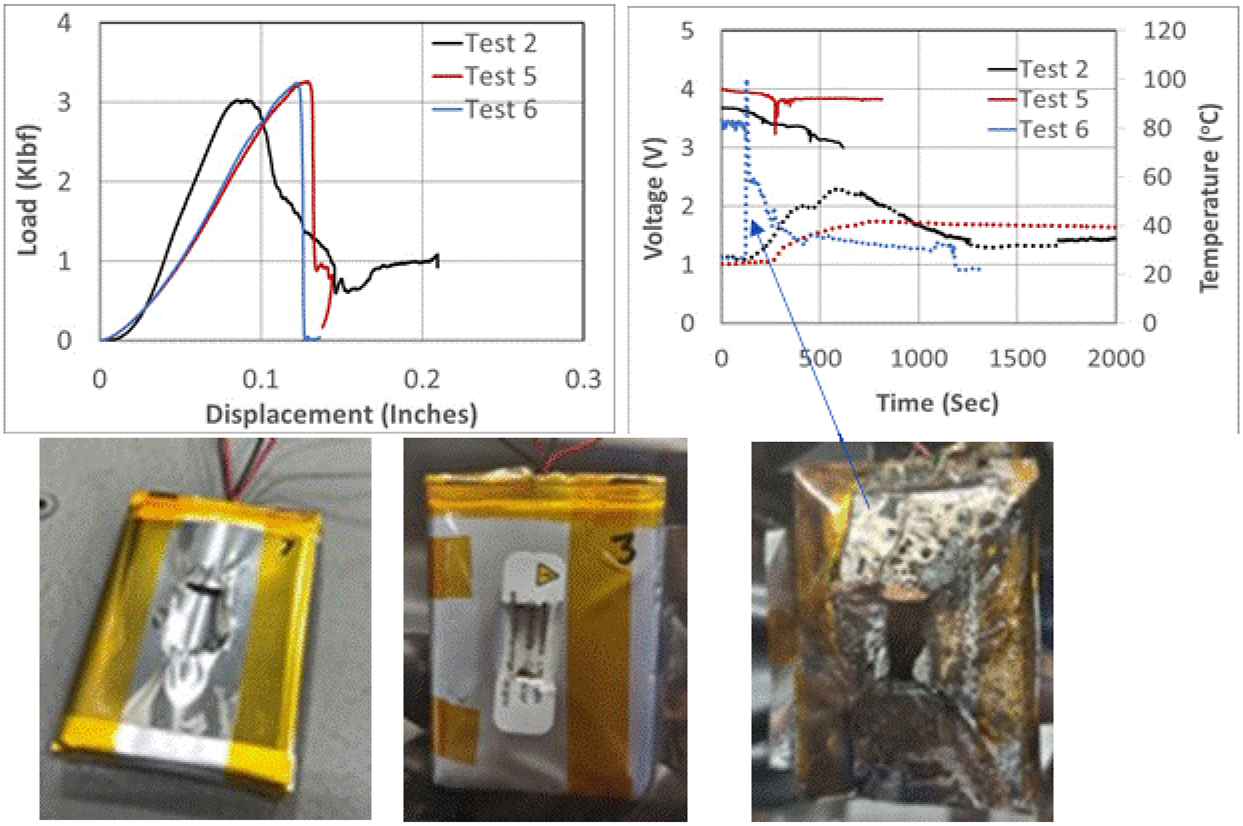

Test 2. load= 0.01 in/min Test 5. load= 0.05 in/min Test 6. load= 0.1 in/min

Figure 13. Battery failure as the rate (in/min) of load application increases.

Al has the lowest density but melts at the lowest temperature among the metals in Table 4. The next lowest-density metal is Ti (Table 4), with the highest melting point (1668°C) and sufficient temperature to survive a battery fire. Moreover, Ti has higher mechanical strengths than Al, so we conducted a weight normalization experiment to determine if Ti is better overall. Figure 14 shows that the mechanical load carried (@ 2 in/min) by pouch cells with 2 mm Ti sheet protection is 2x times better than an almost 2x times thicker (3.2 mm) Al sheet. The density of Al is 2.7 g/cm^3, whereas the density of Ti is 4.5 g/cm^3. The load-bearing capability of Ti sheet was found to be comparable to SS and sheets, but Ti (4.5 g/cm^3) has an advantage of lower weight for a given thickness when compared with the weight of SS (7.85 g/cm^3) and Ni (8.91 g/cm^3). Thus, we selected Ti for more in-depth work, primarily to determine the lowest thickness of the Ti box that will provide enough protection from mechanical indentation.

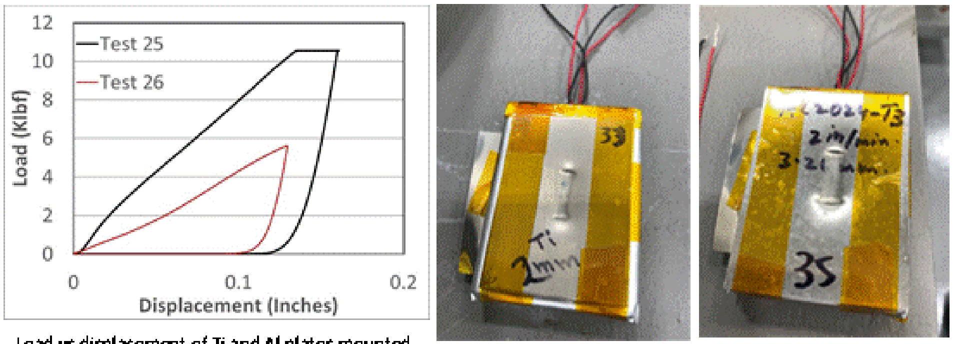

Load vs displacement of Ti and Al plates mounted on pouch cells

Test 25. Ti plate protection

Test 26. Al plate protection

Figure 14. Pouch LIB cells are protected by a 2 mm Ti sheet and a 3.4 mm Al sheet, which provides high-rate (2 in/min) load-bearing (semi-spherical indenter) capability.

Figure 15 shows that with an increase in Ti thickness (30 µm to 400 µm), the load-bearing capability of pouch cells increases from 3500 lbf to 5100 lbf. None of these cells result in TR runaway at 0.1 in/min load application rate. For comparison (Figure 13, test 6), the pouch cell caught fire without any protection when subjected to the same rate (0.1 in/min).

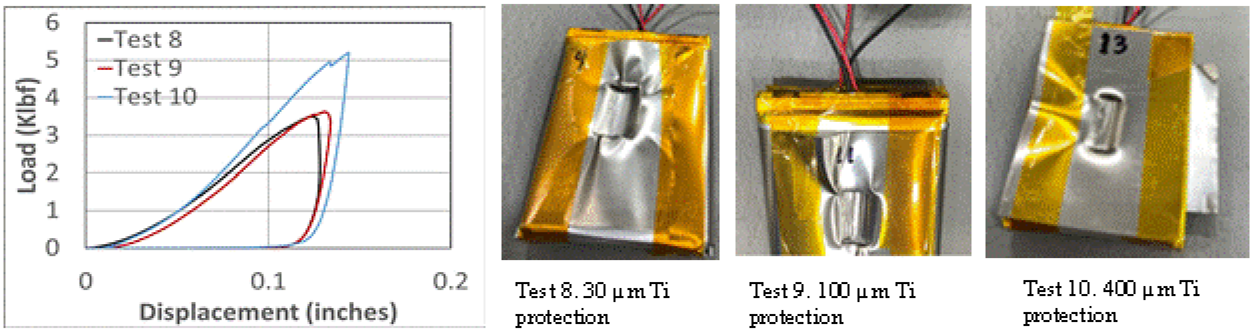

Test 8. 30 µm Ti protection

Test 9. 100 µm Ti protection

Test 10. 400 µm Ti protection

Figure 15. Load-bearing capability (semi-spherical indenter) of LIB pouch cells with 30 µm, 100, and 400 µm thick Ti foil.

Figure 16 shows the 400 µm thick Ti foil limit protecting pouch cells from increased load application rates (0.1 in/min to 0.4 in/min). Cell experienced TR when subjected to a 0.4 in/min load. Thus, we decided to test thicker Ti foils and their protection from 0.4 in/min load, and we found that the cell gets that protection from a 1,000 µm thick Ti foil, as shown in Figure 17. Cell with 1,000 µm thick Ti foil protection can sustain as twice as much load as 400 µm thick Ti foil, and cell temperature remains unaffected as their discharge voltage profile (Figure 17). However, due to cell compression, some internal damage may lead to cell swelling observed after a few hours of the test (Test 22) and cell lost voltage.

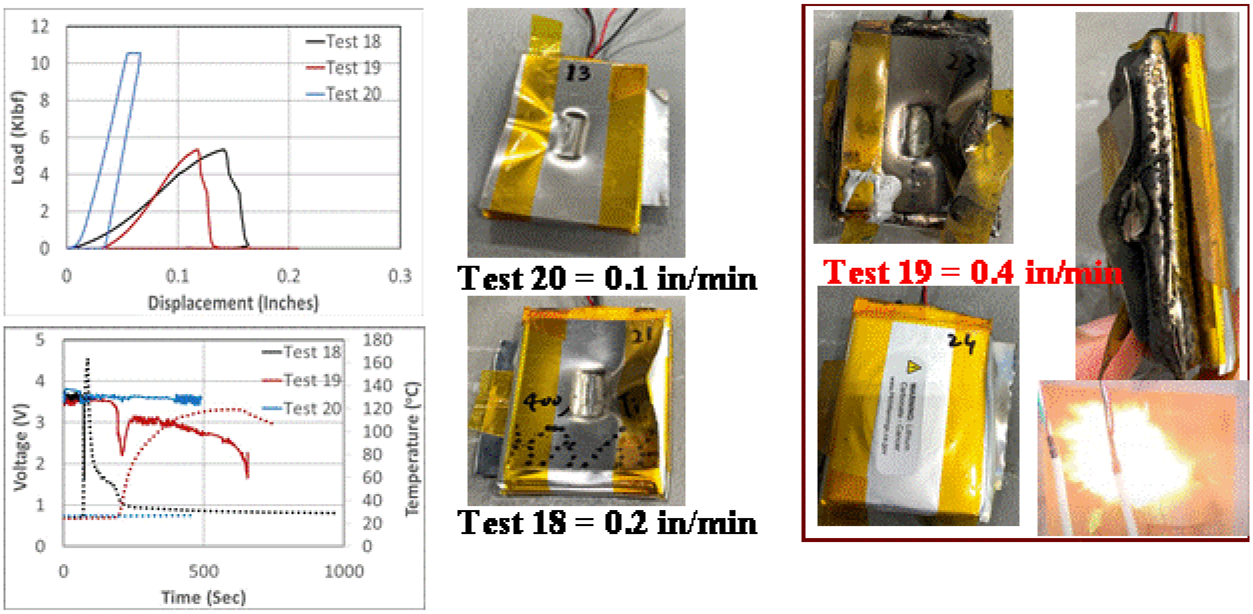

Figure 16. Failure of 400 µm thick Ti foil-protected pouch cells when subjected to a moderate load rate of 0.4 in/min using a semi-spherical indenter.

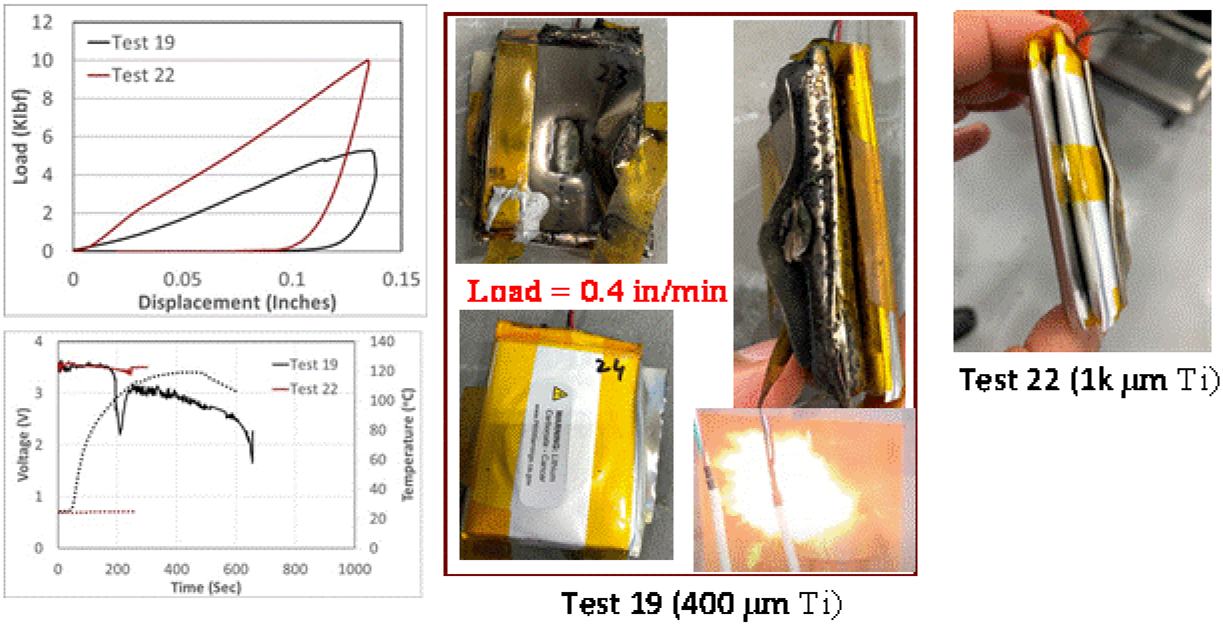

Figure 17. Resiliency of 1000 µm thick Ti foil-protected pouch cells when subjected to a moderate load rate of 0.4 in/min with semi-spherical indenter.

Even though a 1000 µm thick Ti foil protected the pouch cells from TR when subjected to a 0.4 in/min load, it ultimately failed to protect them from TR at a high rate of 1 in/min (Figure 18).

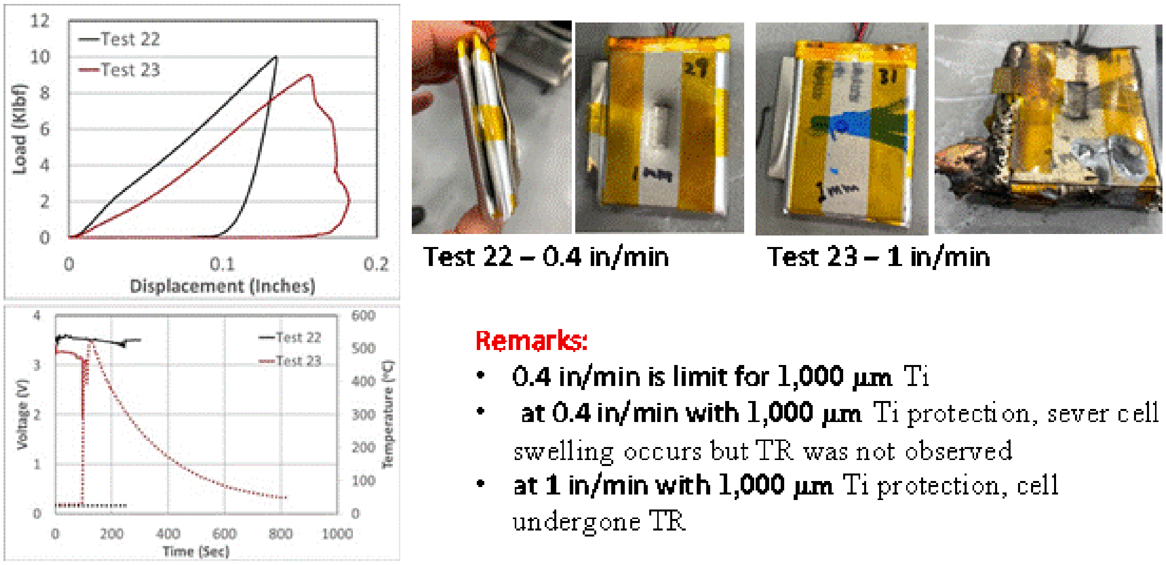

Remarks:

- 0.4 in/min is limit for 1,000 µm Ti
- at 0.4 in/min with 1,000 µm Ti protection, sever cell swelling occurs but TR was not observed
- at 1 in/min with 1,000 µm Ti protection, cell undergone TR

Figure 18. Failure of 1,000 µm thick Ti foil-protected pouch cells when subjected to a high load rate of 1 in/min with semi-spherical indenter.

Since 1,000 µm thick Ti was not enough to completely protect the pouch cell from a 1 in/min, we decided to test protection from a 2,000 µm (2 mm) thick Ti sheet, which ultimately protected not only from 1 in/min load (Figure 19) but also from a much higher 2 in/min load rate. Since 2 in/min (*indenter hit the battery in few seconds*) is quite a high rate of mechanical load application and limit of our instrument, we stopped our indentation resiliency tests using a semi-spherical intender. Still, we continued the test using flat-plate compression load (next section) to see if there is any advantage of using a metal enclosure for battery protection from compression.

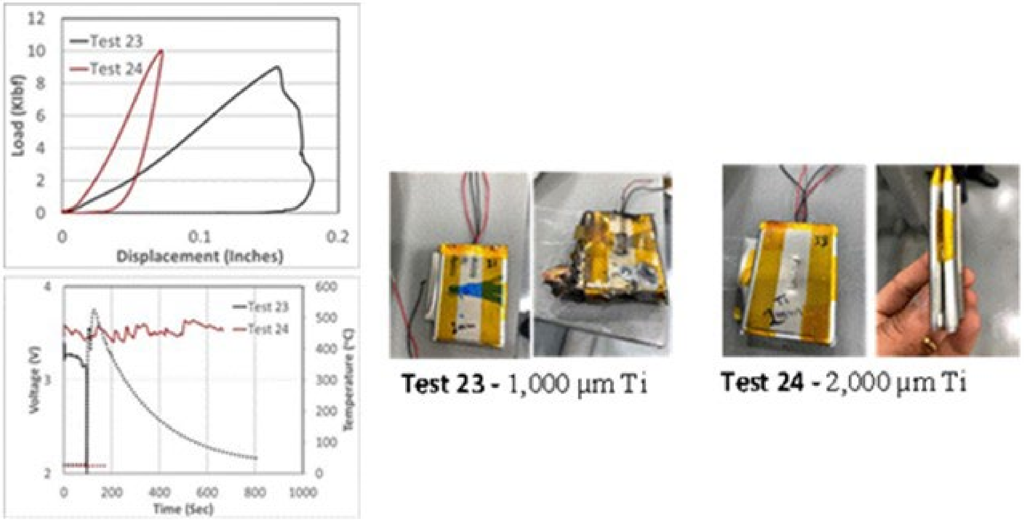

Figure 19. The resiliency of 2000 µm thick Ti foil-protected pouch cells when subjected to a high load rate of up to 2 in/min with a semi-spherical indenter.

5.2 Resiliency of pouch Li-ion cells against flat-plate compression load

Figure 20 shows the load application with 0.4 in/min on 400 µm Ti foil-protected pouch cell with semi-spherical (test 19) and flat (test 21) indenter. Details of the test setup are provided in Appendix 1. In a flat-plate compression test, also known as the crush test, cells are counted on a moving stainless steel plate, and load is applied when the moving plate pressures against a static stainless steel plate. The plate can move at different rates; in Figure 16, the plate moves at a rate of 0.4 in/min and is compared with a semi-spherical (5 mm radius) indenter moving at the same rate. A more concentrated load like the one tested above (Figure 16) with a standard semi-spherical indenter (5 mm radius) can be much more damaging than a flat-plate load (load disperses at a larger area) with the same speed shown in Figure 20. Pouch cells could withstand nearly twice as much load in the case of flat-plate load (9k lbf) compared to spherical indenters (5k lbf). Also, semi-spherical indenter induced battery TR, whereas flat indenter led only a modest temperature rise around 80°C. Suppose a sharp object hits a battery in a real-life crash, which can be related to the mechanical test done using a semispherical indenter. In contrast, a flat panel of aircraft structure can compress the battery, which can relate to the mechanical test done using flat-plate compression (crush test).

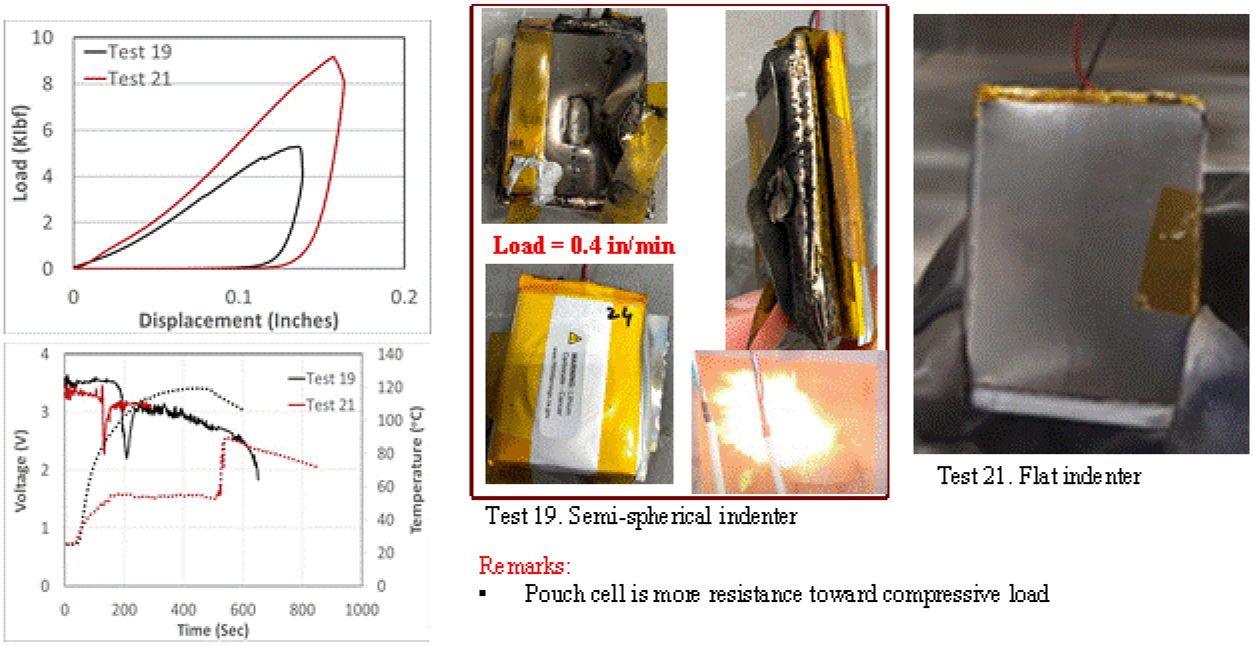

Test 19. Semi-spherical indenter

Test 21. Flat indenter

Remarks:

- Pouch cell is more resistance toward compressive load

Figure 20. Load-bearing capability of pouch cell with semi-spherical and flat indentation.

It is essential to mention here that the resiliency of the pouch cells under flat indentation (crush test) is better with Ti protection. For example, a pouch cell with 400 µm Ti foil protection takes the same load with improved load-displacement characteristics, which results in higher temperature rise as the cell was under stress for a longer time (Figure 21). This result suggests that using a rigid Ti sheet (such as 2 mm Ti as tested and presented in Figure 19) to make a battery encloser will prove quite effective against both the semi-spherical and flat indentation.

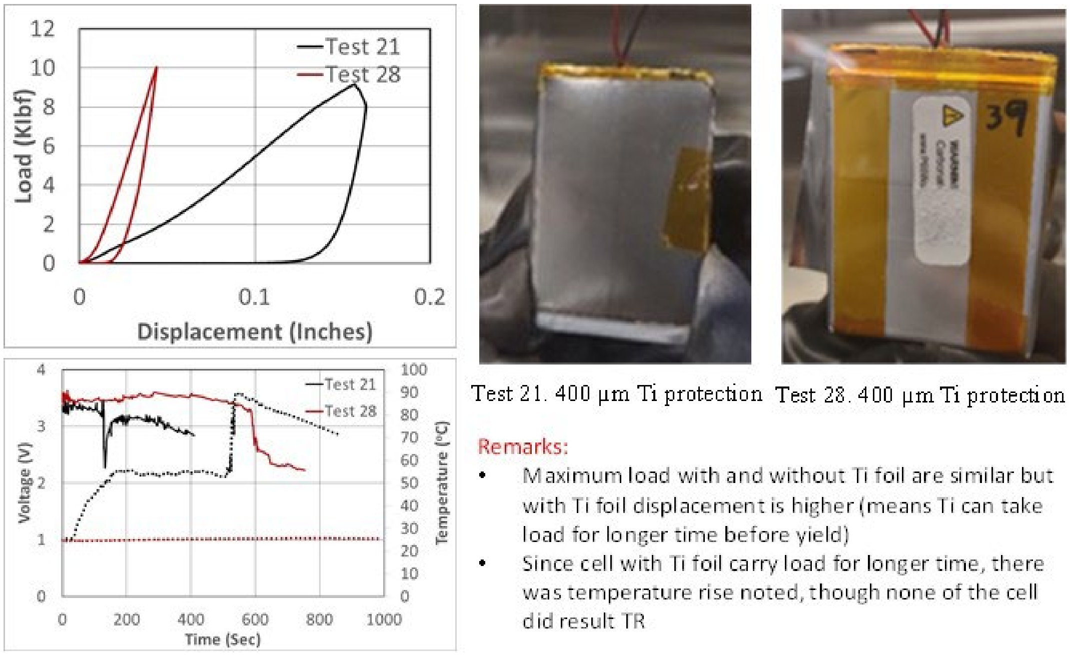

Test 21. 400 µm Ti protection Test 28. 400 µm Ti protection

Remarks:

- Maximum load with and without Ti foil are similar but with Ti foil displacement is higher (means Ti can take load for longer time before yield)
- Since cell with Ti foil carry load for longer time, there was temperature rise noted, though none of the cell did result TR

Figure 21. The metal sheet protection of pouch cells from flat indentation (crush load) is useful.

5.3 Resiliency of cylindrical Li-ion cells against semi-indentation and compression load

Beyond pouch cells, we tested the load-bearing capability of Li-ion in cylindrical format with two different Li-ion chemistries. Figure 22 shows that a cylindrical cell with NMC cathode (186650 type) is highly susceptible to semi-spherical indentation (resulting in thermal runaway) compared to LFP cathode (18650 type), which shows only a modest temperature rise above 100°C. Both NMC and LPF in 18560 formats led to similar load, but the latter had more extended displacement, suggesting that these two chemistry types may have slightly different cell casing. When comparing the same chemistry in two different formats, one 18650 and the other 26650, the cell in 26650 showed much higher load-bearing capability (LFP 18650 – 2k lbf vs. LFP 26650 – 5k lbf) and much less temperature rise (LFP 18650 – 100°C vs. LFP 26650 – 50°C) when indented with the same rate.

One reason why NMC 18650 resulted in thermal runaway and LFP 18650 and LFP 26650 did not is that the cell with NMC cathode has almost 2x higher energy density than LFP 18650. LFP cells will also fail, requiring higher load application rates. Similar results were found when we conducted a crush (flat plate compression) test on NCR (Test 32) and LFP (Test 33) cells at a load application rate of 0.4 in/min (Figure 23). Figure 23 shows that NCR (NMC cathode) involved TR with huge temperature rise and sharp voltage drop, whereas LFP did not involve TR. The temperature increased only up to 100°C, but the voltage dropped sharply, perhaps due to breakage of electrical contact. Also, the LFP cell could take 1.5x load compared to NCR (18650) and pouch cell (NMC cathode – Test 28). NMC cathode in cylindrical and pouch cell (Test 28) formats shows similar load capability when subjected to flat indentation (crush test) (Figure 23). Figures 22 and 23 show that the NMC cell has higher energy density but is more susceptible to TR when subjected to spherical indentations and flat compression.

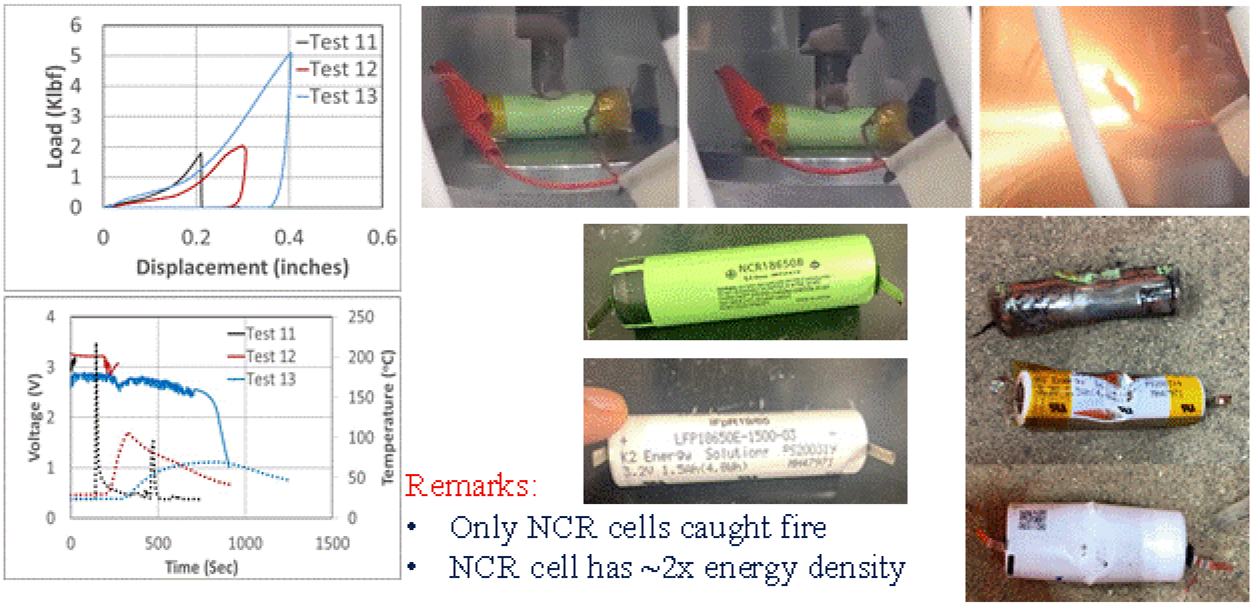

Remarks:

- Only NCR cells caught fire
- NCR cell has ~2x energy density

Figure 22. Load-bearing capability of NCR (NMC cathode in 18650 format—Test 11), LFP (18650 type), and LFP (26650 type) when a load application rate is 0.1 in/min with a semi-spherical indenter.

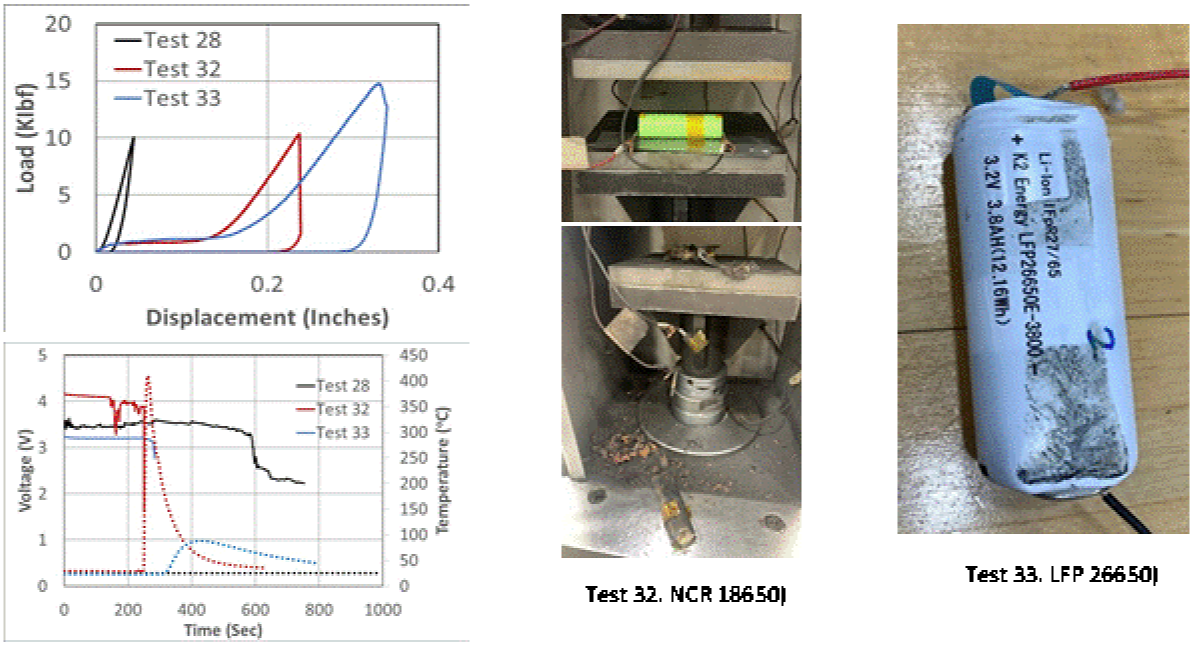

Test 32. NCR 18650|

Test 33. LFP 26650|

Figure 23. Flat load (crush) bearing capability of NCR (NMC cathode in 18650 format – Test 32), LFP (26650 type – Test 33), and NMC cathode (pouch cell – test 28), with load application rate 0.4 in/min with flat indenter.

5.4 Resiliency of pouch Li-ion cells under fatigue loads

LIB cells may be subjected to periodic fatigue loads while in service. The battery's response under fatigue loads regarding voltage change, temperature, and thermal runaway has been documented. Cells in different conditions (in-situ charge and discharge) have been subjected to periodic loads with fixed speeds. This section's results suggest that Li-ion cells without protection are highly susceptible to periodic loads and suffer permanent damage quickly, requiring a protecting enclosure for long-term safe operation. The tests can mimic a real-life situation where a loose object (sharp to flat) can repeatedly hit the battery, which will eventually fail the battery.

Figure 24 shows the entire test set-up to test the fatigue behavior of LIB pouch cells with and without 2mm thick Ti sheet protection. A 2 mm thick Ti sheet was mounted on the pouch cells. Two strain gauges, one transversal and the other parallel to the indenter, were mounted on the pouch cell and Ti sheet surface to sense fracture propagation in multi-direction. The picture on the right shows the entire test set-up, including the battery cycler (in-situ charge and discharge), mechanical load testers, camera (record battery failure), and nitrogen cylinder (battery fire extinguisher).

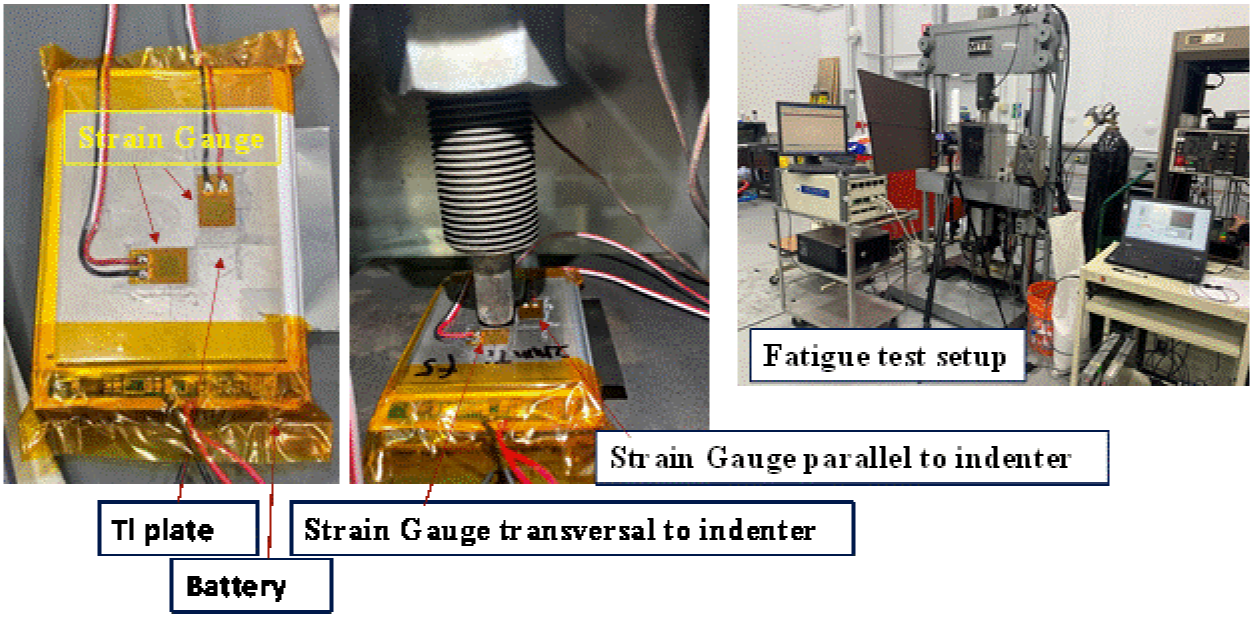

Figure 24. Test set-up to determine LIB pouch cells' fatigue resiliency.

Figure 25 shows the results from fatigue test 1. The Fatigue test 1 involves discharging (1C, 1 h discharge) the charged pouch 2Ah cells without protection but under cyclic fatigue loads. Application of cycling fatigue loads at a frequency 10 Hz with a maximum load of 3228.15 lbf (75% of maximum indentation load – Test 6 of mechanical indentation load test – Figure 13) and minimum load of 242 lbf (10% above zero loads of Test 6 of mechanical indentation load test - Figure 13) while monitoring voltage and temperature of cells. The indenter pierces through the cell within *1,000 sec* and *14,264 load cycles*, followed by a sharp temperature rise and quick cell discharge (electrical short while the indenter is inside the battery connecting all the cell components). Following the observance of the sudden voltage drop and temperature rise, the fatigue load application was stopped, resulting in the cell resuming charge before it failed. Both the gauges showed sharp displacement at the beginning (circle 1 – the start of cell package damage) and at the moment when the intender pierced through the cell (circle 2 – the complete damage of the cell), but (the strain gauge) continued functioning normally once the intender was out of the damaged cell. This result shows that a pouch cell has a *weak resiliency toward fatigue load* and needs secondary protection for long-term and safe functioning.

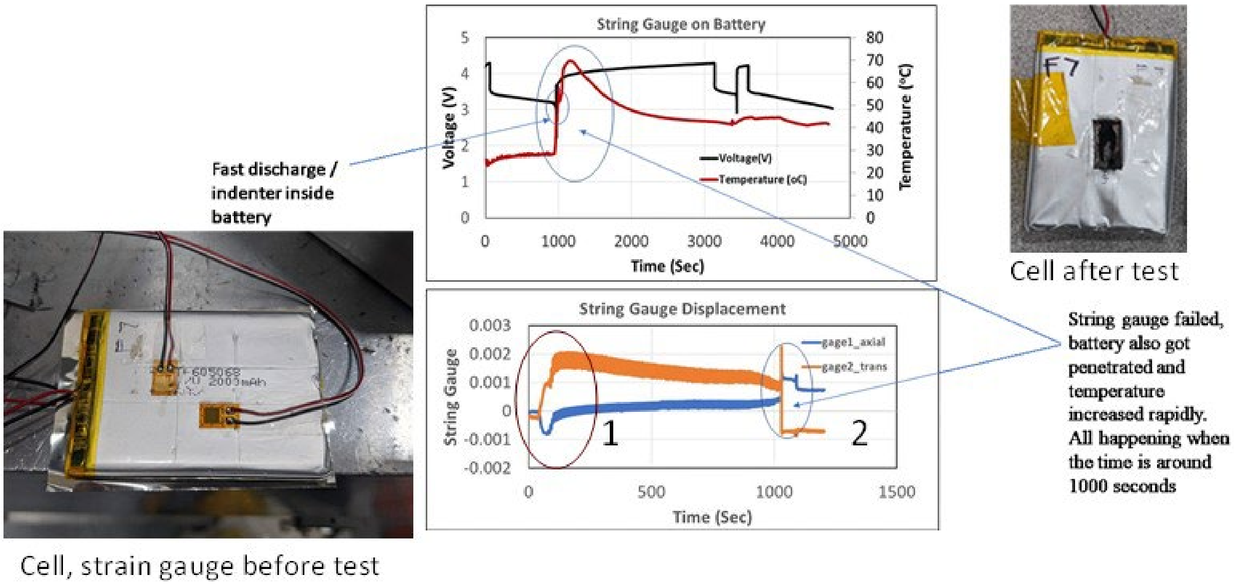

Fast discharge / indenter inside battery

String gauge failed, battery also got penetrated and temperature increased rapidly. All happening when the time is around 1000 seconds

Figure 25. The strain gauge on unprotected LIB pouch cell. Upon cell damage, the temperature rises, the voltage falls, and strain gauge displacement changes.

Fatigue test 2 (Figure 26) involves cells and test parameters similar to fatigue test 1 (Figure 25). A 2 mm Ti sheet protects the pouch cell this time. Figure 26 shows that the intender left a depression mark on the sheet after 3600 sec and 36,000 cycles. Still, the cell shows a regular voltage charge and discharge behavior and a temperature rise of around 35 °C (Figure 26 a). In Figure 26 a, some temperature data points were lost, but we observed no sharp change in cell temperature after the intender dented the Ti sheet (Figure 26 b). The intender may have dented the Ti sheet after 1000 sec of the test as the strain gauge (2) transversal to the intender failed sharply, whereas the strain gauge (1) parallel to the intender remains functional (Figure 26 c).

The failure of strain gauge 2 may have resulted in damage done to it due to a dent in the Ti sheet, which was confirmed through a postmortem study (Figure 27). Dent also ruptured the outer layer of pouch cell packaging, but the cell remains largely intact.

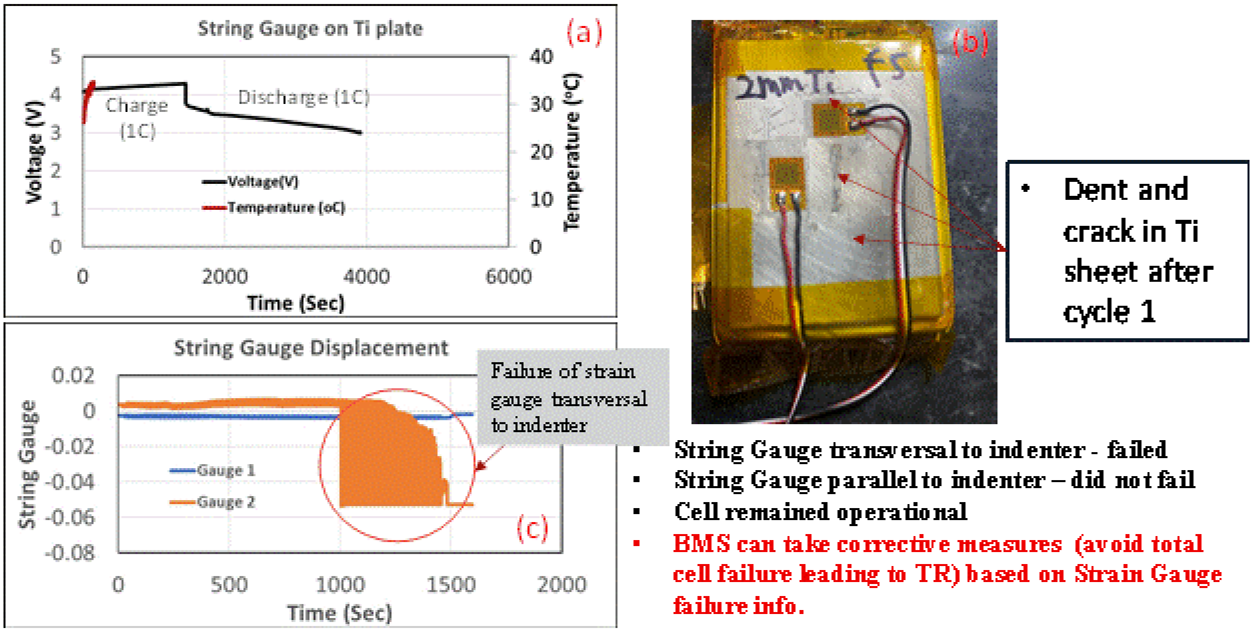

- Dent and crack in Ti sheet after cycle 1

Failure of strain gauge transversal to indenter

- **String Gauge transversal to indenter - failed**
- **String Gauge parallel to indenter – did not fail**
- **Cell remained operational**
- **BMS can take corrective measures (avoid total cell failure leading to TR) based on Strain Gauge failure info.**

Figure 26. a - Temperature increase and voltage loss; b – dent on Ti sheet; and c - change in strain gauge displacement after 1 hr (36,000 cycles of load application) test.

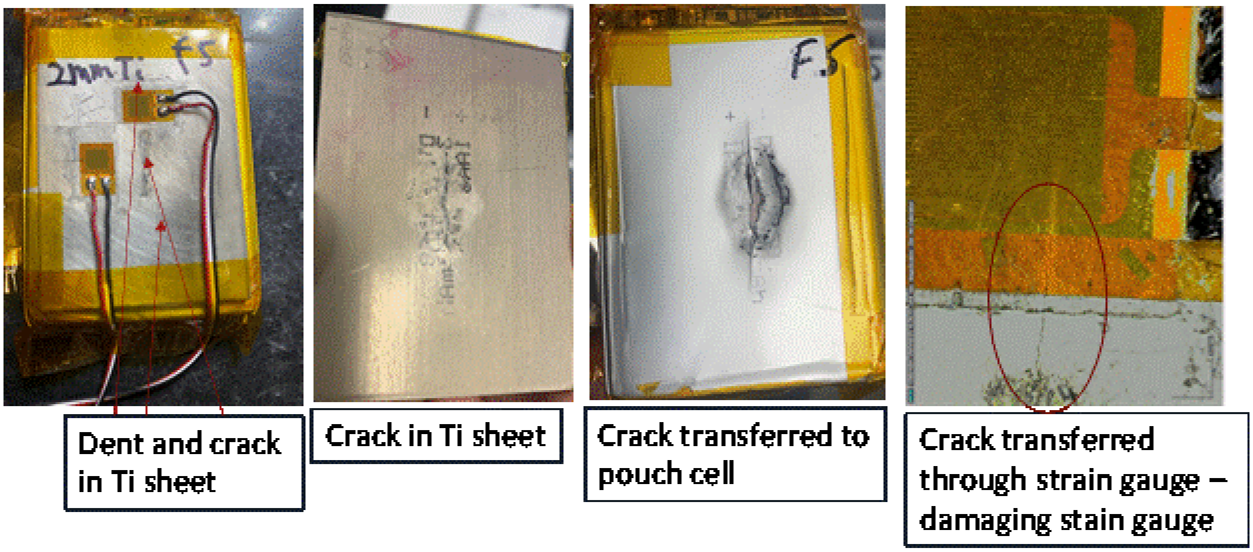

Dent and crack in Ti sheet

Crack in Ti sheet

Crack transferred to pouch cell

Crack transferred through strain gauge – damaging stain gauge

Figure 27. Initial damage to the Ti sheet under fatigue loads (1 hr, 36,000 cycles of load application) and failure transfer to pouch cell packaging and strain gauge transversal to the indenter.

Despite the initial dent in Ti sheet, we continued the fatigue test until Ti sheet was shattered into pieces. The indenter eventually pierced through the cell, leading to a sharp voltage drop and temperature rise (Figure 28). But the protection provided by Ti sheet was impressive. Using a 2 mm Ti sheet protects pouch cells from similar fatigue loads as an unprotected cell for 108,000 cycles (vs. 14,264 load cycles of an unprotected cell) and 3 hours of cell operation (vs. 0.28 hr of unprotected pouch cell) before cell failure. The extra time >2.7 hrs (compared to the time of failure for the unprotected pouch cell) provided by Ti protection from fatigue cell failure, along with a sharp change in the strain gauge displacement (Figure 26 c), can be enough information and time for BMS to shut-down the battery operation and avert catastrophic Li-ion battery failure. Furthermore, after experimentally showing the advantages of using secondary protection, especially a 2 mm Ti sheet in protection from semi-spherical, flat, and tired loads, we determined the electrochemical performances of pouch cells that survived mechanical load and analyzed the critical experimental data through Finite Element Analysis (FEA), which is presented in the next section.

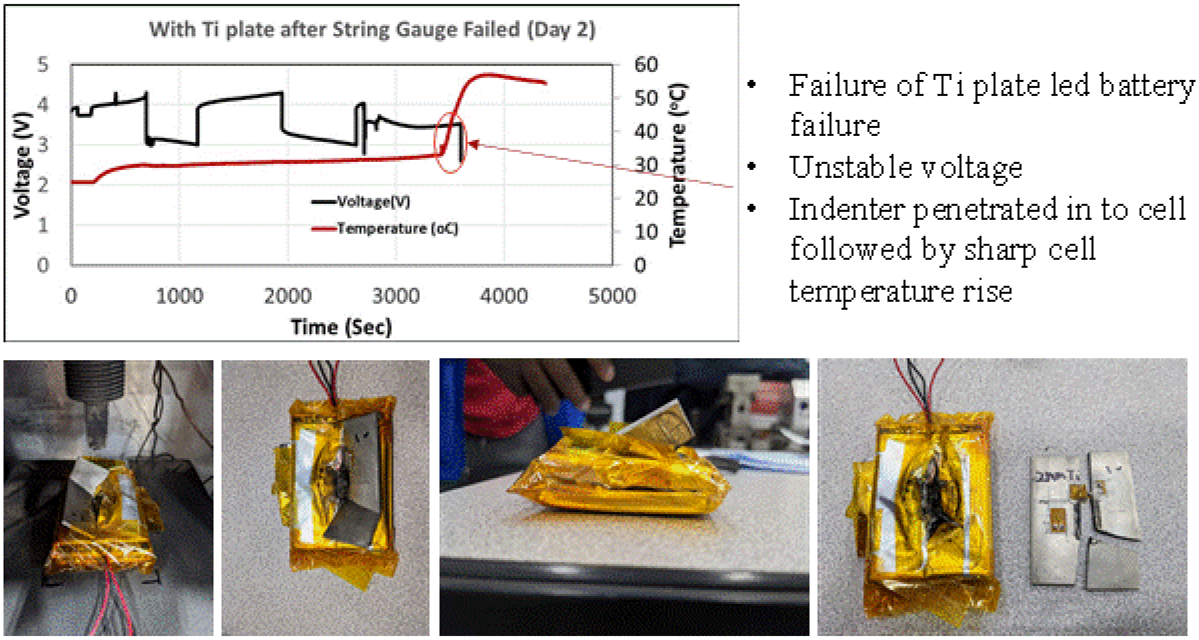

- Failure of Ti plate led battery failure
- Unstable voltage
- Indenter penetrated in to cell followed by sharp cell temperature rise

Figure 28. Fatigue test of 2 mm Ti sheet protected pouch cells until complete failure.

6 Electrochemical analysis of cells survived during mechanical tests

Batteries will play a vital role in the electrification of aerospace. Modern batteries can provide high-energy, high-power, long-cycle life and suitability needed for near future small-size aircraft, but safety is still a concern, especially in dangerous situations like aircraft crashes because if damaged, the battery can release stored energy fast, leading to a battery fire. The worst cases could cause the batteries to burn or explode and can lead to severe injury or death to anyone in the vicinity of this disaster. Thus, the batteries must be protected from various adverse environmental effects, especially mechanical damage (puncture), which leads to quick discharge (electrical shorting) and accelerates exothermic (heat-releasing) reactions. Ideally, battery packs can be protected from any mechanical damage using a thick battery enclosure. However, a battery enclosure that can be very thick and heavy would reduce the battery energy density significantly, which is practically not acceptable. The question then is how much protection the batteries need and how they should be protected without adding too much extra weight, negating the advantage of high energy in today's and future aerospace battery systems.

This project is designed to answer some of the above questions. Various materials (metal, plastic, and carbon composites) have been tested to determine their protective behaviors (hence their suitability as battery enclosures) from mechanical damage. In this report section, we document the electrochemical behavior of those cells that survived mechanical abuse tests when protected by metal sheets. Understanding the post-mechanical test behavior of battery cells is essential because it confirms their survival and answers whether those battery cells are good enough for post-test use with desired safety. The following sections, 6.1, 6.2, and 6.3, document the electrochemical behavior of LIB cells (2 Ah) after ten months of mechanical tests. *As seen in the following paragraphs, there are minor variations in the electrochemical cycling (100 cycles each at 0.5C and 1C rates) behavior of the survived cells. Still, no unusual temperature increase (all cells cycled up to 1C rate remains around room temperature) was found during the cycling of any cells, indicating the possibility of post-crash use of survived cells without safety issues.*

6.1 Post-mechanical test cell capacity after 10 months of storage

Dozens of mechanical tests were carried out, but only a few of the cells, as identified in Table 5, survived due to adequate protection from mechanical abuse (indentation) tests conducted on different thickness protective sheets and with variable rates of mechanical indentation. Each test was carried out with two pouch cells stacked together (*in the future, such tests on modules are recommended*) to determine how damage can propagate from a directly impacted cell (identified position – top) to a nearby cell (identified position – bottom) (Figure 29). For example, the top cell with an indentation rate of 0.1 in/min did not survive due to inadequate protection (thinner Ti sheets (200 µm). However, bottom cells (#18) related to this test survived, indicating that thinner protection sheets may not protect directly impacted cells, but the rest of the cells in the pack would survive. *The increased survivability of cells beneath the indented cells due to* *metallic sheets (or any other mechanically robust sheets) is significant as this can reduce thermal runaway propagation and the severity of thermal runaway.* Kalnaus et al. (2019) found that high-speed indentation triggers long-range deformation propagation through the whole cell stack in the Li-ion module. Hence, as the present work shows, a mechanically robust battery enclosure must be developed to avoid catastrophic thermal runaway events and minimize damage to all cells. The postmortem pictures of the top (#17) and bottom (#18) cells protected with 200 µm Ti are shown in Figure 30.

Furthermore, 400 µm and 1,000 µm Ti sheets were good enough to protect the top and bottom cells from a moderate rate of 0.4 in/min. However, 1,000 µm Ti could not protect the cell from going to thermal runaway with a higher rate of 1.0 in/min. A 2,000 µm Ti sheet was good enough to protect from mechanical damage of even top cells from a 1 and 2 in/min indentation. Compared to Ti (2,000 µm), Al required thicker (3,260 µm) sheets for similar protection of top cells. Al, with a thickness of 1,650 µm, was not good enough to protect the top cell from even 1 in/min indentation, but the bottom cell survived. *Data presented in this section suggests that the thickness or protective material will depend on the mechanical indentation rates. Thicker sheets will be needed to protect them from higher mechanical indentation. Protective behavior also varies with the material selected. For example, titanium proves better than aluminum for protection from a given indentation rate.*

Table 5. Details on LIB cells that survived under mechanical loads.

Cell Number	Position	Protection Material	Thickness (µm)	Indentation rate (in/min)	Capacity (Ah) before test	Capacity (Ah) after ten (10) months	% capacity remaining after ten (10) months
18	Bottom	Ti	200	0.1	1.99752877	0.71513298	36
27	Top	Ti	400*	0.4	1.996788902	0.436139749	22
30	Bottom	Ti	1,000#	0.4	1.938231844	0.353645119	18
33	Top	Ti	2,000	1	1.898767574	0.368222475	18
34	Bottom	Ti	2,000	1	1.937697577	0.361142642	18
35	Top	Al	3,260	2	1.996939923	0.348391302	17
36	Bottom	Al	3,260	2	1.99709406	0.286210262	14
37	Top	Al	1,650	1	1.998214515	0.861326631	43
38	Bottom	Al	1,650	1	1.997062914	0.883900279	44

*The bottom cell also survived, but the post-test data is not available for that cell.

The top cell also survived, but the post-test data is unavailable.

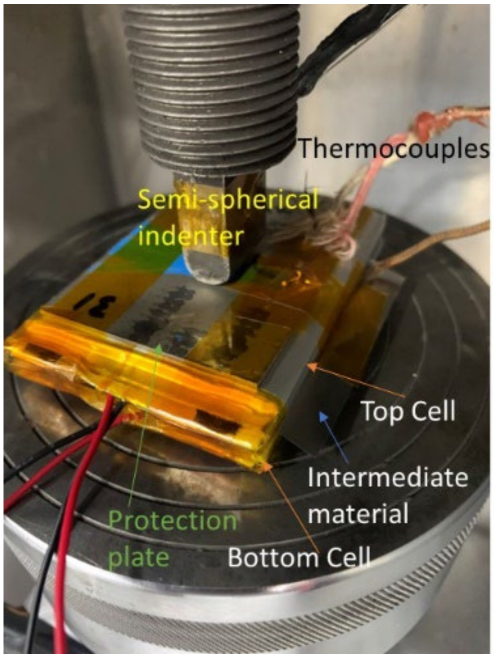

Figure 29. Details of mechanical indentation test assembly for 2x2Ah stacked LIB cells.

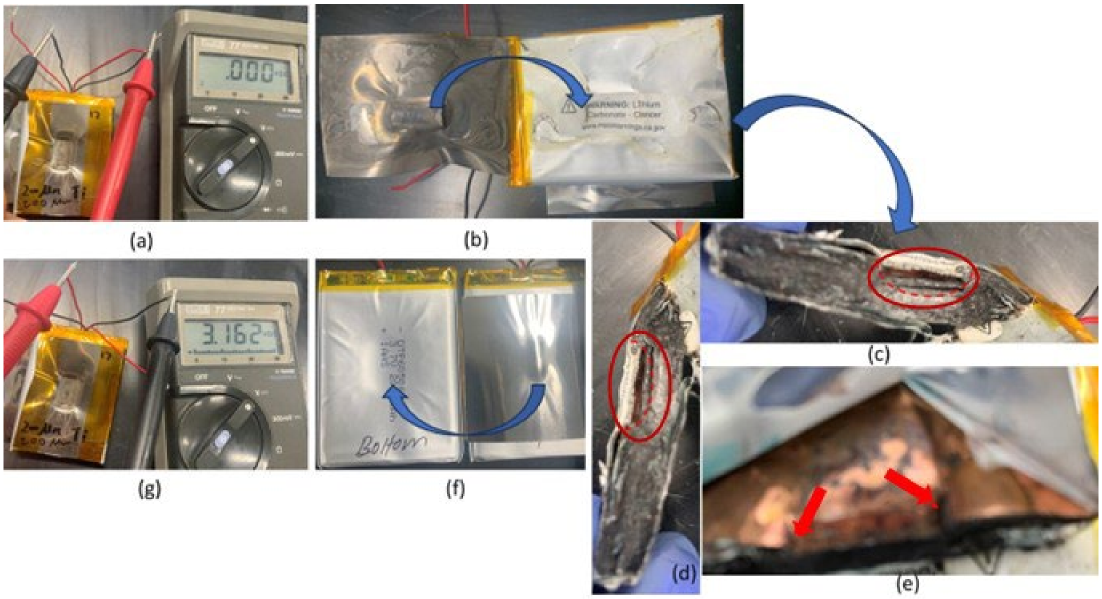

Figure 30. Postmortem pictures of LIB pouch cells protected with 200 μm Ti and subjected to mechanical indentation at a rate of 0.1 in/min. a) cavity formed on top cell similar to the size of indenter (5 mm, radius) and loss of cell voltage; b) broken Ti sheet due to indentation that led to minor fracture of pouch cell skin allowing liquid leakage and cell drying; c & d) cross-section of pouch cell showing indentation and depression (red – curves) on pouch cell layers; e) fracture of copper current collector and consequent damage to cells' other layers; f) load transfer to bottom cell, apparent compression but no physical cut on the bottom cell keeping the bottom cell functional (voltage 3.16 V after discharge; g).

After the mechanical tests, we stored the surviving cells (18, 27, 30, 33-38) for ten (10) months to determine the self-discharge rates and subsequent cycling performance. Table 6 and Figure 31 shows that the survived cells lost variable capacities during ten months of storage, indicating different mechanical compressions during the indentation tests. A typical cell having the same chemistry (NMC cathode, graphite anode, and liquid electrolyte) and capacity (~2Ah) as used in this test stored for ten (10) months at room temperature may retain around 80% of the original capacity (Keil, et al., 2016). However, cells after mechanical tests could maintain a minimum of 17% and a maximum of 44% of the original capacities. Lower capacity retention in mechanically indented cells indicates that during the mechanical indentation test, the cell may have been forced discharged due to compression of cell components (Cannarella & Arnold, 2014), as evident in a representative post-test picture in Figure 30 and Figure 32. Depression on the cells (#30) is due to mechanical damage of the top cell (#31 – cell did not survive the test) with a moving (0.4 in/min) semi-spherical (5 mm) indenter. A critical deformation depth can cause a battery cell to reach its mechanical failure criteria where the principal strains in the components exceed their failure limit. Notably, despite higher self-discharge in mechanically indented cells protected by metallic plates, the follow-on discharge capacities were very close to the original capacities, as evident from Figure 31 b. Sections 6.2 and 6.3 provide detailed cycling performances of all the cells identified in Table 6.

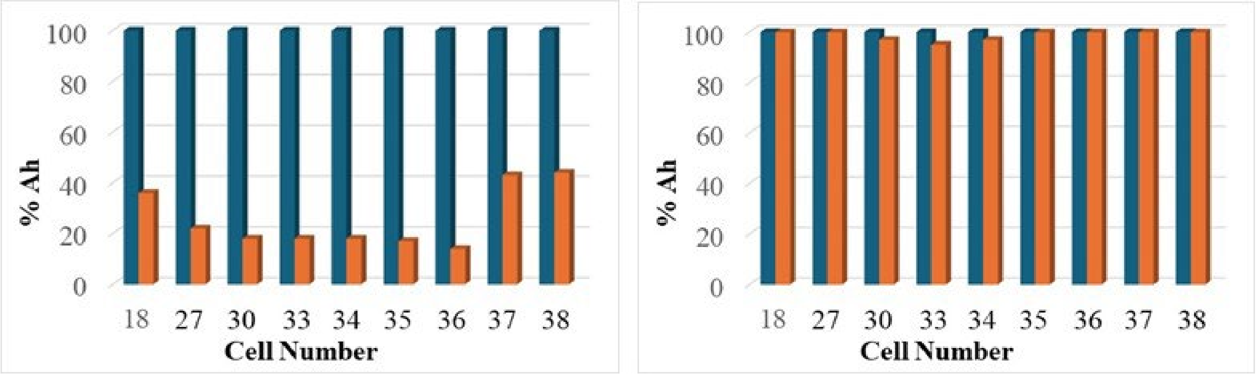

(a) (b)

Figure 31. Experimental capacities of 2Ah LIB pouch cells a) before (blue bar) and after (orange bar) 10 months storage of mechanical test, and b) before (blue bar) and 2nd discharge (orange bar) after mechanical test.

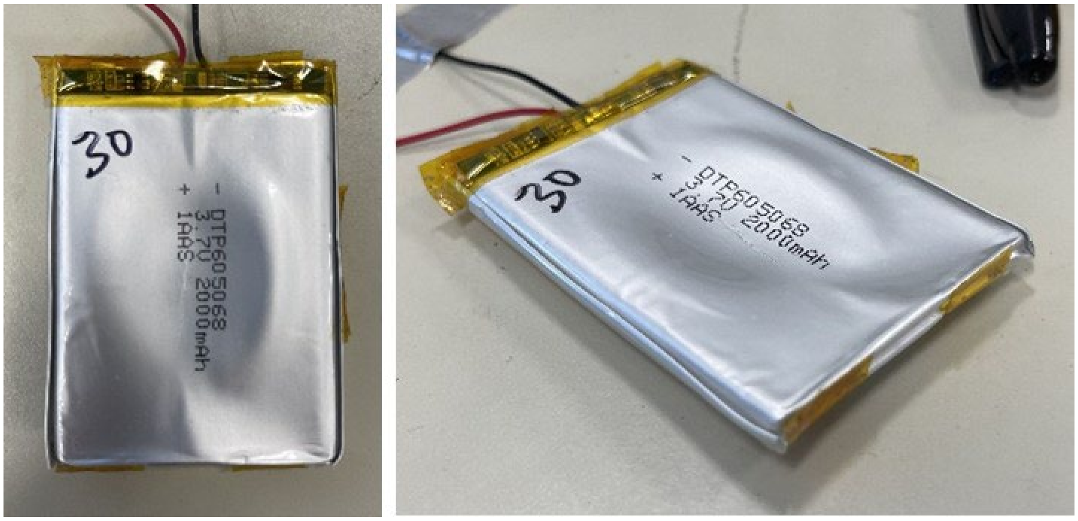

Figure 32: Depression in the bottom cell (#30) due to indentation of the top cell, which has a 1mm Ti sheet and is subjected to a 0.4 in/min indentation rate.

6.2 Room-temperature cycling at C/2 (0.5C) rate

After the mechanical tests were completed and the cells sat in a safe, enclosed lab environment for ten months, they underwent charge and discharge cycle testing. The 100 cycles were conducted at 0.5 C rate to see how the cells performed when discharged with a medium charge and discharge current. Figure 33 shows each cell pair's charge and discharge voltages compared to its capacity for the cells' second cycle. All the cells were charging and discharging as a healthy battery cell would. If both the cells of a pair remain functional, the red curve represents the top cell (directly impacted cell), and the black curve shows the bottom cell. The graphs show a trend that the cells on top typically charge and discharge slightly less than the bottom cells, which is justifiable as the top cell was directly in contact with the metal plate upon which mechanical indentation was applied. Also, the comparison of 2nd discharge for all bottom cells (figure 34 a) and top cells (figure 34 b) do not differ by a large margin.

Finally, at a 0.5C rate, the discharge behavior of 2 mm Ti and 3.264 mm Al protected cells subjected to the highest indentation rates (2.0 in/min) is compared (Figure 35). Both figures 34a and 34b show that the surviving top and bottom cells, when protected with 3.26 mm Al, are slightly better than 2.0 mm Ti-protected cells. However, an important observation is that the top cell loses around 13% of capacity (baseline 2Ah compared to 1.72 Ah after 100 cycles), whereas bottom cells lost around 5% (2 Ah to 1.89Ah) for the same comparison. *This highlights that the directly impacted cells may induce different degrees of permanent damage and may or may not be used. In contrast, the remaining cells may be unaffected during mechanical indentation and continue functioning as normal cells. To extend this conclusion, similar tests on a module should be conducted.*

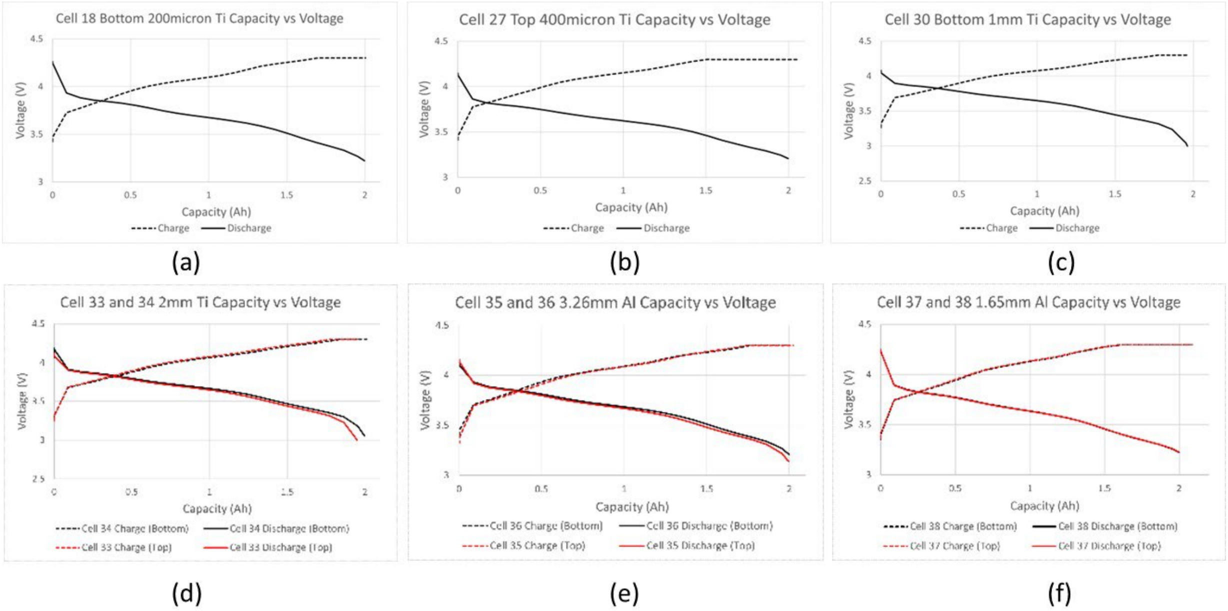

Figure 33: Voltage vs capacity curves of all the survived cells when charged and discharged at a 0.5 C rate.

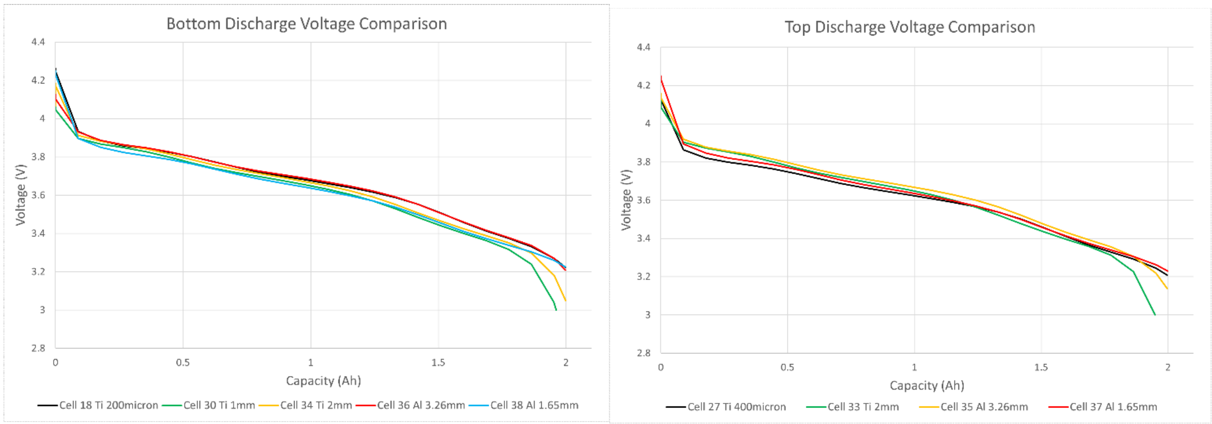

(a) (b)

Figure 34. Discharge (0.5C rate) curves of all bottom cells (a) and top cells (b).

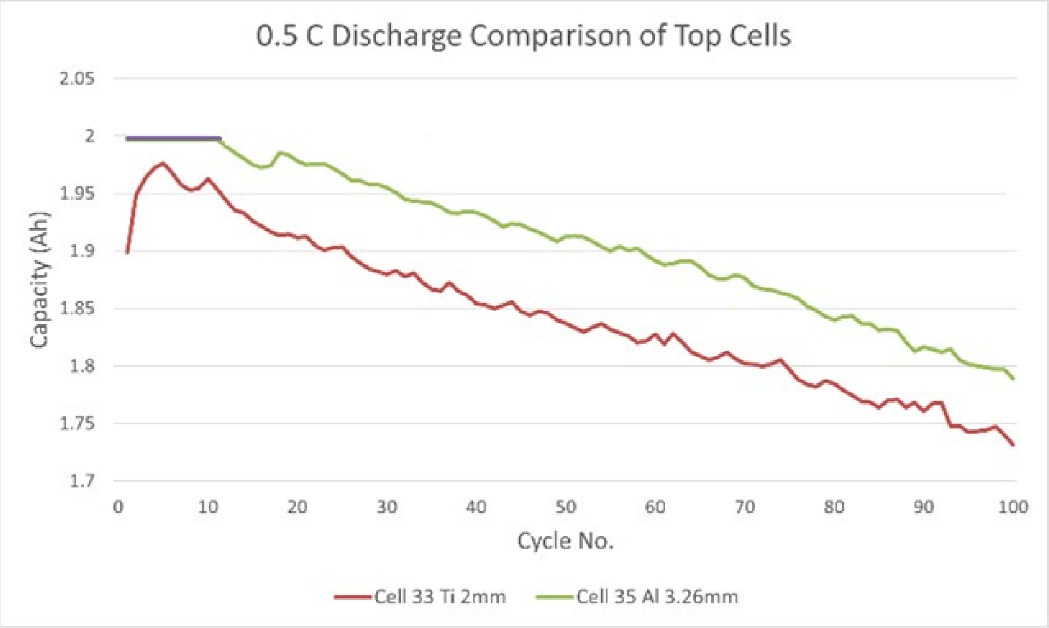

(a)

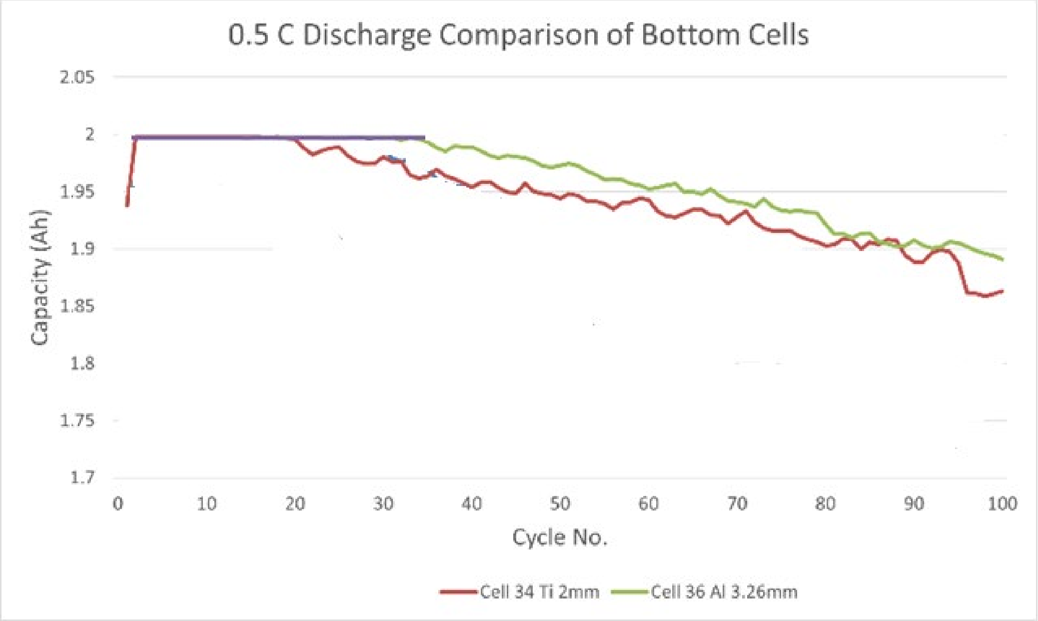

(b)

Figure 35. Cycling (C/2 rate) performances of all bottom cells (a) and top cells (b).

6.3 Room-temperature cycling at 1C rate

This section concludes that the conclusions stated in the prior section (6.2) remain similar when cells cycle at a 1C rate. All the survived cells show a typical discharge capacity as healthy cells; the higher the C-rate, the lower the discharge capacity. Figure 36 (a—i) compares the discharge capacities of each survived cell at two different C-rates, viz 0.5C and 1C rates. Data is in Figure 36; though there are slight variations in discharge capacities at the 1C rate, it can be confidently concluded that all the survived cells are still working as intended. Moreover, the prior comparison between 2 mm Ti and 3.26 mm Al-protected cells holds. There is only a slight difference between the discharge capacities of cells protected by 2 mm and 3.26 mm Al. Still, the significant difference is that the top cells in direct contact with the indented plates perform inferior to the bottom cells. For example, during 100 cycles, the top cells lose 41% capacity (from 1.7 Ah to 1.0 Ah; Figure 37(a)), whereas the bottom cells lose, on average, 11% (from 1.8 Ah to 1.6 Ah; Figure 37(b)).

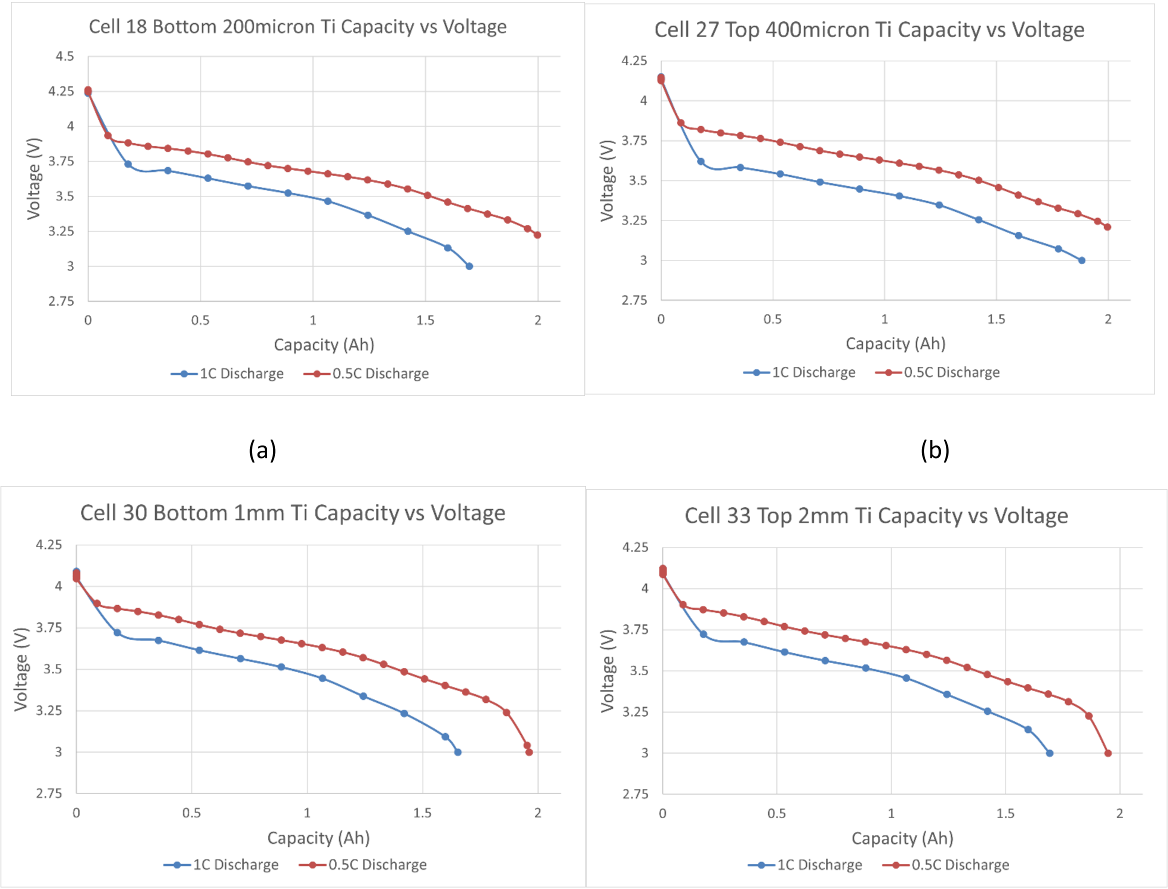

(a) (b)

(c) (d)

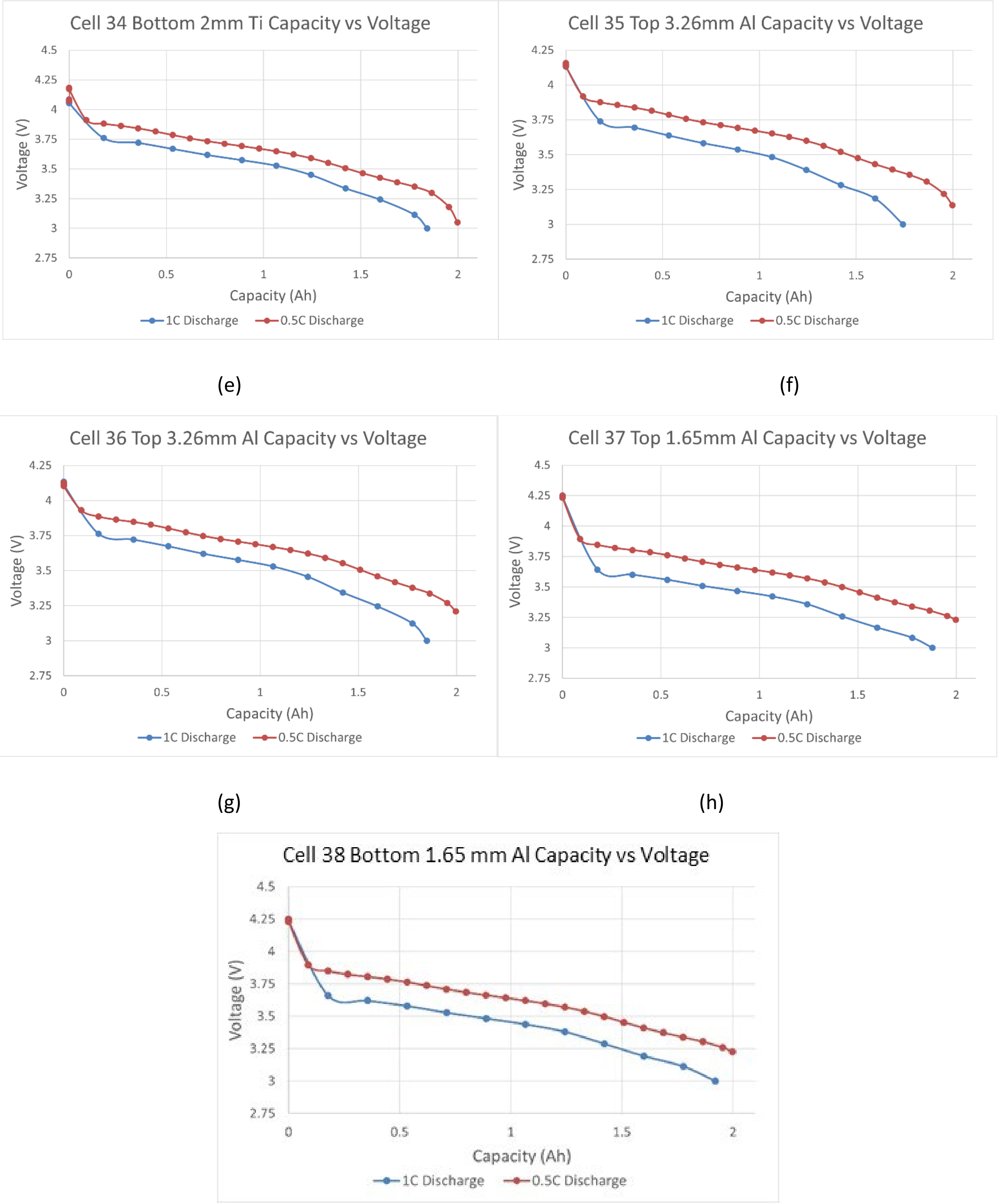

(e)

(f)

(g)

(h)

(i)

Figure 36: Comparison of discharge capacities of all the survived cells discharged at 0.5 C and 1C rates.

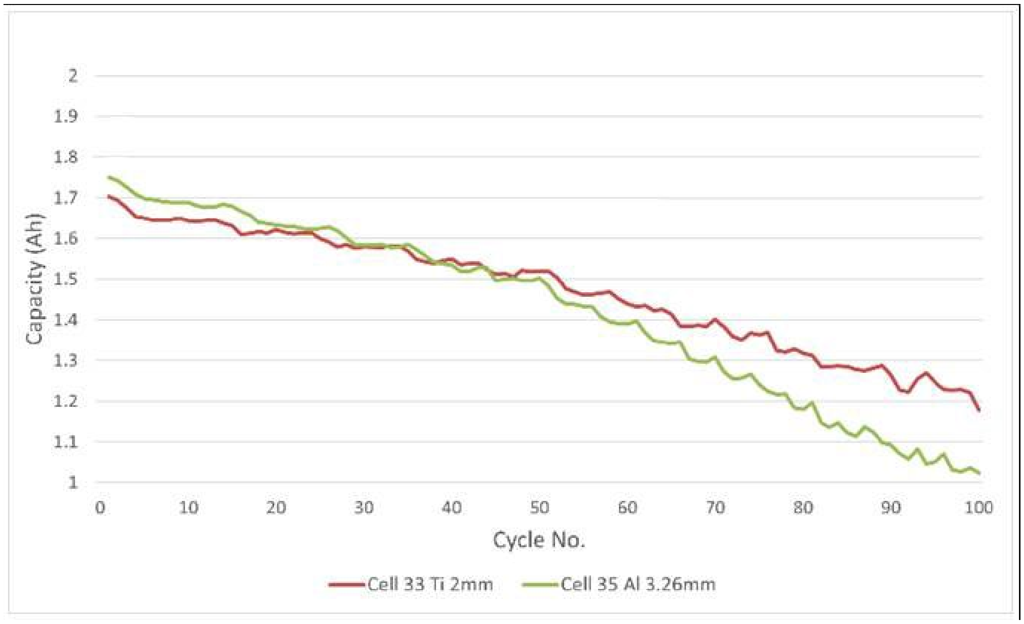

a (top cells)

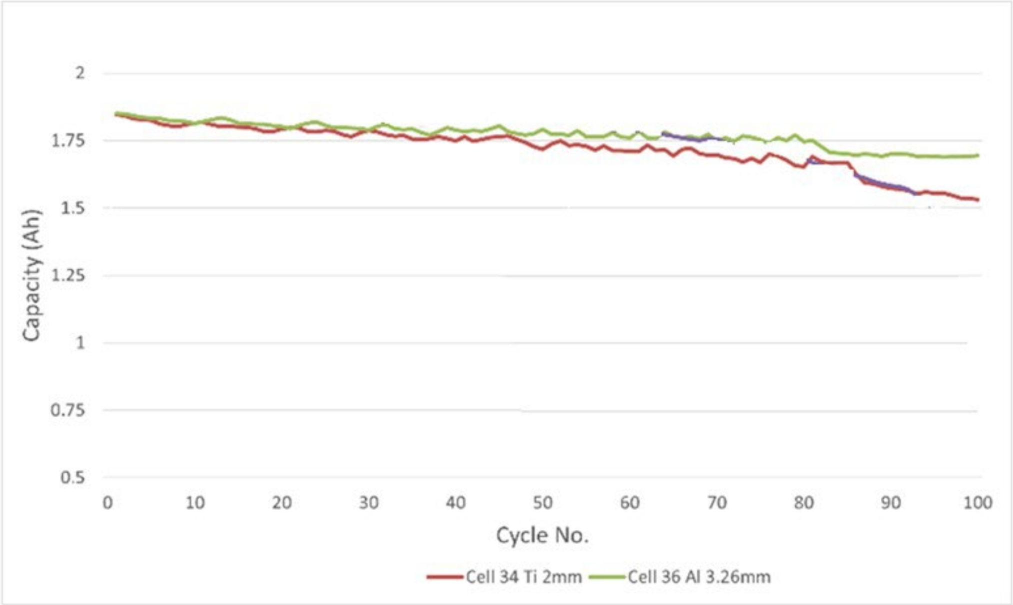

b (bottom cells)

Figure 37: Comparison of discharge capacities of 2 mm Ti and 3.26 mm Al protected cells when indented at 2 in/min and discharged at 1C rate after 10 months of storage.

7 Mechanical analysis

The experimental data generated in this project suggests that the required thickness of the protective metal sheet will depend on the rate of mechanical indentation. Figure 38 summarizes the thickness of Ti metal sheets needed to protect from a given indentation (approximately *0.625 in long x 0.5 in wide indenter with a rounded (5 mm radius) nose*) moving at a particular rate (in/min) and hitting the protected battery cells. During our tests, the highest indentation rate our machine could produce was 2 in/min. We concluded that a 2 mm Ti sheet would be required to protect a battery if, during a crash, a moving object (metal) would hit the pouch cell battery with 2 in/min. If the moving objects travel faster than 2 in/min and hit the protected battery cells, the thickness of the protective metal sheet is expected to be higher. Also, if the radius of the indenter changes (lower or higher than 5 mm used here in this project), the required thickness of the metal (protective) sheet is expected to change. The smaller the indenter radius, the thicker the protective sheet is needed. Thomas et al. found that the force-displacement curves obtained for hemispherical indenters and pouch cell scale linearly with the indenter tip radius (Tancogne-Dejean & Mohr, 2022).

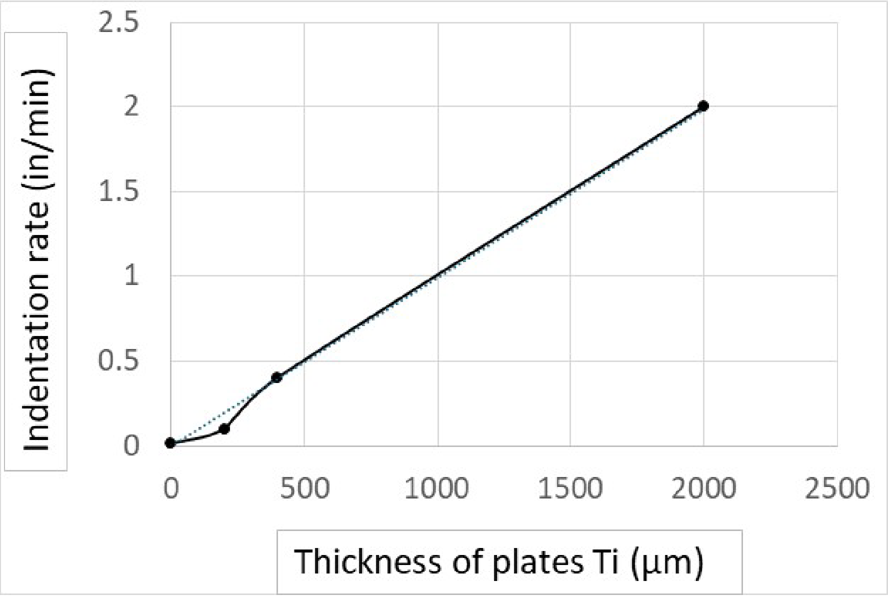

Figure 38. The thickness of titanium is required to protect from increased mechanical indentation rates.

This section (#7) provides the outcome of the analytical modeling of the mechanical behavior (under moving indentation and compression loads) of the baseline and 2 mm Ti sheet-protected LIB pouch cells and 18650 cylindrical cells. We must focus on a protective metal plate and optimize its thickness to eliminate TR in a collision condition. The experimental tests on the most promising LIB configurations were modeled using Abaqus FEA software. Accurately duplicating mechanical tests in FEA analyses could provide helpful information, when considered in conjunction with temperature and voltage data (presented in later section 8), in predicting when thermal runaway will occur. For the analytical study presented in this section, we treated pouch cells as a whole as the basic structure (a solid box). We did not investigate layers of pouch cells, as lots of layer-level modeling has been published (Cannarella & Arnold, 2014). The literature (experiment and modeling) on the indentation of small-format lithium-ion pouch cells by Thomas et al. (Cannarella & Arnold, 2014) sets up a baseline study for this project. Their study was on small-format (4 Ah, lithium cobalt oxide cathode, LCO) pouch cells, similar to our project work (2 Ah, LCO cathode). The difference between our project work and prior published work (Tancogne-Dejean & Mohr, 2022) is that we focused on finding materials that protect from mechanical indentation (5 mm radius) and flat-plate compression loads. In contrast, Thomas et al. work was to understand the mechanical behavior of pouch cells without protection. *We found (**sections 7.1 – 7.5**) a good correlation between experimental and analytical curves, and the difference can be used to understand the role of cell casing (especially in cylindrical cells) and excess packing of cell components under mechanical loads.*

7.1 Indentation of two stacked pouch cells without a protective metal plate

The ideal configuration of one 2 Ah pouch cell LIB stacked on top of another identical 2 Ah pouch cell LIB with one 25.4 µm (0.001 in) thick layer of stainless steel between the cells was modeled as displayed in Figure 39. Stainless steel foil was used between two pouch cells to attach a thermocouple to measure the battery's core temperature. One-quarter of the test was modeled to take advantage of symmetry about the X-Z and Y-Z planes. The indenter was modeled as a rigid body. The LIB pouch cells were 2.756 in long x 1.988 in wide x 0.244 in thick blocks. The stainless steel foil was modeled utilizing the same length and width as the pouch cells, which were 0.001 inches thick.

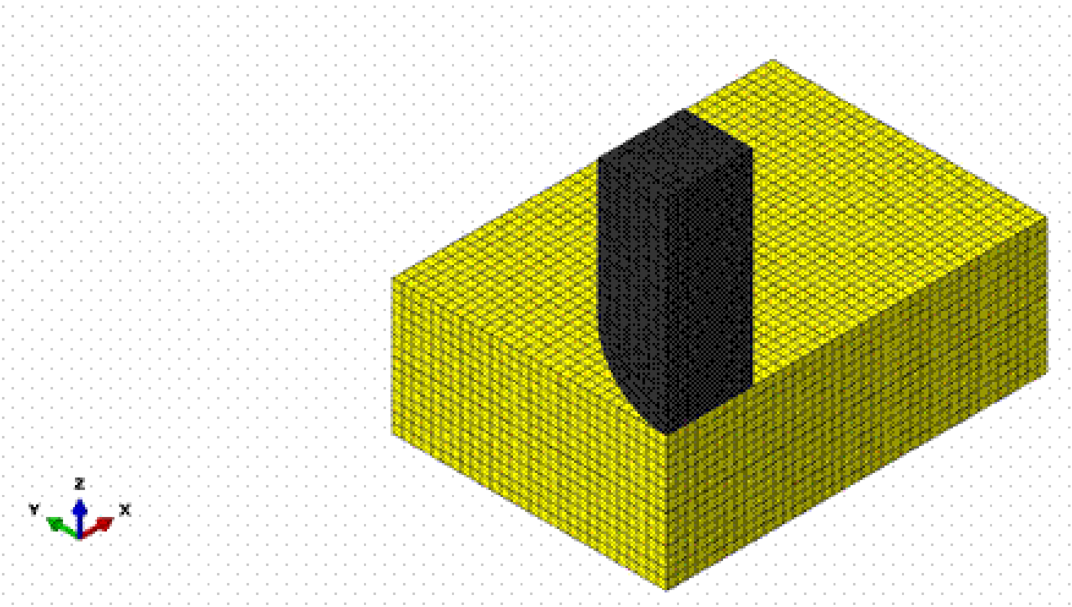

Figure 39. FEA Model of indentation test on configuration (2 pouch cells stacked together) with no top-protecting metal sheet.

Elastic-plastic stainless steel properties were assigned to the foil between the two LIB pouch cells, as listed in Table 6. Analysis iterations were conducted to determine the effective elastic stiffness to assign to the LIB pouch cells. This resulted in the analytical load-displacement response matching that from the experimental tests. An effective stiffness of 35 ksi allowed a close correlation to the experimental data.

Table 6. Stainless steel material properties utilized in FEA analysis

Material	Density	E	ν	Fty	Ftu	Elongation at Break	Reference	Component
	$(\text{lb}_m/\text{in}^3)$	(psi)	(-)	(psi)	(psi)	(%)		
Stainless Steel (SS)	0.281	28,427,397	0.28	97,320	136,335	26.5	MatWeb	Foil Between Pouch Cells

The model was meshed with a nominal 0.035 in solid hexagonal elements. Surface-to-surface contact was defined between the surface of the bottom curved surface of the indenter and the top surface of the top pouch cell LIB.

Boundary conditions were assigned to the model to mimic the experimental test. The mechanical test base was simulated by simply supporting the bottom surface of the bottom cell, i.e., not allowing the configuration to translate in the Z-direction. Since one-quarter of the setup was modeled, appropriate symmetry boundary conditions were placed on the X-Z and Y-Z faces of the modeled components. The indenter was constrained so that only motion in the Z-direction was permitted. Rigid body motion was prevented by pinning the node at the center of the bottom pouch cell LIB's bottom surface.

The indenter was displaced a maximum of 0.05 in in the -Z-direction. An example of the displacement of the center of the quarter model appears in Figure 40, so that deflection through the thickness can be examined. The deflection in the model, mirrored about its planes of symmetry to show the entire configuration, is similar to that exhibited in the experimental test article as seen in Figure 41. The reaction force on the indenter in the Z-direction was plotted vs. the Z-displacement of the center of the top surface of the top pouch cell LIB and compared to experimental data on the exact configuration (but in three different electrical modes OCV, charge, and discharge) shown in Figure 42. The black dashed curve representing the analytical data lies close to the other (experimental) curves. For an example of how close the analytical curve matches the experimental curves, at 0.04 in deflection, the analytical load differs from the experimental loads by an average of 165 lbs. The slight difference between experimental and analytical curves can be attributed to the fact that the cell stack is treated as a solid box in the analytical modeling, and the effect of cell component compaction (Figure 30 c) during mechanical load is ignored.

It is important to mention that, as Figure 42 shows, the cell’s load-carrying behavior does not change significantly depending on whether the battery is under OCV, charge, or discharge modes. However, it’s a real possibility (section 8) that the electrical and thermal behavior may change under a given load with changes in electrical modes, whether the battery is under OCV or change or discharge during active load application.

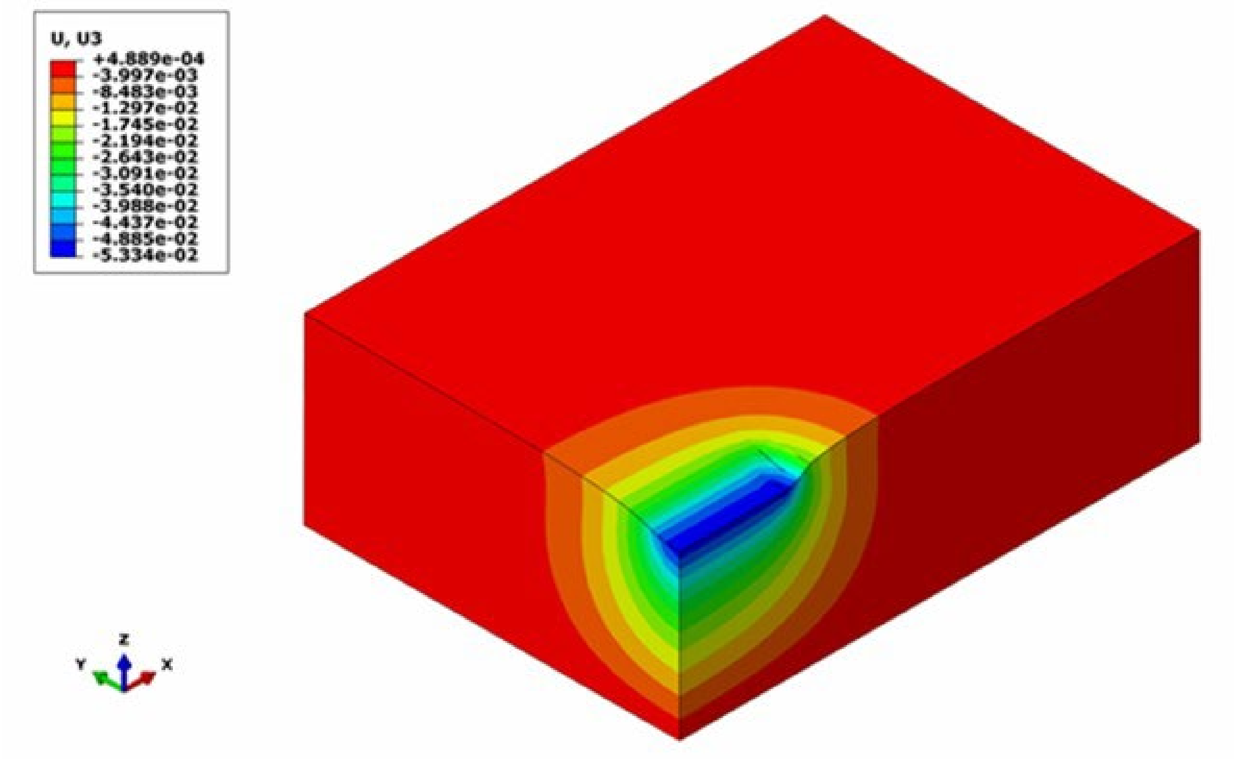

Figure 40. Displacement in Quarter Model of indentation test on pouch cell LIBs.

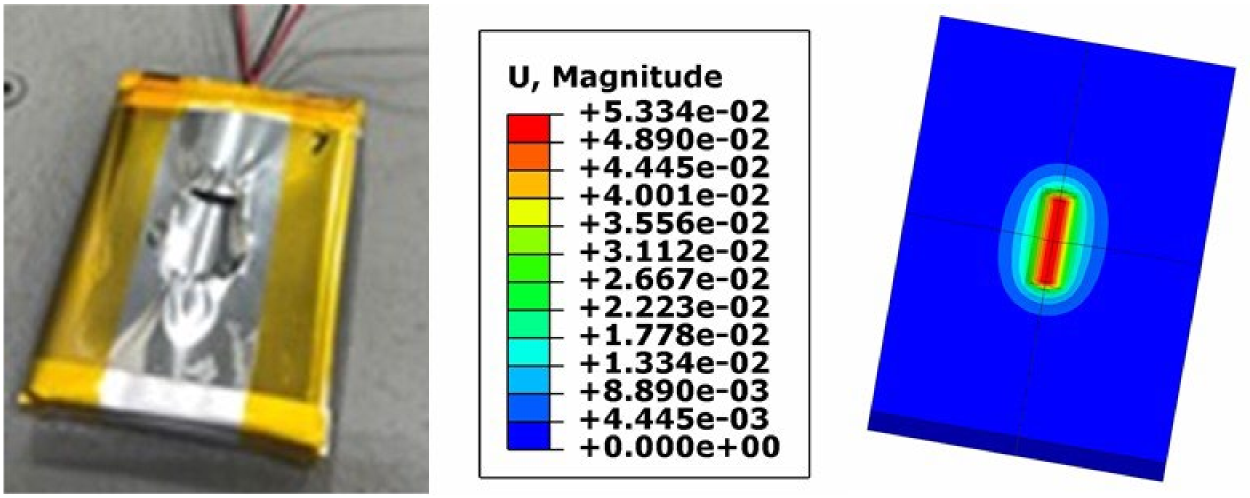

Figure 41. Deflection in indentation experimental pouch cell LIB test article (Left) compared to analytical model (Right).

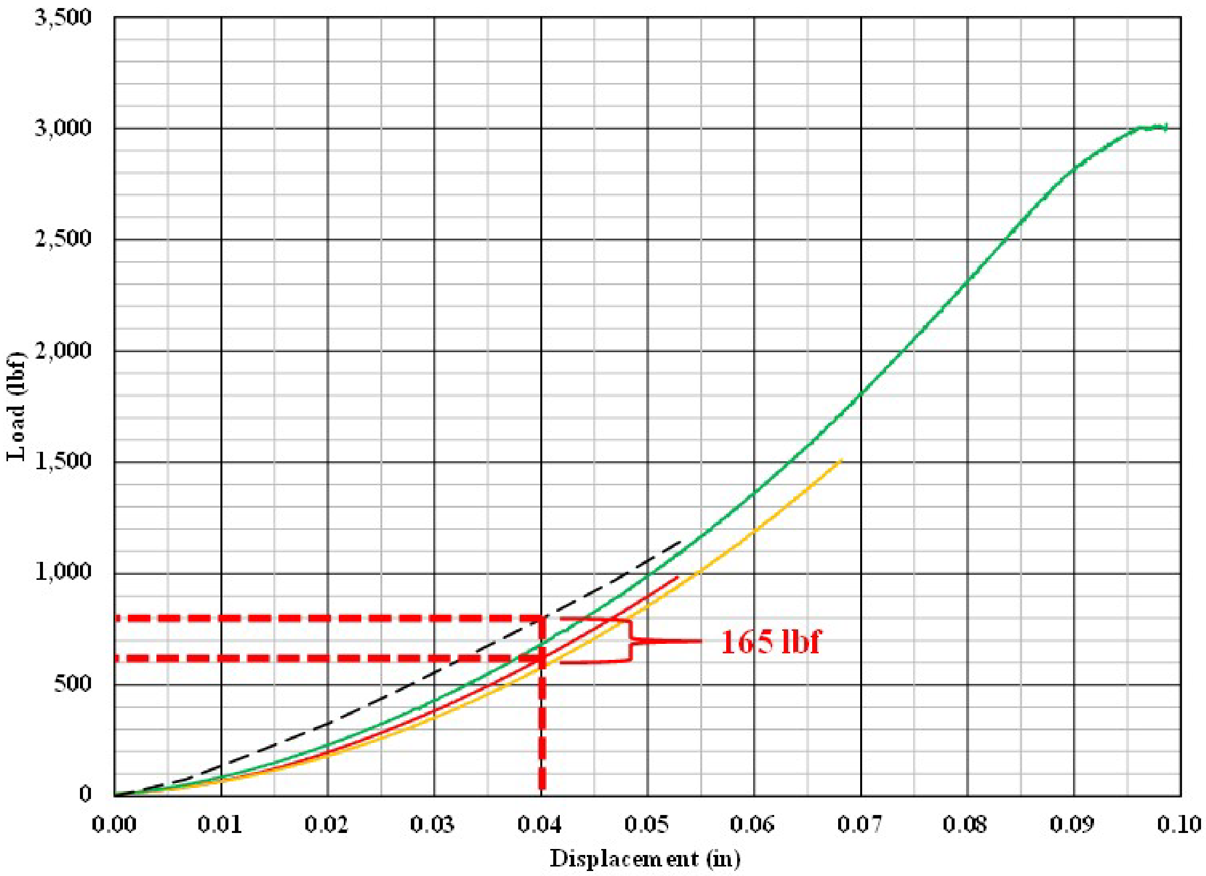

Key	Date	Configuration	Load Rate (in/min)	Charge/Discharge
🟥	11/1/2022	0.001 in SS between cells	0.01	OCV
🟨	11/2/2022	0.001 in SS between cells	0.01	Discharge
🟩	11/3/2022	0.001 in SS between cells	0.01	Charge
– – –	Analysis, E = 35 ksi			

Figure 42. Analytical data plotted along with experimental data for indentation test on stacked pouch LIBs cells without protection.

7.2 Indentation of two stacked pouch cells with a protective metal sheet

The configuration with a 2 mm (0.079 in) thick sheet of Ti added to the top of the stack for protection was also modeled as in Figure 43. A layer with the same length and width as the pouch cell LIBs was added to the previous model (Figure 39). Elastic-plastic Ti properties were assigned to the sheet on top of the two LIB pouch cells, as listed in Table 7. The Ti sheet was meshed with the same-size mesh, and surface-to-surface contact and boundary conditions were updated. The effective elastic stiffness assigned to the LIB pouch cells was determined through rigorous analysis iterations. This led to a close correlation between the analytical load-displacement response and the experimental tests—an effective stiffness of 70 ksi allowed for a near-perfect match to the experimental data.

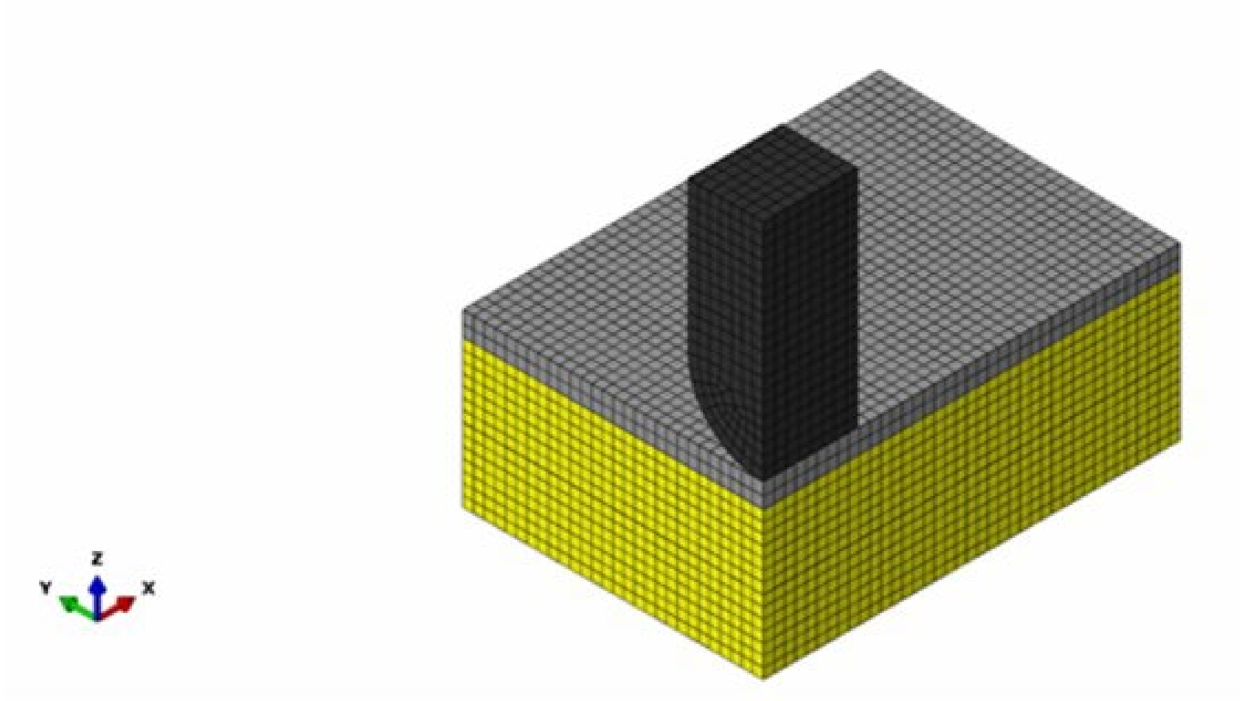

Figure 43. FEA model of indentation test on configuration with a top metal sheet.

Table 7. Titanium material properties utilized in FEA analysis

Material	Density	E	ν	Fty	Ftu	Elongation at Break	Reference	Component
	(lb_m/in^3)	(psi)	(-)	(psi)	(psi)	(%)		
Titanium (Ti)	0.163	16,824,378	0.34	20,305	31,908	54.0	MatWeb	Plate on Top of Pouch Cells

The indenter was displaced a maximum of 0.15 in in the -Z-direction. An example of the displacement of the center of the quarter model appears in Figure 44 so that deflection through the thickness can be examined. The reaction force on the indenter in the Z-direction was plotted vs. the Z-displacement of the center of the top surface of the top pouch cell LIB and compared to experimental data on the same configuration, as shown in Figure 45. Except for the early portion of the curve, during which differences are seen among all the batteries due to inner components' compaction under load, the black curve representing the analytical data lies nearly exactly on top of the red curve for one of the configurations experimentally tested.

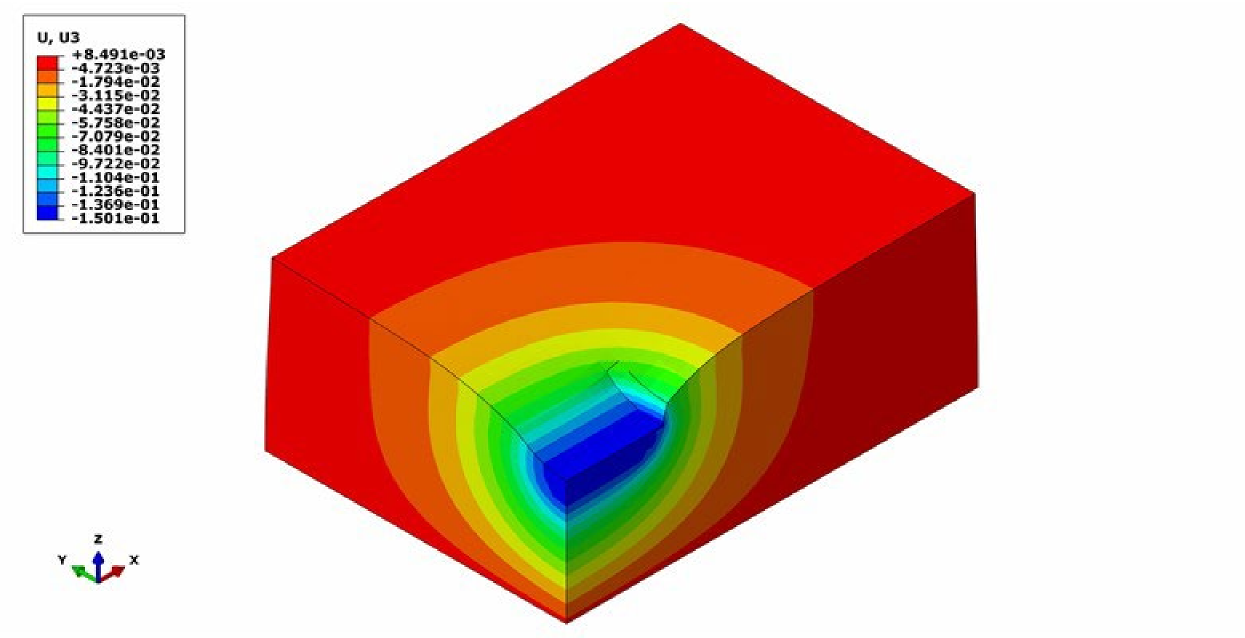

Figure 44. Displacement in a quarter model of indentation test on pouch cell LIBs with a metal sheet on top.

Although the loads required to produce similar deflections in the tests differed due to the minor differences in test articles noted in the experimental section, the slopes of the main portions of the experimental curves were nearly identical, and the analytical load-displacement response was matched to this slope.

The deflection in the model, mirrored by its planes of symmetry to show the entire configuration, is similar to that exhibited in the experimental test article, as seen in Figure 45. The reaction force on the indenter in the Z-direction was plotted vs. the Z-displacement of the center of the top surface of the top pouch cell LIB and compared to experimental data on the same configuration, as shown in Figure 46. Except for the early portion of the curve, when differences are seen among all the batteries due to inner components such as air or battery fluid being displaced, the black dashed curve representing the analytical data lies nearly precisely on top of the red curve. It possesses the same slope as that of the other experimental curves.

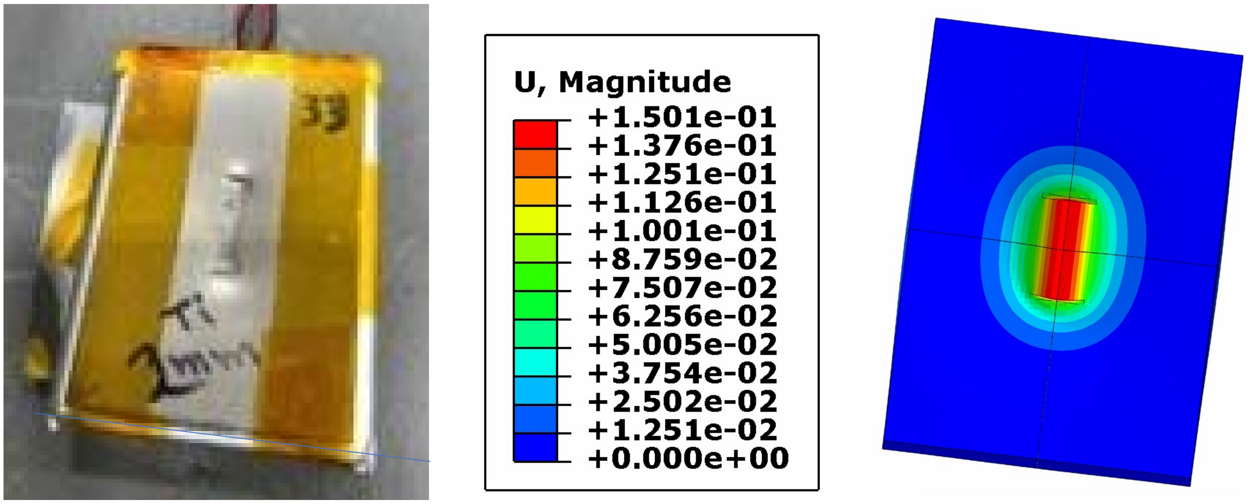

Figure 45. Deflection from indentation test in experimental pouch cell LIB test article with top sheet (Left) compared to analytical model (Right)

Analysis utilizing a model for the LIB stack configuration without a protective top metal sheet determined that the pouch cells have an effective elastic isotropic Young's modulus of 35 ksi (Figure 42), while analysis employing a model with a protective Ti top sheet determined that the effective modulus of the pouch cells is 70 ksi (Figure 46). Ideally, these moduli should have been the same. This difference suggests that more useful mechanical information could be gained from modeling the inner components of each LIB and assigning elastic-plastic material properties. Since this program focused on determining effective elastic isotropic properties of the LIBs, this could be an investigation for future efforts.

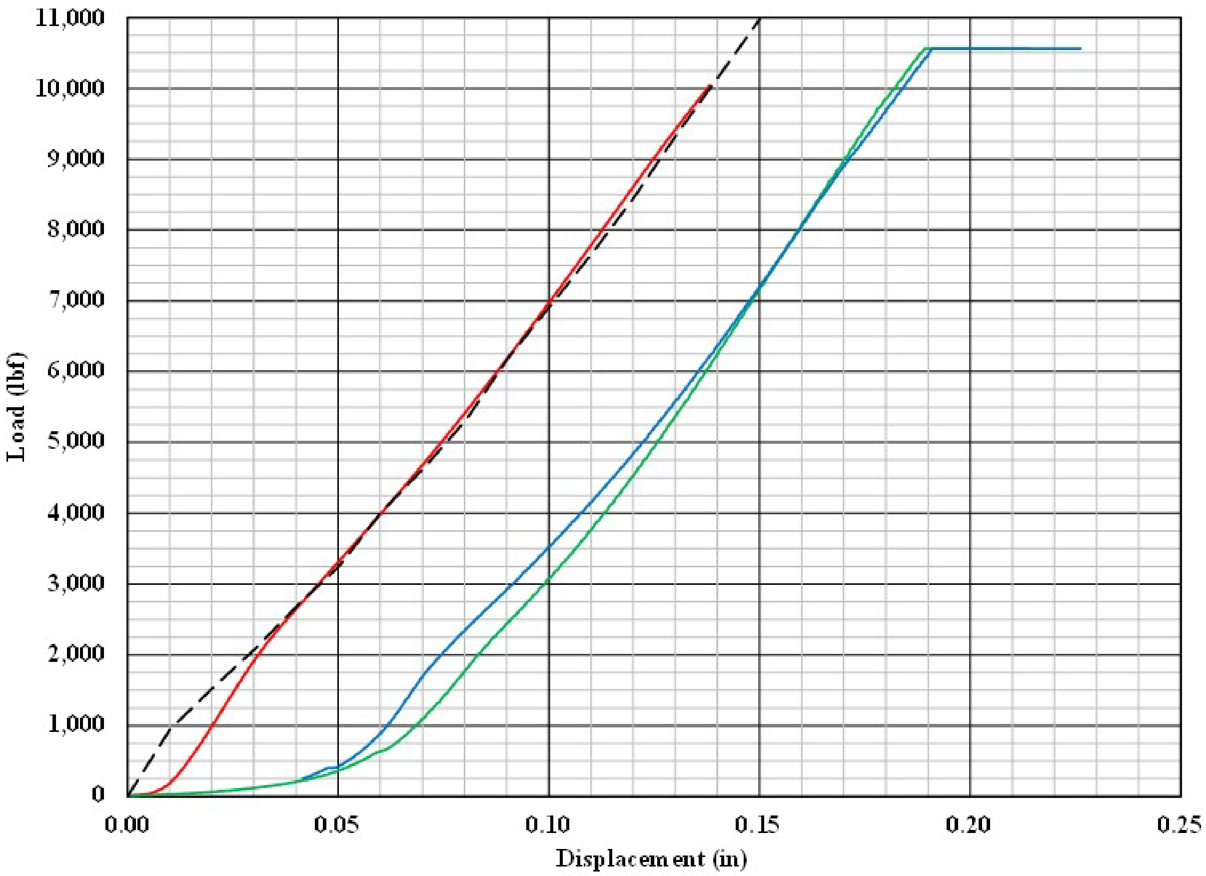

Key	Date	Configuration	Load Rate (in/min)	Charge/Discharge
🟥	12/1/2022	0.001 in SS between, 0.079 in Ti on top	0.98	Discharge
🟩	9/21/2023	0.001 in SS between, 0.079 in Ti on top	0.99	Discharge
🟦	9/21/2023	0.001 in SS between, 0.079 in Ti on top	1.98	Discharge
▬ ▬ ▬	Analysis, E = 70 ksi			

Figure 46. Analytical and experimental data for the indentation test on pouch cell LIBs with a Ti sheet on top are plotted.

7.3 Flat-plate compression of two stacked pouch cells without protective metal sheet

Figure 47 shows the experimental load-displacement behavior (blue curve) of 2 pouch cells stacked together compared to the analytical curve (black dashed). The response at the beginning of the test was nonlinear, possibly due to the compaction of cell inner components and/or battery fluid being displaced inside the pouch cell LIBs at the beginning of the test. The latter portion of the curve possesses a constant linear slope. The analytical load-displacement response was matched to this linear slope. An effective elastic isotropic Young’s modulus of 21.5 ksi allowed this close correlation. The black curve representing the analytical data possesses the same slope as the linear portion of the blue curve representing experimental data on the actual configuration tested.

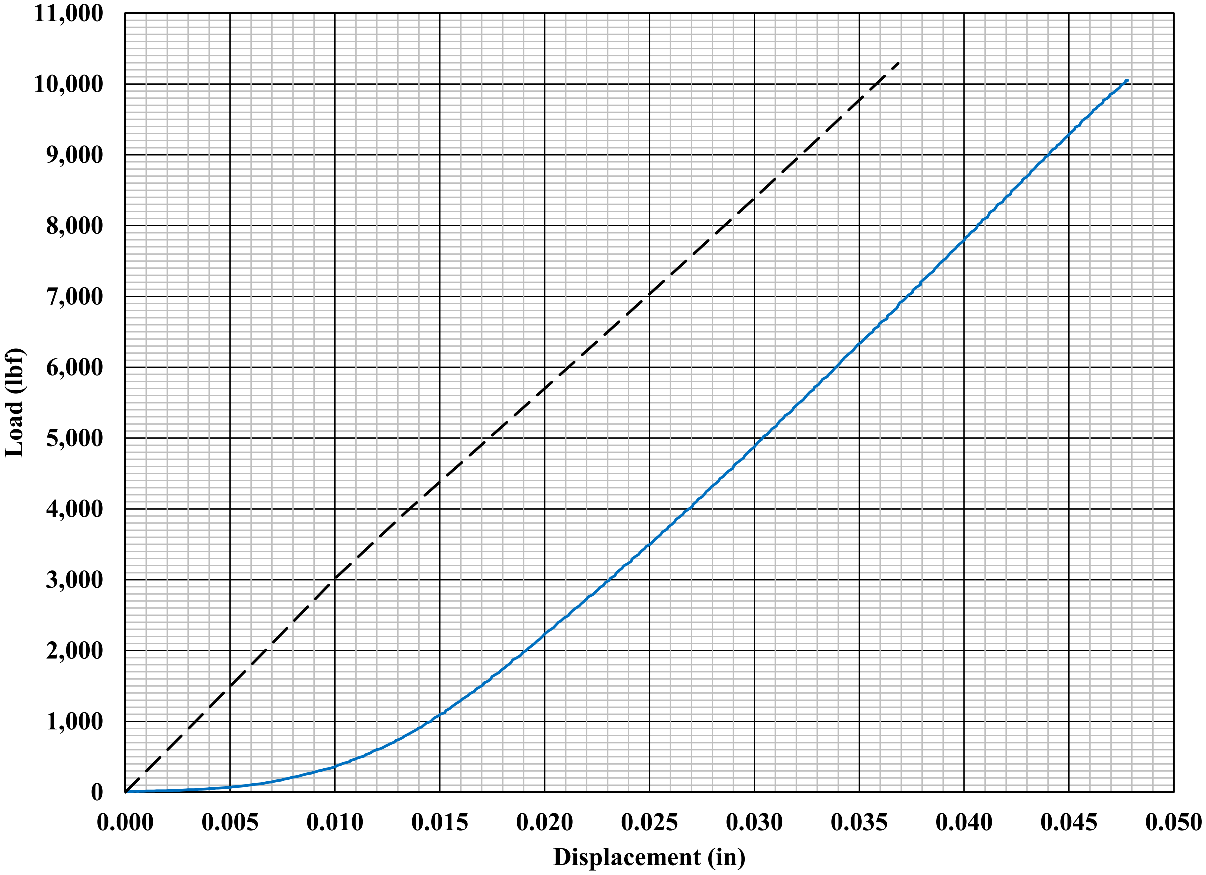

Key	Date	Configuration	Load Rate (in/min)	Charge/Discharge
━━━	12/1/2022	0.001 in SS between, no Ti on top	0.66	Discharge
━ ━ ━	Analysis, E = 21.5 ksi			

Figure 47. Analytical data plotted along with experimental data for flat plate compression test on pouch cell LIBs without top sheet

Analysis utilizing a model for the LIB stack configuration tested with an indenter determined that the pouch cells have an effective elastic isotropic Young’s modulus of 35 ksi (Figure 42), while analysis employing a model of the same stack configuration compressed between flat plates determined that the effective modulus of the pouch cells is 21.5 ksi (Figure 47). Ideally, these moduli should have been the same. The indentation test involves a localized deformation, while the flat sheet test involves a global compressive deformation. Shear stiffness dominates the response in the indentation test, while compressive stiffness dominates the flat plate compression test response. As noted previously, more useful mechanical information could be gained from modeling the inner components of each LIB and assigning elastic-plastic material properties.

7.4 Indentation of cylindrical cell without protective metal sheet

Figure 48 shows the experimental load-displacement behavior (red curve) of a single cylindrical 18650 Li-ion compared to the two analytical curves (black dashed and black dotted). The response during the test was nonlinear, possibly due to the compaction of anodes, cathodes, current collectors, and separators inside the battery cell and also the flattening of the cylinder cell casing. Analytical responses utilizing effective elastic isotropic Young's moduli of 20 ksi and 30 ksi appear to bracket the reaction of the experimental test, with the slope of the 20 ksi analytical response (*most probably due to flattening of the curved cylindrical surface of 18650 cell casing*) matching some portions of the experimental curve, and the 30 ksi analytical response (*due to compaction of cell internal components*) matching other portions of the experimental data (Figure 48).

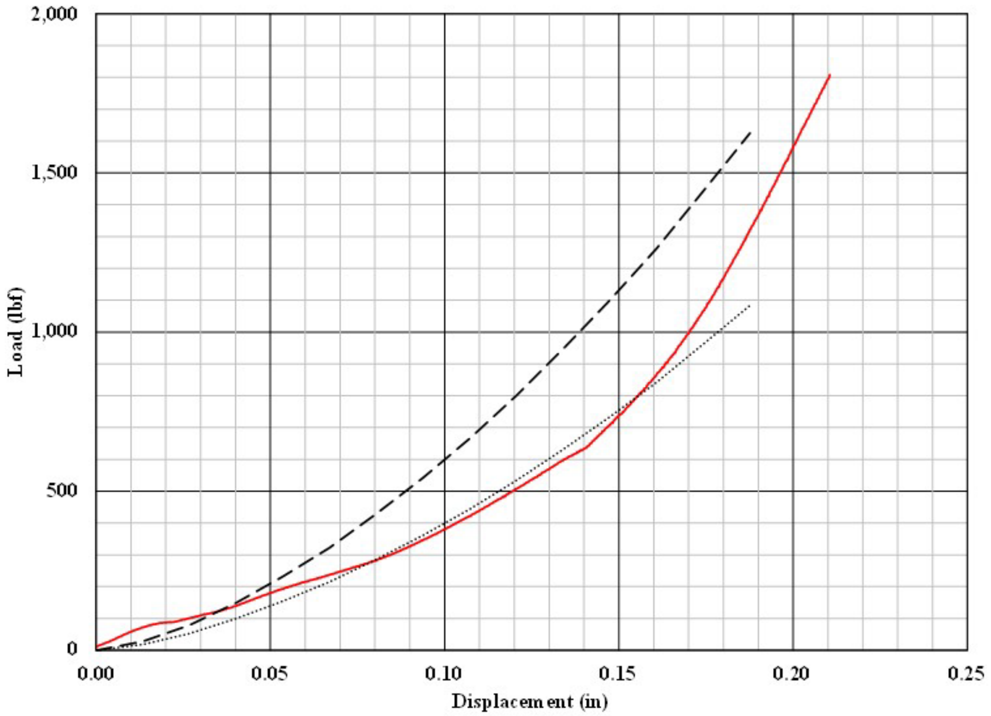

Key	Date	Configuration	Load Rate (in/min)	Charge/Discharge
▬▬	11/18/2022	3.4 Ah NCR18650	0.1	Discharge
▬ ▬ ▬	Analysis, E = 30 ksi			
▪▪▪▪▪▪	Analysis, E = 20 ksi			

Figure 48. Analytical data were plotted along with experimental data for the indentation test on a cylindrical NCR18650 cell.

7.5 Flat-plate compression of cylindrical cell without protective metal plate

Figure 49 shows the experimental and analytical response of a mechanically pressed cylindrical (NCR 18650) cell. The load-displacement response was linear at the beginning (regions I and II of Figure 49) of the test, possibly due to a combination of i) load taken by the stainless steel cell case, ii) the flattening of the cylindrical cell casing, and iii) load reactions in the inner components (compaction). Analytical responses utilizing effective elastic isotropic Young's moduli of 45 ksi and 85 ksi appear to match different portions of the experimental curve. The slope of the dotted black curve representing the analytical data with an effective isotropic Young's modulus of 45 ksi possesses the same slope as the initial portion of the red curve representing experimental data on the actual configuration tested. In comparison, the dashed black curve representing the analytical data with an effective modulus of 85 ksi matches the later portion of the red curve.

The numerical differences in load-displacement behavior of the same cylindrical 18650 NCR cells analyzed in Figure 48 (indentation) and Figure 49 (compression) can be attributed to the fact that in the indentation process, the load is concentrated in a small area (radius of indenter tip). In contrast, the load gets dispersed to a larger area along the surface of the cylindrical cell.

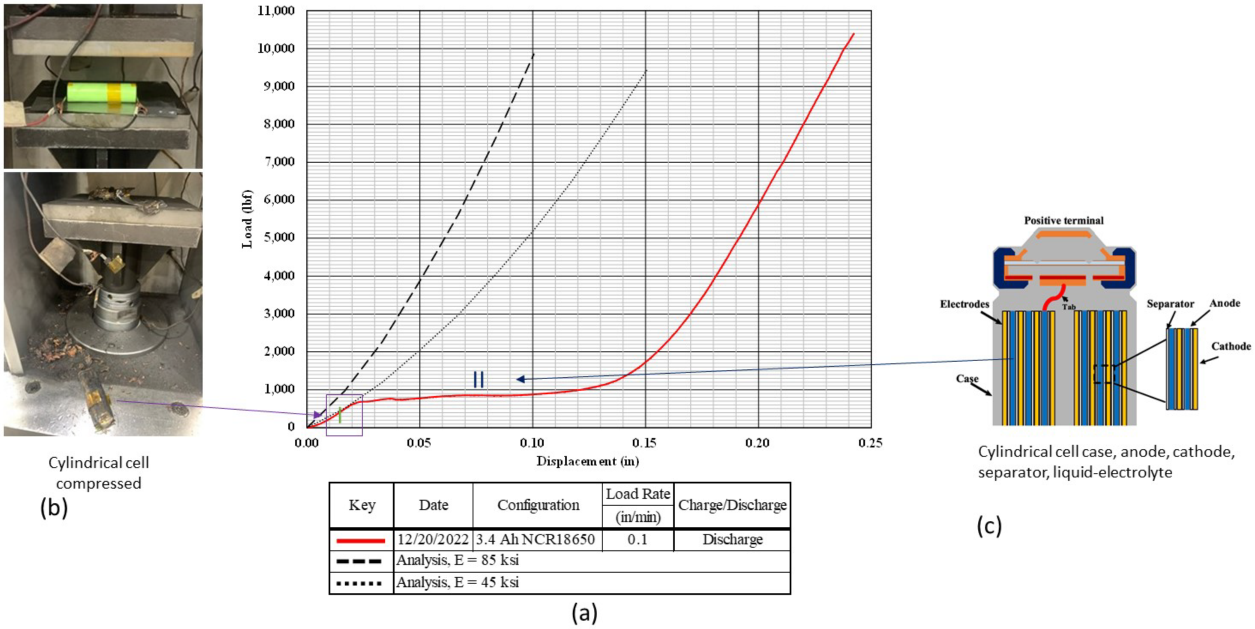

Cylindrical cell compressed

(b)

Key	Date	Configuration	Load Rate (in/min)	Charge/Discharge
▬▬	12/20/2022	3.4 Ah NCR18650	0.1	Discharge
▬ ▬ ▬	Analysis, E = 85 ksi			
••••••	Analysis, E = 45 ksi			

(a)

Cylindrical cell case, anode, cathode, separator, liquid-electrolyte

(c)

Figure 49. Analytical data compared with experimental data for a flat plate compression test on a cylindrical NCR cell, along with pictures of cell components and the flattening of the cylindrical cell case.

Analysis utilizing a model for the cylindrical NCR18650 battery tested with an indenter determined that the pouch cells have an effective elastic isotropic Young’s modulus of 20-30 ksi, while analysis employing a model of the same battery cell compressed between flat plates determined that the effective modulus of the pouch cells is 45-85 ksi. Ideally, these moduli should have been the same. The indentation test involves a localized deformation, while the flat plate test involves a global compressive deformation. Shear stiffness dominates the response in the indentation test, while compressive stiffness dominates the flat plate compression test response. As noted previously, more useful mechanical information could be gained from modeling the inner components of each LIB and assigning elastic-plastic material properties. An analysis that defines the material properties of the inner components and the interactions between them may be necessary, even more so than the analysis of indentation tests on cylindrical battery cells, to completely match the overall response of these cells to flat plate compression as exhibited in the experimental tests.

8 Mechanical-electrochemical-thermal analysis

As mentioned earlier, a critical deformation depth can cause a battery cell to reach its mechanical failure criteria where the principal strains in the components exceed their failure limit. A load exceeding the critical deformation can cause cell shorting (temporary or permanent), leading to voltage loss and a rise in cell temperature. It is essential to understand the magnitude of voltage loss and temperature rise. Still, it is critical to understand the time scale at which voltage loss and temperature rise happen after cell mechanical failure. A quick voltage drop and, hence, cell shorting lead to a fast temperature rise and less time for a battery management system to activate thermal management and contain the spontaneous thermal runaway (Schöberl, Ank, Schreiber, Wassiliadis, & Lienkamp, 2024). This section highlights the mechanical load-led damage of Li-ion cells and the time scale of voltage loss and temperature rise.

8.1 Temperature and voltage change during indentation of pouch cell

Figure 50 shows load, temperature, and voltage during indentation tests of pouch cells (2 pouch cells stacked together) under 0.5C rate discharge and without any metal sheet protection. The load was applied to the cell at a 1.0 in/min rate. The load reached a maximum within 10 seconds, a sharp voltage drop was observed at 50 seconds, and the temperature started rising after 120 seconds. The temperature rose from RT to 400°C within ~15 seconds. Nitrogen gas was flown to the cell when the cell failure (observation of sharp temperature rise) occurred; otherwise, the temperature may have gone beyond 1000℃ within 15-20 seconds. This spontaneous rise of temperature in mechanically damaged cells makes controlling thermal runaway nearly impossible, and the only way to avoid thermal runaway is to prevent reaching the critical load by employing battery protection sheets, as shown in Figure 51. Figure 51 shows the indentation of pouch cells at 2 in/min and the change in voltage and temperature. As can be seen from Figure 51, the voltage dropped around 35 seconds and recovered to normal. The temporary voltage drop was due to the cell components' local compaction (similar to Figure 32), which led to the forced discharge. As soon as the load was removed, cell components relaxed (decompressed), and the voltage recovered. The temporary voltage drop led to a slight temperature increase, never crossing 40°C. The recovered cells were stored for ten months and checked for capacity loss and cycling behavior, as discussed in Section 6.

Figure 52 shows load, temperature, and voltage during fatigue indentation tests of pouch cells (2 pouch cells stacked together) under 0.5C rate discharge and with and without metal sheet protection. As expected, even without protection (red curves), the cell fails after 100s of repeated indentation and takes around 100s seconds to fail. Total voltage loss and a modest temperature rise were observed. The cell was permanently damaged. On the other hand, with a 2 mm Ti protection (green and blue curves), the cell survived several hours to fail, and the temperature rise mainly was below 35°C. The battery management system can easily detect the slow rise in temperature and time-taking voltage loss, and such failures can be managed with a catastrophic battery fire.

Voltage and temperature changes were more dramatic in cylindrical cells despite the metal cell casing (though the thickness of the case (stainless steel) is only around 250 µm) compared to a soft plastic case used in the pouch cell. Figure 53 shows indentation load-led temperature and voltage changes in 18650 cylindrical cells made of two different cathode chemistries (NMC and LFP). NCR 18650 (red curves) and LFP 18650 (green curves) show similar maximum load before the failure. However, the NCR 18650 cell lost voltage almost instantly after reaching the maximum load, and a sharp temperature rise was observed within 150 seconds. Despite the N_2 flow, the cell caught fire (temperature could not be measured when the cell was on fire, perhaps due to thermocouple contact loss). On the other hand, the LFP NCR cell (green curves) lost voltage after 150 seconds of reaching maximum load, and the corresponding temperature rise peaked when the cell completely lost the voltage. The maximum temperature observed for NCR 19650 was only 100°C. A thicker LFP (26650) cylindrical cell could hold a much larger load (5,000 lb), lose voltage >700 seconds of reaching maximum load, and peak temperature was around 75°C. Notably, the time gap maximum load and voltage loss and temperature rise are significantly higher in the case of LFP-based cells compared to NCR cells. This allows BMS to sense load lead damage, prepare for battery cooling by activating the thermal management system, and avoid potential battery fire much more efficiently in LFP cell-based battery modules than NCR cells.

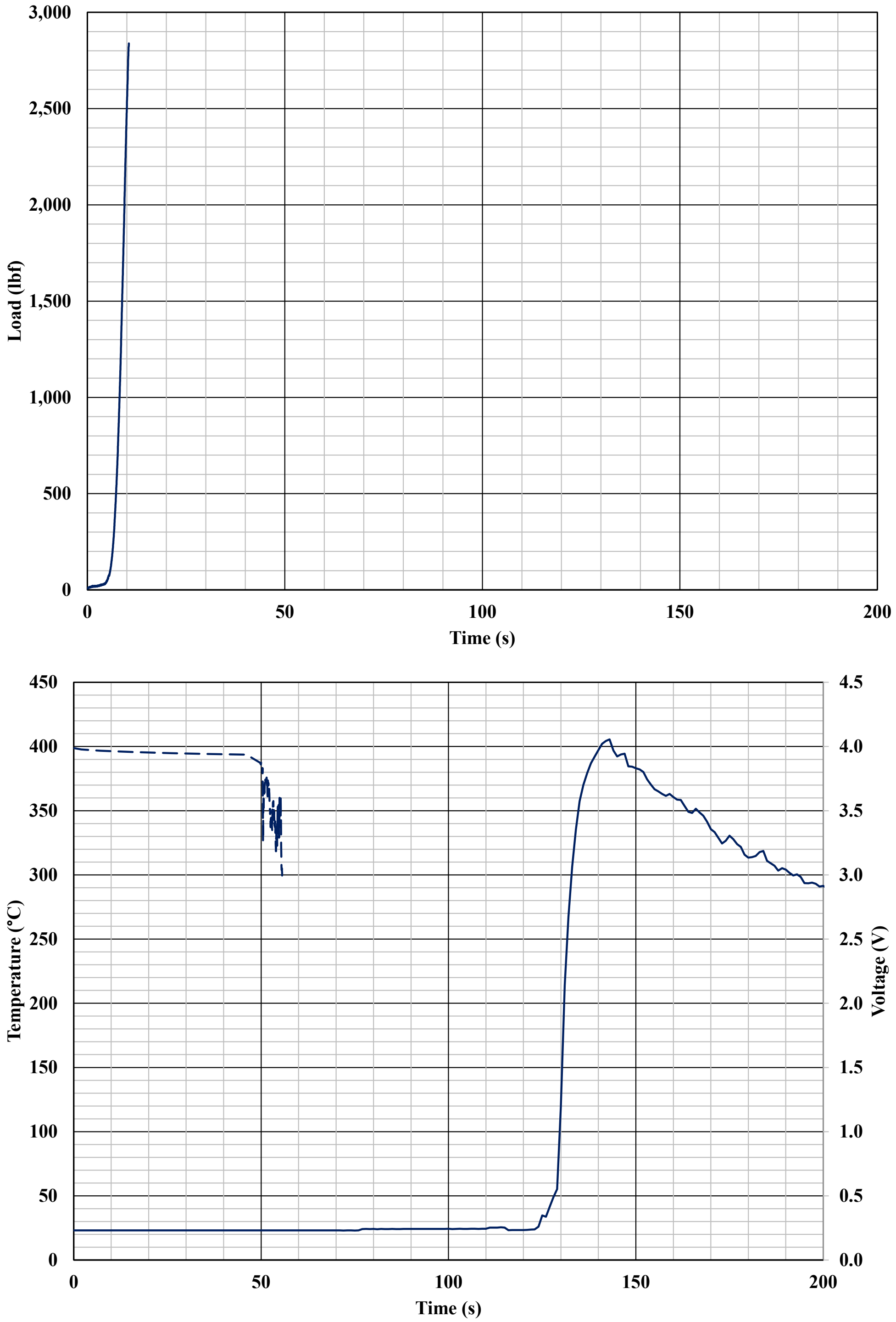

Key	Date	Configuration	Load Rate (in/min)	Charge/Discharge	Measurement
━━	9/21/2023	0.001 in SS between cells	1.00	Discharge	Load, Temperature
‒ ‒ ‒	9/21/2023	0.001 in SS between cells	1.00	Discharge	Voltage

Figure 50. Load, temperature, and voltage during pouch cell indentation (1.0 in/min).

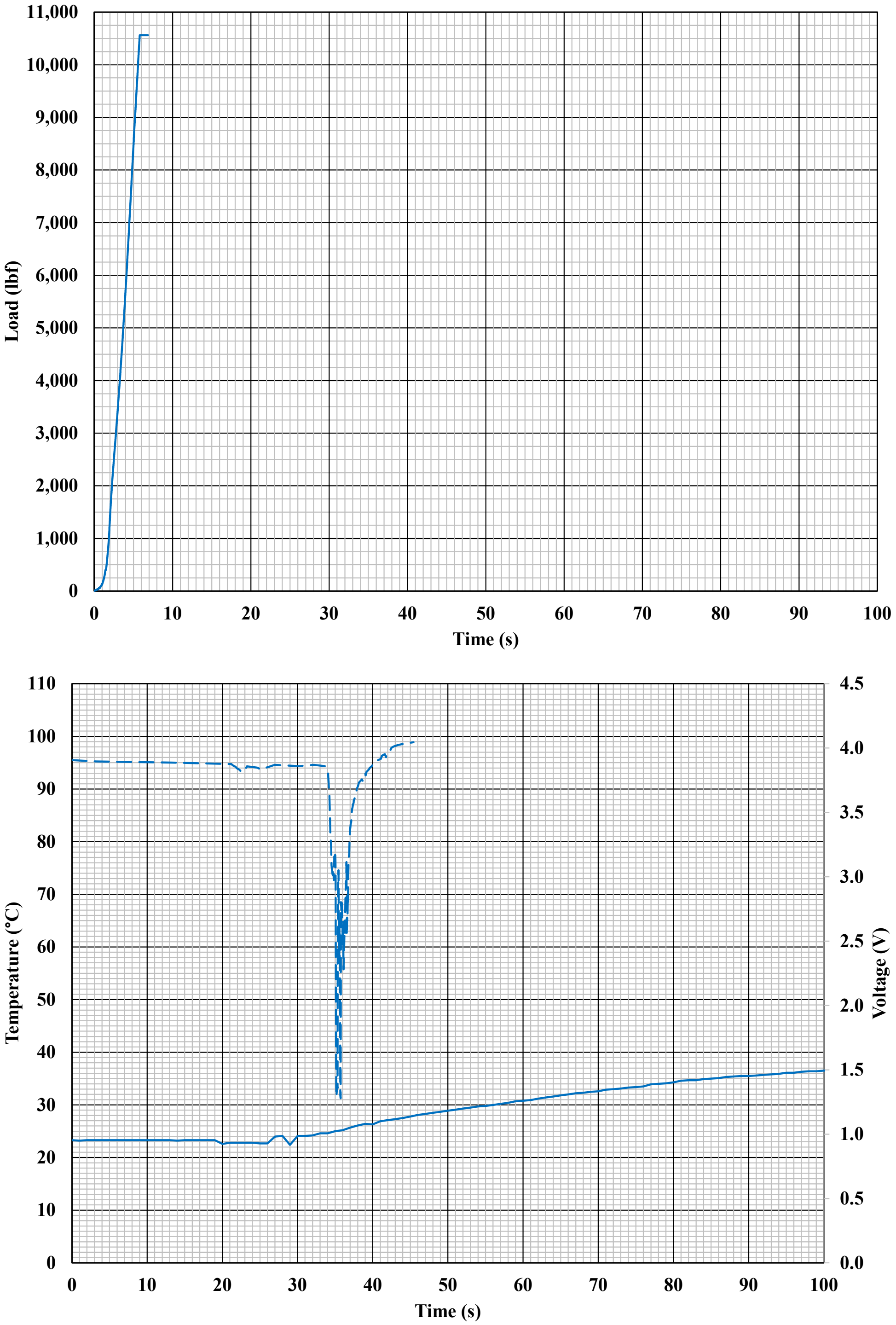

Key	Date	Configuration	Load Rate (in/min)	Charge/Discharge	Measurement
━━	9/21/2023	0.001 in SS between, 0.079 in Ti on top	1.98	Discharge	Load, Temperature
‐ ‐ ‐	9/21/2023	0.001 in SS between, 0.079 in Ti on top	1.98	Discharge	Voltage

Figure 51. The pouch cell's load, temperature, and voltage change are protected with a 2 mm titanium sheet when indentated at a 2.0 in/min rate.

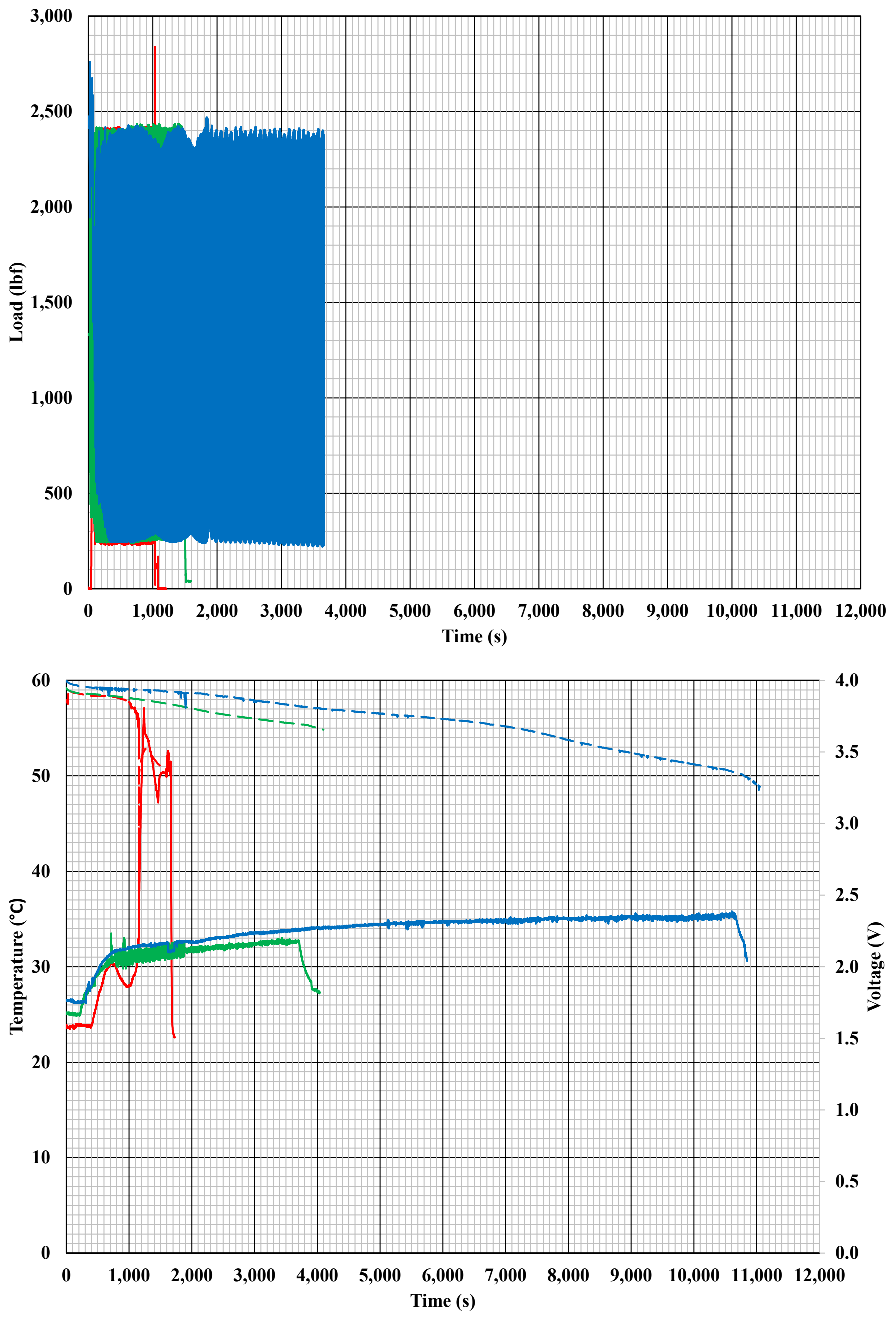

Key	Date	Configuration	Frequency (Hz)	Charge/Discharge	Measurement
🟥 ———	1/26/2023	25.4 µm SS between, no Ti on top	0.143	Discharge	Load, Temperature
🟥 - - -	1/26/2023	25.4 µm SS between, no Ti on top	0.143	Discharge	Voltage
🟩 ———	1/26/2023	25.4 µm SS between, 2 mm Ti on top	0.143	Discharge	Load, Temperature
🟩 - - -	1/26/2023	25.4 µm SS between, 2 mm Ti on top	0.143	Discharge	Voltage
🟦 ———	1/30/2023	25.4 µm SS between, no Ti on top	0.143	Discharge	Load, Temperature
🟦 - - -	1/30/2023	25.4 µm SS between, no Ti on top	0.143	Discharge	Voltage

Figure 52. Load, temperature, and voltage during fatigue tests on pouch cells with (2 mm Ti) and without protection were presented simultaneously.

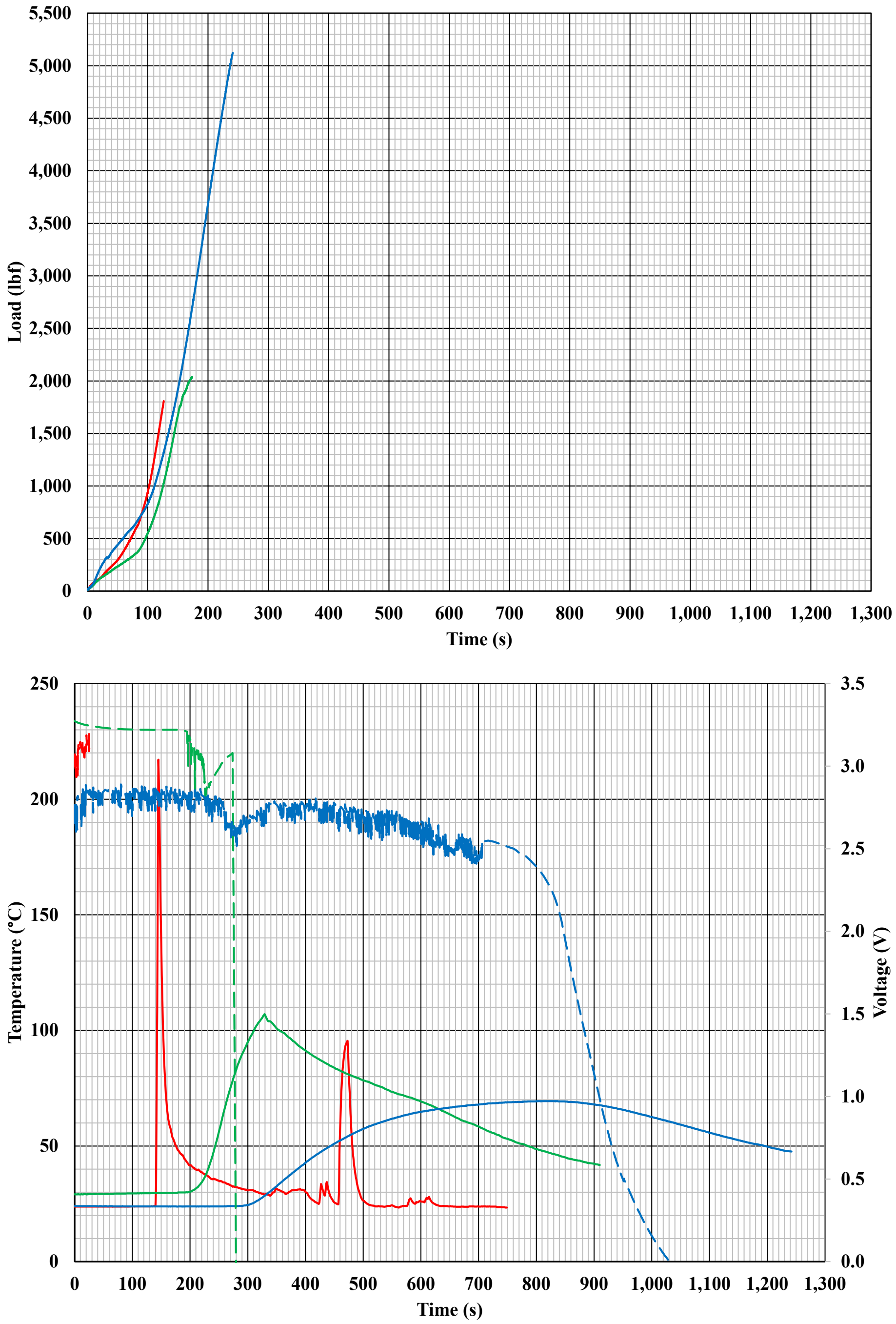

Key	Date	Configuration	Load Rate (in/min)	Charge/Discharge	Measurement
━━	11/18/2022	3.4 Ah NCR18650	0.1	Discharge	Load, Temperature
╍╍	11/18/2022	3.4 Ah NCR18650	0.1	Discharge	Voltage
━━	11/18/2022	1.7 Ah LFP18650	0.1	Discharge	Load, Temperature
╍╍	11/18/2022	1.7 Ah LFP18650	0.1	Discharge	Voltage
━━	11/21/2022	3.4 Ah LFP26650	0.1	Discharge	Load, Temperature
╍╍	11/21/2022	3.4 Ah LFP26650	0.1	Discharge	Voltage

Figure 53. Load, temperature, and voltage during indentation tests on cylindrical cells (18650) were presented on the same time scale.

8.2 Temperature and voltage change during compression of the pouch and cylindrical cells

Pouch cell: Due to its flat geometry, a protective plate may not be required to protect pouch cells from a flat-plate compression load unless the compression plate is uneven. Figure 54 shows the load, temperature, and voltage response of unprotected (blue curves) and with 0.4 mm Ti plates (red curves). Without the Ti plate, no temperature rise or voltage loss was observed for a very high compressive load (>10,000 lb). Meanwhile, with the Ti plate, there were uneven voltage drops during the compression test and, hence, uneven temperature rise (each voltage loss shows a corresponding temperature rise) up to a maximum of 90°C. Ideally, both the tests (with and without the Ti plate) should have yielded the same load, voltage loss, and temperature change, but the loss of voltage and increase in temperature with the Ti plate was because the edge of the Ti plate dented (Figure 55 – red arrows) the soft pouch cells. This can be avoided if the plate size is the same or bigger than the pouch cells.

Cylindrical cell: Unlike flat pouch cells, the cylindrical cell case can easily deform under compression load due to its curved geometry. Figure 56 shows unprotected cylindrical cells' load, temperature, and voltage response based on NCR (red curves) and LFP (blue curves) cathodes. Two voltage drops were observed for the NCR cell, the first one around the same time (150 seconds) as the load reached it's maximum, which may be flattening of the cell case and compressing cell components for forced discharge, and the second voltage loss (permanent voltage loss) which is which is around 250 seconds may be due to damage of cell components. NCR cells experienced a sharp temperature increase simultaneously with the second voltage loss. The cell went into thermal runaway. On the other hand, LFP cells carried almost x1.5 times higher load and maximum temperature approaching 100°C after 200 seconds of reaching maximum load. Once again, the LFP cathode seems less prone to thermal runaway, verified by many earlier studies, including ref. 2 cited for this report.

Pouch cell vs. cylindrical cell under compression: Comparing data from Figures 54 and 56, it's clear that for the same cathode chemistry (NMC) packaged in a pouch (Figure 54) and cylindrical (Figure 56) formats, pouch cells are much more robust than cylindrical cells under compression load.

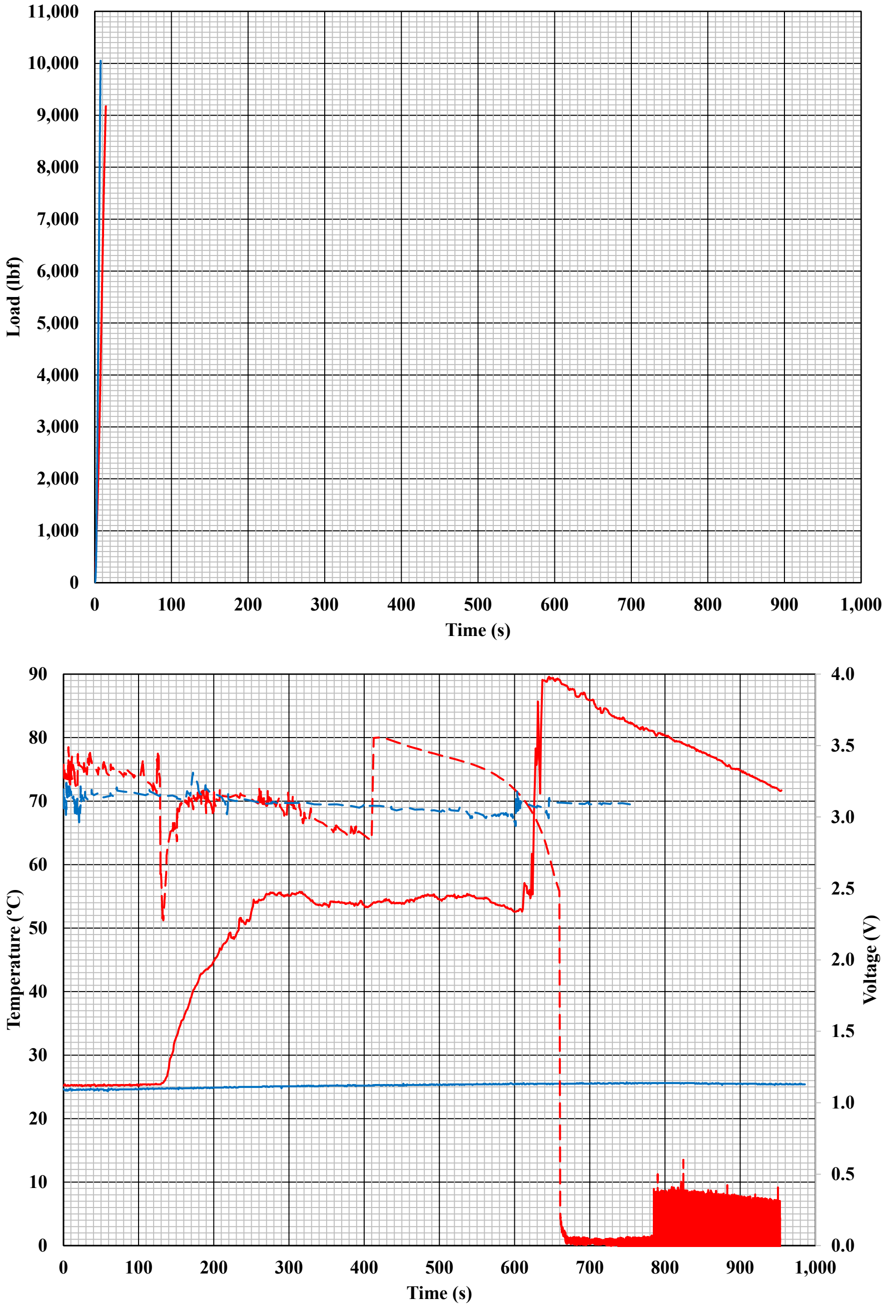

Key	Date	Configuration	Load Rate (in/min)	Charge/Discharge	Measurement
━━━	12/1/2022	25.4 µm SS between, 0.4 mm Ti on top	0.66	Discharge	Load, Temperature
╍╍╍	12/1/2022	25.4 µm SS between, 0.4 mm Ti on top	0.66	Discharge	Voltage
━━━	12/1/2022	25.4 µm SS between, no Ti on top	0.40	Discharge	Load, Temperature
╍╍╍	12/1/2022	25.4 µm SS between, no Ti on top	0.40	Discharge	Voltage

Figure 54. Load, temperature, and voltage during flat plate compression tests on pouch cells were presented on the same time scale.

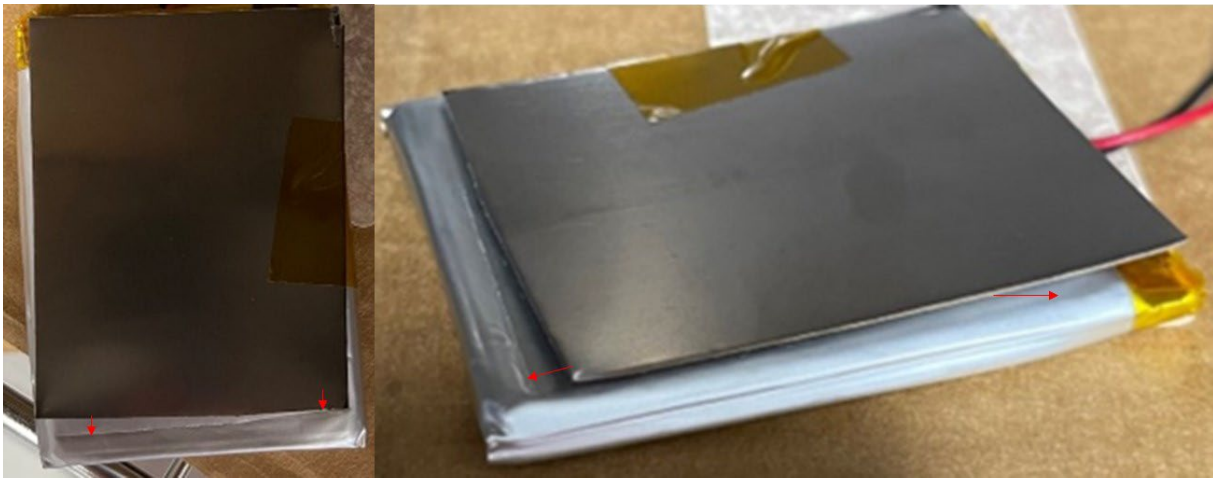

Figure 55: Cell damage due to the smaller size of the protective sheet.

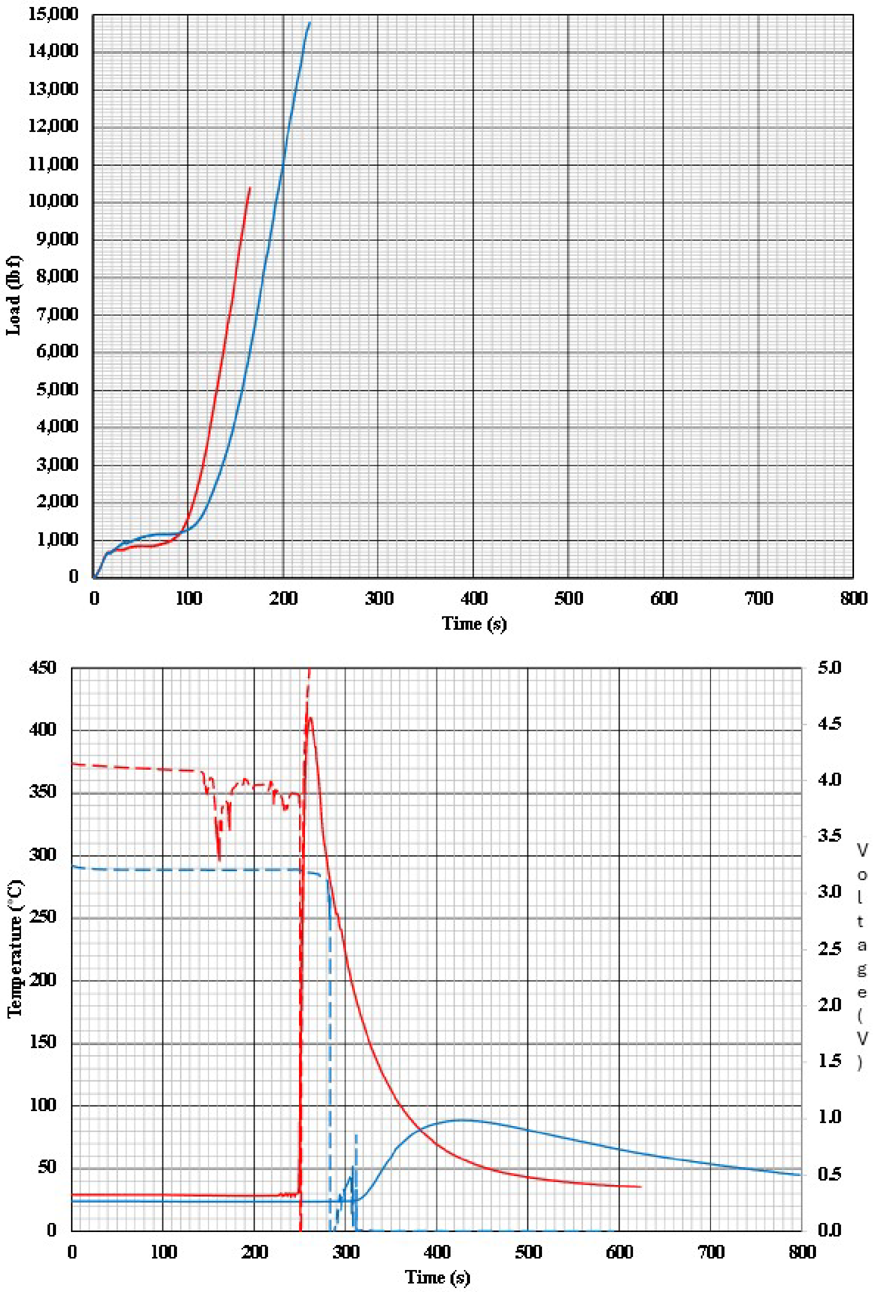

Key	Date	Configuration	Load Rate (in/min)	Charge/Discharge	Measurement
━━━	12/20/2022	3.4 Ah NCR18650	0.1	Discharge	Load, Temperature
- - -	12/20/2022	3.4 Ah NCR18650	0.1	Discharge	Voltage
━━━	12/21/2022	3.4 LFP26650	0.1	Discharge	Load, Temperature
- - -	12/21/2022	3.4 LFP26650	0.1	Discharge	Voltage

Figure 56. Load, temperature, and voltage were presented simultaneously during flat plate compression tests on cylindrical cells.

9 Conclusions

Under a project funded by the FAA, the battery research team at the University of Dayton Research Institute (UDRI) studied the feasibility of a model design of LIB battery pack that can be helpful to safely and efficiently provide power to the next-generation electric aircraft. The concept is based on designing a small LIB module mechanically protected by lightweight, thermally conducting, and corrosion resistance metal consisting of the following three main features:

1. An LIB based on an LFP cathode that can not only charge and discharge faster with longer cycle-life compared to an NMC cathode-based LIB but also presents a safer option, which is a vital requirement of an aircraft battery,
2. Between cylindrical and pouch cell configuration, the latter can be the preferred format as this provides an opportunity to densely pack cells in a module, which is enabled by wrapping metal foils for efficient and uniform cell thermal management naturally. The pouch cell format is also much more resistant to compression loads and has fewer failure chances if the cell experiences compression during either regular use or under collision,
3. Through a series of mechanical-thermal-electrical property studies supported by both experimental and analytical methods, it was found that Ti can be the most suitable metal as a secondary enclosure for encasing LIB modules safely and thermally,

As a next step,

1. Similar tests should be carried out at the module level to confirm the size of LIB modules needed for adequate performance and safety of EAVs.
2. If modular design, as suggested in this report, is effective, the FAA should facilitate research and development of needed power control systems that would be key to seamlessly controlling the functioning of all individual modules.

10 References

Aerotech News. (2020, June 12). Progress on cruise motors, future wing sets stage for all-electric X-57 ground tests. doi:https://www.aerotechnews.com/blog/2020/06/12/progress-on-cruise-motors-future-wing-sets-stage-for-all-electric-x-57-ground-tests/#:~:text=These%20components%20include%20the%20electric%20cruise%20motors,%20which%20will%20power

Cannarella, J., & Arnold, C. B. (2014). Stess evolution and capacity fade in constrained lithium-ion pouch cells. *Journal of Power Sources, 245*, 745-751. doi:https://doi.org/10.1016/j.jpowsour.2013.06.165

Cardone, M., Gargiulo, B., & Fornaro, E. (2021). Modelling and experimental validation of a hybrid electric propulsion system for light aircraft and unmanned aerial vehicles. *Energies, 14*, p. 3969.

Ding, Z., Wang, H., Luo, J., & Li, N. (2020). A review on forming technologies of fibre metal laminates. *International Journal of Lightweight Materials and Manufacture, 4*(1), 110-126. doi:https://doi.org/10.1016/j.ijlmm.2020.06.006

Dynamometer Schedules, Appendix I to Part 86, Title 40 (2023). Retrieved from https://www.ecfr.gov/current/title-40/part-86/appendix-Appendix I to Part 86

Kalnaus, S., Wang, H., Watkins, T. R., Simunovic, S., & Sengupta, A. (2019). Features of mechanical behavior of EV battery modules under high deformation rate. *Extreme Mechanics Letters, 32*. doi:https://doi.org/10.1016/j.eml.2019.100550

Keil, P., Schuster, S. F., Wilhelm, J., Travi, J., Hauser, A., Karl, R. C., & Jossena, A. (2016). Calendar aging of lithium ion batteries. *Journal of the Electrochemical Society, 163*(9), A1872-A1880. doi:10.1149/2.0411609jes

Kim, H. D., Perry, A. T., & Ansell, P. J. (2018). A review of distributed electric propulsion concepts for air vehicle technology. *2018 AIAA/IEEE Electric Aircraft Technologies Symposium (EATS)*, (pp. 1-21). Cincinnati. doi:https://ieeexplore.ieee.org/document/8552794

Morgan, A. B., Kumar, J., Barklay, C. D., & Kramer, D. P. (2020). Non-nuclear based thermoelectric + battery system concepts for space power systems. *IEEE Aerospace Conference*, (pp. 1-6). Big Sky. doi:10.1109/AERO47225.2020.9172493

Rickard Arvidsson, A. N. (2024). Life cycle assessment of a two-seater all-electric aircraft. *The International Journal of Life Cycle Assessment*, 240-254.

Schöberl, J., Ank, M., Schreiber, M., Wassiliadis, N., & Lienkamp, M. (2024). Thermal runaway propagation in automotive lithium-ion batteries with NMC-811 and LFP cathodes: Safety requirements and impact on system integration. *eTransportation, 19*, p. 100305.

Shaefer, J. (2016). *NOVA F7200 aircraft flight manual.* Altavian, Inc.

Skillings, J. (2013). *Boeing works to fireproof its 787 batteries (pictures)*. Retrieved from cnet.com: https://www.cnet.com/pictures/boeing-works-to-fireproof-its-787-batteries-pictures/

Skyquest. (2024). *Drone Market Size, Share, Growth Analysis - Industry Forecast 2025-2032.* Retrieved from https://www.skyquestt.com/report/drone-market/market-size

Stefan Baumeister, T. K. (2024). Emissions reduction potentials in business aviation with. *Transportation Research Part D*, 104415.

Tancogne-Dejean, T., & Mohr, D. (2022). Indentation of small format lithium-ion pouch cells: Experiments and modeling. *International Journal of Solids and Structures, 245*, 745-751. doi:https://doi.org/10.1016/j.ijsolstr.2022.111900

Zhang, A., & Li, Y. (2023). Thermal conductivity of aluminum alloys - A review. *Materials, 16*(8), 2972. doi:10.3390/ma16082972

A Experimental setup for mechanical indentation and compression tests

In this study, we focused on mechanical indentation (load through a semi-spherical indentor) and flat-plate compression (crush) tests to determine the mechanical strength of the battery enclosure. Figure A- 1 shows the mechanical test setup, including the mechanical test machine, fire extinguisher (nitrogen gas, spherical indentor (5 mm radius), and flat-plate compression setup. In semispherical indentation and flat-plate compression, many Li-ion battery cells will be subjected to piercing and crushing loads, respectively, mimicking a few possible collision scenarios. The battery's response regarding voltage change, temperature, and thermal runaway during the mechanical tests has been documented. Cells in different conditions (charged, discharged, and OCV) have been subjected to loads up to failure with variable speeds.

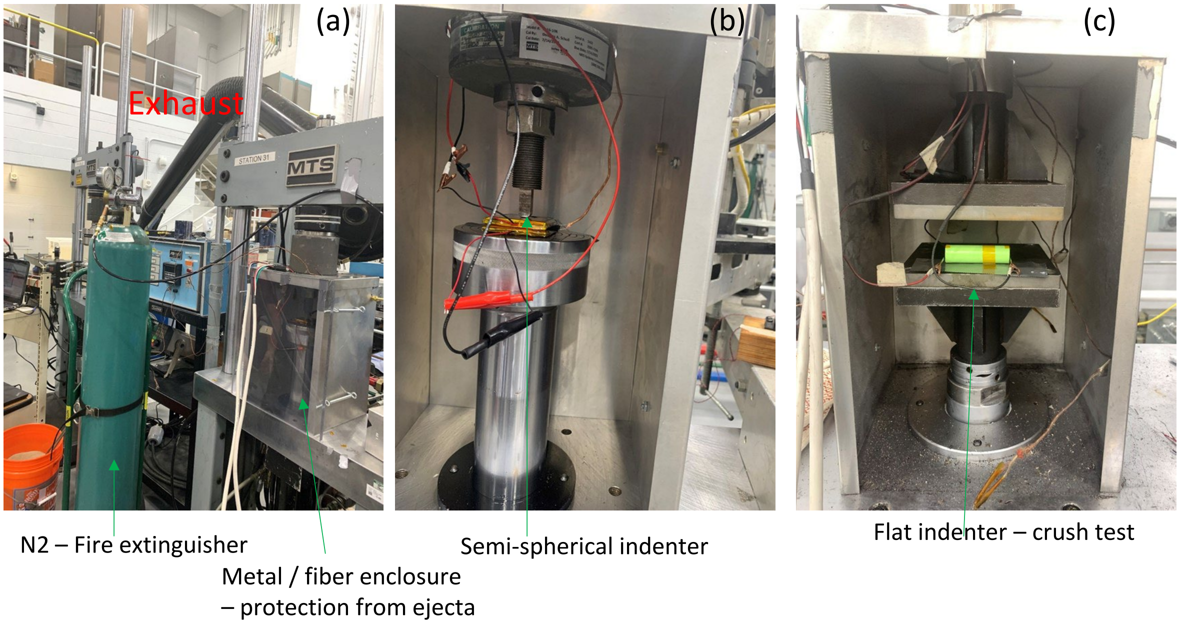

Figure A- 1. a. Mechanical test setup, including fiber wall protection from ejecta and nitrogen gas as fire extinguisher; b. battery placement below semi-spherical indenter, wires for battery cycling, and thermocouple for temperature measurement; c. setup for a crush test.